

DYNAMIC NUCLEAR POLARISATION OF DIAMOND

by

GRANT LYSLE HIGH

submitted in accordance with the requirements

for the degree of

DOCTOR OF PHILOSOPHY

in the subject

PHYSICS

at the

UNIVERSITY OF SOUTH AFRICA

PROMOTER: PROF. E C REYNHARDT

AUGUST 1998

Acknowledgements

First and foremost, I would like to thank my promoter, Prof. E C Reynhardt for his guidance and assistance during this study. In addition, I would like to thank him for making a significant contribution to my personal development beyond the requirements of this degree. It is much appreciated.

A great debt of gratitude is owed to Dr J A van Wyk for his assistance and willingness to share his vast knowledge and experience in the field of diamond impurities and electron paramagnetic resonance. Without his involvement, particularly in the development of the techniques for determining paramagnetic impurity concentrations, many of the new and interesting results would not have been possible to explain.

The influence and drive of my project manager, Dr U A S Tapper at DebTech, cannot be underestimated and a special note of thanks is directed to him. In addition, I would like to thank the rest of the project team at DebTech for their assistance and especially Bruce Dickson for his help with theoretical derivations of electromagnetic equations, Jens Eggers for proofreading and René Hoogenboosch and Cerina le Roux for their help with the figures and illustrations. I would also like to thank the management at DebTech for financial assistance during this study.

Next I would like to thank Dr D R Müller from Bruker Analytik for his positive and intuitive approach to many of the difficulties that arose during the investigation of the dynamic nuclear polarisation of diamond. I believe his influence and challenging manner contributed significantly to the scope and understanding attained during this study.

In addition to the people mentioned above, the following people have made significant contributions to my understanding and to the output in this study. I would therefore like to thank Mr F Meier and Dr P E Höfer of Bruker Analytik, Prof. M J R Hoch and Dr G

Hill of the University of the Witwatersrand and Mr C J Terblanche of the University of South Africa, for their input.

Finally, I would like to thank my wife, Martie and my daughter Grace, for their support, understanding and patience during the writing of this thesis and for being an inspiration and motivation.

Summary



This study is presented in nine chapters as follows:

Chapter one reviews the reported literature on the NMR of natural diamond. The NMR signal of diamond consists on a single line at 39 ppm from TMS and two hyperfine lines due to ^{13}C interactions. The reported relaxation times, measured in natural diamond, synthetic diamonds and ^{13}C enriched diamonds, are discussed.

The second chapter introduces the apparatus used, which included a Bruker Avance NMR spectrometer, a Bruker ESP380E pulsed EPR spectrometer and a high power s-band DNP system. The availability of this excellently equipped laboratory presented a unique opportunity to perform this investigation.

Chapter three outlines the experimental techniques used as well as the manner in which the acquired data was processed.

The fourth chapter presents an overview of the most common defects found in diamond. Proposed models of these defects are presented and the resulting EPR spectra displayed.

The methods developed to determine the paramagnetic impurity concentration from the EPR line width and the spin-spin relaxation times are presented in the fifth chapter. The line width gives the total paramagnetic impurity concentration to about 10 ppm. The spin-spin relaxation time allows the determination of P1 and P2 paramagnetic impurity concentrations individually, to much lower levels from measurements on the central and hyperfine lines. This information was used in the explanation of the relaxation behaviour for the various diamonds investigated.

The temperature dependence of the paramagnetic electron relaxation times is reported in the sixth chapter. The results obtained are consistent with the findings in prior work that P1 impurities are typical Jahn Teller centres. Two diamonds, however, display trends that depart from this theory. These diamonds contain N3 defect centres, which appear to be responsible for this behaviour. It was found in these experiments that, bar thermal expansion effects, the spin-spin relaxation time is essentially independent of temperature.

The seventh chapter deals with the solid state and thermal mixing effects. The relevant theory, results obtained and a discussion of these results, are presented. The effect of impurity concentration, defect types, microwave power, the exposure time and the offset from resonance on the polarisation rates and the ^{13}C polarisation are investigated in

depth. Finally the effect of applying the DNP treatment on the central and hyperfine lines is discussed.

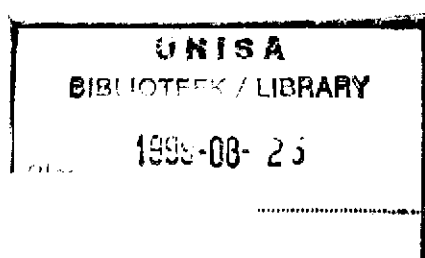
The pulsed DNP process is presented in the eighth chapter. The relevant theory, the effects of matching of the Hartmann-Hahn condition, impurity concentrations and types, on the polarisation rate and signal enhancement of ^{13}C nuclei is given. A comparison to the continuous wave techniques is then made.

The ninth chapter summarises the achievements and recommendations for further work.

Key terms:

Nuclear magnetic resonance; Electron paramagnetic resonance; Paramagnetic impurities; Dynamic nuclear polarisation; Diamond; Solid state effect; Thermal mixing effect; Nuclear orientation via electron spin locking.

553.82 HIGH



0001729193

List of Publications

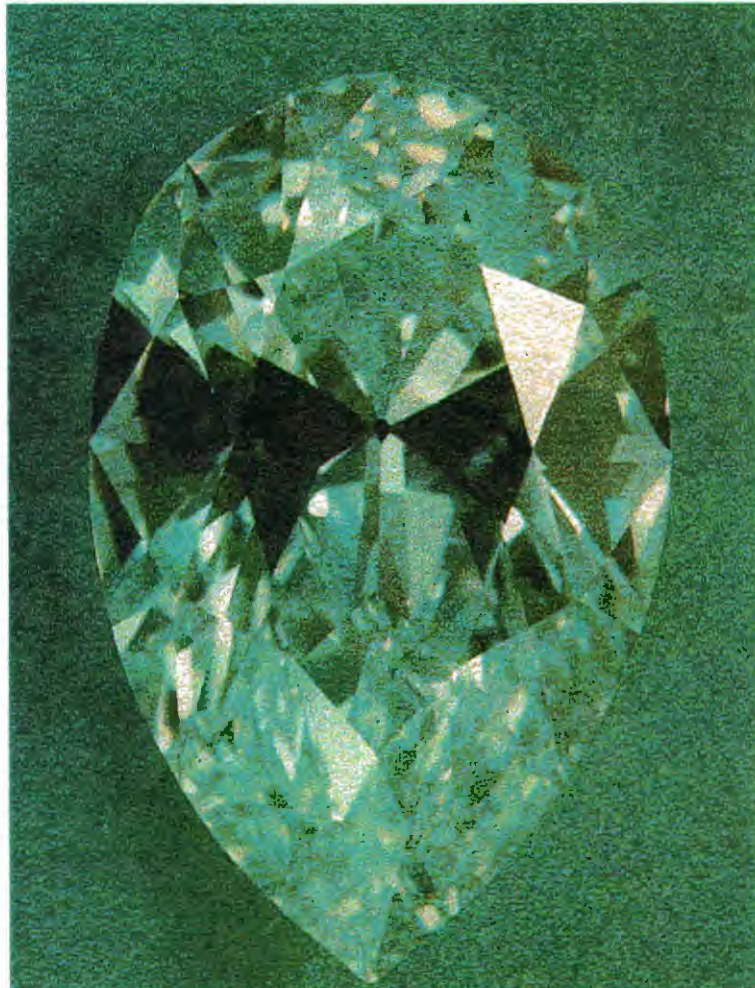
1. The Dependencies of ESR Line Widths and Spin-spin Relaxation Times, of Single Nitrogen Defects, on the Concentration of Nitrogen Defects in Diamond., J. A. van Wyk, E. C. Reynhardt, G. L. High and I. Kiflawi, J. Phys. D: Appl. Phys., **30**, 1790, (1997).
2. Dynamic Nuclear Polarisation of Diamond. I: Solid State and Thermal Mixing Effects., E. C. Reynhardt and G. L. High. Accepted for publication, J. Chem. Phys., (1998).
3. Dynamic Nuclear Polarisation of Diamond. II: Nuclear Orientation via Electron-spin Locking., E. C. Reynhardt and G. L. High. Accepted for publication, J. Chem. Phys., (1998).
4. Temperature Dependence of Spin-spin and Spin-lattice Relaxation Times of Paramagnetic Nitrogen Defects in Diamond., E. C. Reynhardt, G. L. High and J. A. van Wyk, Submitted for publication to J. Chem. Phys., (1998).
5. U. A. S. Tapper, D. R. Müller, G. L. High, G. W. Over and P. E. Höfer, Diamond Detection & Sorting, South African Patent No. 96/0325, application numbers are as follows: Australia 40876/96, Brazil PI96000872, Canada 2167119, Namibia 96/0003 and Russia 96/00761, 1995.
6. U. A. S. Tapper, D. R. Müller, G. L. High, G. W. Over and P. E. Höfer, Diamond Detection & Sorting (EPR techniques), South African Patent Application Number No. 95/0468, 1995.

7. U. A. S. Tapper, D. R. Müller, G. L. High, G. W. Over, J. A. van Wyk and P. E. Höfer, Diamond Detection & Sorting (pulsed EPR techniques), South African Patent Application Number No. 95/0468, 1995.

8. E. C. Reynhardt and G. L. High, *Dynamic Nuclear Polarisation of ^{13}C Nuclei in Natural Diamond*, 29th Ampère – 13th ISMAR Conference, Berlin, (1998).

Preface

Diamond – Magic and Mystique



Diamond, the material studied in this investigation has a long and interesting history, a flavour of which is given here, for the interested reader. Ancient kings and monarchs celebrated the sparkle of diamond in myth and legend for centuries as symbols of love and enduring relationships. The mystique of diamonds lies not only in their inherent beauty, but also in the talismanic properties attributed to them. Because of their clarity and brilliance, diamonds have been regarded as both a test and a guarantee of chastity,

while their durability has made them an assurance of permanence – of eternal love or as the advertisement leads one to believe, “a diamond is forever”.

One of the earliest legends associated with diamond is that of the valley of diamonds [P.1]. The elements that constitute the legend were first mentioned by Epiphanius (ca 315-403 AD), bishop of Salamis, metropolitan of Cyprus and an ardent follower of the faith of Nicaea. As Epiphanius tells it:

In the Scythian desert there is a deep valley surrounded by high and rocky mountains. From the summit one cannot see the bottom of the valley, which is lost in a fog as though in impenetrable depths. The kings of the surrounding countries sent their people to this valley to extract the treasures of precious stones that lay heaped in the farthest depths. To accomplish this task the people had to resort to trickery. They killed and flayed sheep and cast their quarters in to the depths of the valley where incalculable treasures lay. Soon eagles appeared from their aeries and swooped down through the fog to seize upon the flesh and carry it back to their nests. The precious stones adhere to the flesh and the king's people have only to rob the eagles' nests to gather them.

The reoccurrence of this legend is quite remarkable, it reappears (circa 500 AD) in the memoirs of the Chinese princes of the Liang dynasty as well as in the oldest known treatise on mineralogy (circa 750). This treatise is accredited to a writer known as the “pseudo Aristotle” and mentions Alexander the Great's acquisition of diamonds from a valley using birds and bait. With time the legend gathers additional elements, such as the presence of serpents that protect their precious cache with a murderous gaze as well as the statement that the precious cache is exclusively diamond. Marco Polo also gave an account of the legend and placed its origin in India. It is however now believed to have had its origin in the Hellenistic East in the first century BC – at a time when the diamond trade was just beginning. The legend is thought to have reached China and was transmitted to the Arabs and Persians before spreading to India and finally to Europe.

Another legend that may be of particular interest to the reader of this thesis is that of diamond's power over magnets [P.2]. Not all legends lend themselves to rational explanation and this particular myth, that diamond is an effective magnetic field filter, is a case in point. It is difficult to understand what lay behind the belief, repeated by Pliny the Elder, that a diamond would remove the attractive power of a magnet. It attributes a very unusual quality to diamonds and it would be tempting to dismiss it as purely the moral of some fable. It is however interesting that this belief has sustained been over the centuries and is repeated by authors that must be taken seriously. One of the most unlikely places for this legend to surface is in "*Gargantua and Pantagruel*" by Francois Rabelias (1494 – 1553) who, besides being a writer of fiction, was also a well known physician and scientist and editor of several medical works. The gist of the legend is as follows:

After reaching the farthest point on their voyage to the Land of the Lanterns, Pantagruel and his companions came to the kingdom of "Dive Bouteille" and were invited to enter the temple of Bacchus. The doors of the temple are opened and closed by an invisible force, controlled by a complicated device consisting of plates of polished steel, magnets and an "Indic diamond as thick as an Egyptian bean". Rabelias explained that the system functions according to a natural law, "occult and splendid", based on the attraction of iron to magnets. He adds that it only operates when the diamond is removed, for the diamond frees the steel from its natural obedience to the magnet, and the stone must be removed if the magnet is to operate efficiently. For a more thorough understanding of this legend the reader is referred to the study by K H Francis [P.3].

The essences of some other interesting legends are, for example, the legend of the curative power of diamond. Here Li Shi-chen asserts that when diamond is set into hair spangles, finger rings or girdle-ornaments, it wards off uncanny influences, evil and poisonous vapours. Pliny the Elder contends that diamond neutralises poisons, dispels insanity and drives away groundless apprehensions from the mind. In another, *Agastimata* curses would-be forgers and recommends the following recipe: "The vile

man who fabricates false diamond will sink into an awful hell, charged with a sin equal to murder. When the connoisseur believes that he recognises an artificial diamond, he should test it by means of acid or through the application of heat. If false, it will lose its colour and if true will double its lustre. It may also be washed and brought into contact with rice: it will at once be reduced to a powder”.

It is legends such as these that have contributed to the mystique surrounding diamond and could have prompted Wilke Collins to say: “The diamond laid such a hold on me I burst out with a large ‘O!’ The only one of us who kept his sense was Mr. Godfrey. He said ‘Carbon, mere carbon my good friend, after all’ ” [P.4].

Today diamonds are not only accessible to kings and monarchs. The book “Diamond People” [P.5] published in 1990, states that world-wide, some three hundred million women own at least one piece of diamond jewellery and each year, husband, lovers and woman themselves, spent about forty billion US dollars on sixty million pieces of jewellery containing fifteen million carats of diamond. Behind these numbers is an industry that mines diamonds in more than twenty countries, employing over 200 000 people on formal mines and countless others on independent diggings (both legal and illicit). The cutting of diamond takes place in over 30 countries and employs around 800 000 people. The jewellery manufacturing industry employs this many people again. All tolled, approximately two million families are dependent on the diamond industry for their livelihood.

The subject of this thesis is perhaps a more sober investigation into some magnetic resonance properties of natural diamond with, hopefully, more rational explanations of the results than given above.

References

- [P.1] *Diamonds – Myth, Magic and Reality*. (Crown Publishers. Inc. New York. Original text and illustrations © by Smeets Offset, Weert The Netherlands, 1980)
- [P.2] *Publications of the Field Museum of Natural History*. (Anthropological Series, XV, Kruas Reprint Corp., New York, 1967).
- [P.3] K H Francis, *The mechanism of the Magnetic Doors of Rabelias*, (French Studies 13, Oxford, 1959).
- [P.4] Wilke Collins, *The Moonstone*, London: Tinsley, (1868).
- [P.5] *Diamond People*. (Norfolk House, 1990).

Table of Contents

Acknowledgements.....	3
Summary.....	5
List of Publications.....	9
Preface.....	11
Diamond – Magic and Mystique.....	11
References.....	15
Table of Contents.....	17
Chapter 1.....	23
Magnetic Resonance Studies in Diamond.....	23
A Literature Survey.....	23
1.1 Basic Nuclear Magnetic Resonance of Diamond.....	24
1.2 Magnetic Resonance in Semiconducting Diamonds.....	28
1.3 Electron Paramagnetic Resonance in Diamond.....	29
1.4 References.....	30
Chapter 2.....	31
Apparatus.....	31
2.1 Introduction.....	32
2.2 S-Band Dynamic Nuclear Polarisation System.....	33
2.3 X-Band Dynamic Nuclear Polarisation System and Electron Paramagnetic Resonance Spectrometer.....	36
2.4 Nuclear Magnetic Resonance Spectrometer.....	38
2.5 Low Temperature Equipment.....	39
2.6. References.....	40
Chapter 3.....	41

Experimental Techniques.....	41
3.1 The Nutation Experiment	43
3.2 Spin-Spin Relaxation Time Measurements	47
3.2.1 Pulse Sequences.....	47
3.2.2 Pulse Lengths and Delay Times	48
3.2.3 Low Temperature Spin-Spin Relaxation Time Measurements	50
3.3 Spin-Lattice Relaxation Measurements.....	50
3.3.1 Pulse Sequences.....	50
3.3.2 Pulse Lengths and Delay Times	52
3.3.3 Low Temperature Spin-Lattice Relaxation Time Measurements.....	54
3.4 Rotating Frame Spin-lattice Relaxation Time Measurements.....	54
3.4.1 Pulse Sequences.....	54
3.4.2 Pulse Lengths and Delay Times	56
3.5 Continuous Wave Dynamic Nuclear Polarisation at X-Band	58
3.6 Continuous Wave Dynamic Nuclear Polarisation at S-Band	60
3.7 NOVEL at X-Band	62
3.8 NOVEL at S-Band.....	66
3.9 Nuclear Polarisation Enhancement.....	67
3.10 The Dipolar Reservoir	68
3.11 Nuclear Magnetic Resonance Measurements.....	69
3.11.1 Nuclear Magnetic Resonance Pulse Sequences.....	70
3.11.2 Nuclear Magnetic Resonance Signal Processing	70
3.11.3 Probe Head Tuning.....	70
3.12 EPR Measurements	71
3.12.1 EPR Line Width Measurements	71
3.12.2 Electron Paramagnetic Resonance Spectra.....	71
3.12.3 Electron Relaxation Times	73

3.13 References	75
Chapter 4.....	77
Common Defects in Diamond	77
4.1 Introduction to Defects in Diamond.....	79
4.2 Description of P1, P2 and N3 centres.....	80
4.2.1 Dispersed Substitutional Nitrogen: The P1 Centre	80
4.2.2 Aggregated Nitrogen. The P2 Centre	83
4.2.3 The N3 Centre	84
4.3 Diamond Types	87
4.3.1 Type I.....	87
4.3.2 Type II	88
4.4 Sample Characterisation.....	88
4.5 References	89
Chapter 5.....	91
Determination of the Paramagnetic Impurity Concentration in Diamond from the EPR Line Width and the Spin-spin Relaxation Time.	91
5.1 Introduction	93
5.2 Background theory	93
5.2.1 Impurity Concentration Determined from the EPR Line Width.	93
5.2.2 Impurity Concentration Determined from the Spin-Spin Relaxation Time.	96
5.3 Results	97
5.3.1 Synthetic Diamond Samples.....	97
5.3.2 Natural Diamond Samples.....	97
5.3.3 Impurity Concentration as a Function of Line Width	97
5.3.4 Impurity Concentration as a Function of Spin-Spin Relaxation Time	99
5.4 Discussion.....	101
5.5 References	102

Chapter 6.....	103
Temperature Dependence of the Spin-Lattice and Spin-Spin Relaxation Times in Natural Diamond.....	103
6.1 Theory.....	105
6.1.1 The Ideal Crystal Case.....	105
6.1.2 The Van Vleck Theory of Relaxation via Spin-orbit Coupling.	116
6.1.3 The Orbach Process of Relaxation via a Real Intermediate State.	117
6.1.4 Jahn Teller Effect	118
6.1.5 Cross Relaxation Mechanisms	121
6.2 Results	122
6.2.1 Spin-lattice Relaxation Times	122
6.2.2 Spin-spin Relaxation Times	128
6.3 Discussion.....	128
6.4 References	131
APPENDIX 6A. The Strain Tensor.....	132
6A.1 One-dimensional strain.....	132
6A.2 Two-dimensional strain	133
6A.3 Three-dimensional strain	135
Chapter 7.....	137
Dynamic Nuclear Polarisation of Diamond: Solid State and Thermal Mixing Effects..	137
7.1 Theory.....	139
7.1.1 Background Theory of Dynamic Nuclear Polarisation	140
7.1.2 The Solid State Effect.....	143
7.1.3 Thermal Mixing Effect	145
7.1.4 Time Dependence of the Nuclear Polarisation.....	148
7.1.5 Nuclear Relaxation Times and Signal Enhancement	153
7.2 Results	158
7.2.1 Microwave Field (H_1) at X-Band	158
7.2.2 Microwave Field (H_1) at S-Band.....	159

7.2.3 The Line Shape Function $g(\omega)$	163
7.2.4 Signal Enhancement and Polarisation Rate as a Function of Field Offset from Resonance	165
7.2.5 Dependence of the Polarisation Rate on Impurity Concentration	171
7.2.6 Nuclear Signal Enhancement for DNP of Central and Hyperfine lines	173
7.3 Discussion.....	175
7.4 References	177
Chapter 8.....	179
Dynamic Nuclear Polarisation of Diamond: Nuclear Orientation via Electron Spin-Locking	179
8.1 Theory of Nuclear Orientation Via Electron–Spin Locking	181
8.2 Results	184
8.2.1 Field Offset from Resonance.....	184
8.2.2 Spin-Locking Pulse Amplitude and Phase	185
8.2.3 The Effect of Impurity Concentration on the NOVEL Polarisation Rate	188
8.2.4 NOVEL at Different Frequencies.....	189
8.2.5 Signal Intensity and Polarisation Rates for Pulsed and Continuous Wave DNP Techniques.....	191
8.3 Discussion.....	194
8.4 References	195
Chapter 9.....	197
Concluding remarks	197
9.1 Achievements	198
9.2 Recommendations	199

Chapter 1

Magnetic Resonance Studies in Diamond

A Literature Survey.



1.1 Basic Nuclear Magnetic Resonance of Diamond.....	24
1.2 Magnetic Resonance in Semiconducting Diamonds.....	28
1.3 Electron Paramagnetic Resonance in Diamond.....	29
1.4 References.....	30

1.1 Basic Nuclear Magnetic Resonance of Diamond

Magnetic resonance studies in diamond have, to a large degree, been concentrated in the field of electron paramagnetic resonance, mainly because of the large number of impurities that can be studied by this method. Nuclear magnetic resonance studies have been rather limited, probably due to very long relaxation times associated with ^{13}C nuclei in diamond. It is reported in this study and elsewhere that longitudinal relaxation times of many tens of hours are not uncommon. The time required to make a single spin-lattice relaxation time measurement runs into hundreds of hour per diamond and is, therefore, a very time consuming process.

Diamonds of gem quality give very narrow NMR lines of about 250 Hz half width at half height, even in solid state spectrometers. The diamond NMR spectrum is relatively simple, consisting of a strong central line at about 39 ppm above TMS (tetramethylsilane) and two weak satellite lines. The satellite lines are due to ^{13}C hyperfine interactions [1.1]. These satellite lines are only visible after enhanced polarisation of the diamond has been achieved using dynamic nuclear polarisation techniques. Wilke *et al.* [1.2] report that the diamond spectrum consists of a major resonance centred near 50 ppm above TMS and a smaller and broader resonance near 170 ppm below TMS. The major resonance is attributed to diamond type carbon nuclei and the other resonance is presumed to be due an aromatic type impurity. In the diamonds investigated in this study no such feature was observed around 170 ppm below TMS.

Of relevance to this study are the spin-lattice relaxation effects in diamond. Although there is a limited amount of work that has been done in this field, this aspect of diamond NMR will be reviewed here. Henrichs *et al.* [1.3] report on the relaxation of nuclear spins in diamond by the action of paramagnetic centres in the absence of spin diffusion. The gem diamonds used in their study produce spectra containing one ^{13}C line at 39 ppm from TMS and no evidence of multiple NMR lines in diamond was observed. The agreement

between experimental data and the theory of relaxation of non-communicating nuclear spins by paramagnetic centres indicates that this is the dominant relaxation mechanism in these diamonds. Similar experiments were carried out on synthetic diamond and relaxation times were found to be far shorter, most probably due to the presence of ferromagnetic impurities in synthetic diamonds [1.3].

In a recent study by Terblanche *et al.* [1.4], ^{13}C Zeeman spin-lattice relaxation in a suite of 5 natural diamonds was measured. These diamonds were of type Ia, Ib and IIa. This paper also attributes the ^{13}C spin-lattice relaxation mechanism to dipolar interactions between paramagnetic impurities and ^{13}C nuclei. It is reported that P1 type impurities, which are discussed in chapter 4, are chiefly responsible for ^{13}C relaxation in type Ia diamonds. It is also reported that P2 impurities are ineffective in relaxation of ^{13}C . In one sample, which had a low P1 impurity concentration, but contained a transition metal of spin $5/2$, the latter impurity seems to dominate the relaxation process. Good agreement between the theory and experiment was obtained. A difference between the work reported by Terblanche *et al.* [1.4] and Wilke *et al.* [1.2] is the inclusion of spin diffusion in the explanation of the observed behaviour by the former group.

The ^{13}C spin-lattice relaxation in two natural diamonds of type Ia and IIa were investigated at 4.7 tesla (T) by Reynhardt and Terblanche [1.5]. In this investigation the polarisation rate from zero to equilibrium as well as the depolarisation rate, from an enhanced polarisation state achieved by dynamic polarisation of the ^{13}C nuclei, was investigated. It was found that polarisation times are shorter than the depolarisation times. In terms of spin temperatures, the rate of cooling to the lattice temperature in a field of 4.7 T is faster than the rate of heating from a very low spin temperature (enhanced magnetisation) to the lattice temperature. Reynhardt and Terblanche [1.5] also performed an experiment where the enhanced magnetisation was first inverted and then allowed to relax to equilibrium. It was found that this relaxation time was shorter than the depolarisation time described above, but longer than the polarisation time from zero to equilibrium. Again, in terms of spin temperature, inverting the magnetisation results in a high negative spin temperature so that relaxation to the lattice temperature proceeds from

this negative temperature through zero to the temperature of the lattice. A qualitative explanation of the observed behaviour in terms of spin-lattice relaxation via paramagnetic impurities is offered.

Developments in the processes used in the production of synthetic diamond have enabled the production of diamond containing 100% ^{13}C , compared to the natural abundance of 1.1%. The first work reported on enriched diamonds was by Lefmann *et al.* [1.6], who performed NMR measurements on these crystals. It was found that the line shape was very sensitive to orientation of the external magnetic field relative to the crystallographic axes, which is typical of dipolar line broadening. With the magnetic field aligned with the [110] direction, the NMR line is broad and flat, whereas when the field is aligned with the [001] direction, a narrower gaussian line results.

In the [001] direction, all nearest neighbour bonds are at the same angle, i.e. $\theta = 54.7^\circ$ to the external field [1.6]. This is the famous magic angle where the term $(1 - 3\cos^2\theta)$ vanishes and the dipole interaction is zero [1.7]. In this orientation only next-nearest neighbours and further nuclei can contribute to line broadening. The line is therefore expected to be relatively narrow as the dipolar interactions fall off with distance r as $1/r^3$. This prediction is in accordance with the line shape observed by Lefmann *et al.* [1.6]. For the case where the external field is applied along the [110] direction, the angle between the field and the bonds no longer satisfies the magic angle condition. Consequently dipole interactions between these nearest neighbour nuclei contribute to line broadening, in agreement with the observed behaviour.

In the [111] direction a splitting of 8.5 kHz is observed [1.6]. This behaviour is explained as follows. Nuclei in the diamond structure are in a tetrahedral arrangement and when the field is applied along the [111] direction, one of the four nearest neighbour bonds is parallel to the field i.e. the central nucleus and one other. The angle between the field and this bond is therefore zero, $(\theta = 0)$, and the maximum dipolar interaction is experienced by these nuclei. The term, $(1 - 3\cos^2\theta)$, describing the dipolar interaction, is therefore

maximised. The angle between the bond directions of the remaining 3 nuclei with the central nucleus and the field, results in lower dipolar interaction and hence a splitting of the ^{13}C NMR line. This situation corresponds to the conditions necessary for line splitting by the mechanism known as “Pake’s doublet” [1.8]. A doublet is indeed what was observed by Lefmann *et al.* [1.6].

Longitudinal and rotating frame ^{13}C spin-lattice relaxation of two enriched diamonds was reported by Schaumberg *et al.* [1.9]. One was a clear high purity diamond and the other a lower purity greenish diamond. The impurity concentration in the second diamond was estimated to be about 10^{17} cm^{-3} . The spin-lattice relaxation time results reported in this study indicate that the spin-lattice relaxation times for these two diamonds differ by two orders of magnitude i.e. 1800 seconds for the pure diamond compared to 16 seconds for the greenish diamond [1.9]. This behaviour is ascribed to relaxation via paramagnetic impurities in agreement with the conclusions of previously quoted authors [1.3-6].

The rotating frame spin-lattice relaxation times was only measured for the impure diamond. The results indicate that there are two mechanisms involved. The relaxation times were $T_{1\rho}^i = 4.5 \pm 1.5$ ms and $T_{1\rho}^r = 745 \pm 5$ ms. Initially, the magnetisation decreases by rapid dephasing of the nuclear magnetic moments without exchange of energy with the lattice. Later, the spin temperature changes as the energy is exchanged with the lattice according to the expression:

$$\frac{dM}{dt} = \frac{1}{T_{1\rho}}(M_0 - M). \quad 1.1$$

Schaumberg *et al.* [1.9] also report on the orientation dependence of the NMR spectra of these enriched diamonds in agreement with the behaviour observed by Lefmann *et al.* [1.6].

1.2 Magnetic Resonance in Semiconducting Diamonds

A study of the nuclear spin-lattice relaxation of dilute spins in semiconducting diamond was reported by Hoch and Reynhardt [1.10]. Absorption line shape and spin-lattice relaxation time measurements were made on ^{13}C nuclei (1.1% abundance) in a type IIb single crystal semiconducting diamond.

The line shape observed for this diamond is in good agreement with the truncated Lorentz line shaped predicted by Van Vleck for dilute spin systems [1.10].

Spin-lattice relaxation times of the order of 3 to 4 hours were observed in this diamond. Although this is a relatively long relaxation time for diamond, it is at least an order of magnitude shorter than that for a type IIa diamond. This behaviour suggests that the boron acceptor centres play an important role in the spin-lattice relaxation of type IIb diamonds. The temperature dependence of the spin-lattice relaxation time was measured in the temperature range from 273 to 375 K. The observed temperature dependence is explained in terms of a model in which spin diffusion plays a role. Paramagnetic centre relaxation is ascribed to an Orbach process involving excited states near the valence band [1.10].

The electron paramagnetic resonance spectrum of semiconducting diamond is discussed in a paper by Ammerlaan and van Kemp [1.11]. The detection of an EPR spectrum from a semiconducting diamond is a rather difficult measurement to perform and requires low temperatures ($T < 4\text{ K}$) and a large uniaxial stress ($P \approx 1\text{ GPa}$). The spectrum is analysed with an effective $3/2$ spin and a Hamiltonian including terms depending on the magnetic field and the strain. The resonance is associated with the neutral acceptor boron in these diamonds and the width of the resonance is attributed to random internal strain [1.11].

1.3 Electron Paramagnetic Resonance in Diamond

A large number of defects in diamond have been reported and many of these have been discovered and modelled using EPR techniques (e.g. [1.12]). A detailed review of the literature in this field of diamond research is beyond the scope of this thesis but relevant studies are however discussed in chapter 4. Loubser and van Wyk [1.13] give the salient features of diamond that make it an interesting material to explore by EPR techniques. They state that the electrical, optical and other properties of diamond are very sensitive to small amounts of impurities. Electron paramagnetic resonance is one of the most sensitive and powerful tools for the investigation of these impurities. It is also possible to study one impurity in the presence of others even if they are in much higher concentration. This is usually not possible using other techniques.

Many of the studies of impurities have been carried out after exposure to ionising radiation that create defect centres like vacancies, interstitials and aggregations. The manner in which the defects are introduced and removed and how they affect the physical properties of diamond are used in their identification [1.13].

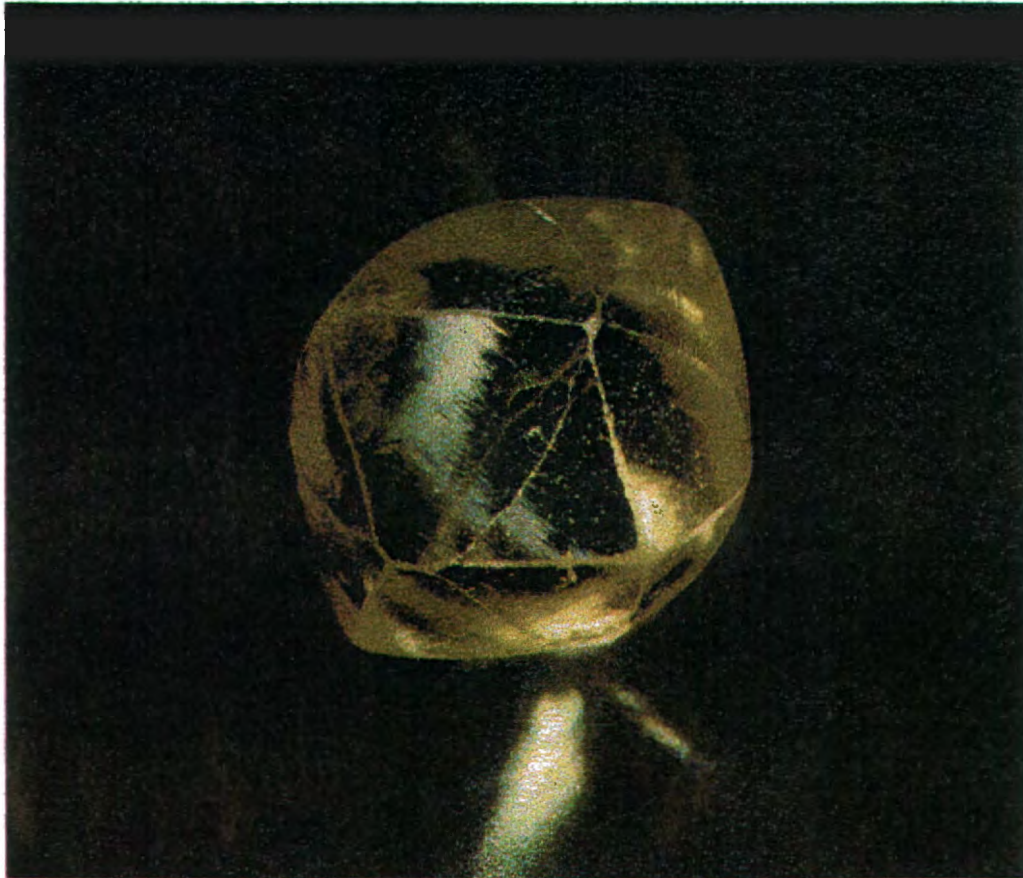
Research into defects in diamond has not been as rapid as, for example in silicon and ZnS, but the unique properties of diamond, such as hardness, high Debye temperature, large refractive index and large forbidden gap (5.7 eV), will continue to be a motivation and source of interesting research [1.13].

1.4 References

- [1.1] M.J.R. Hoch, G.J. Hill and J. Wu, *Fine Structure in Dynamic Nuclear Polarization Spectra from Natural Diamond.*, Invited lecture, Eleventh International Conference on Hyperfine Interactions, Durban, (1998). Submitted to Hyperfine Interactions.
- [1.2] C. A. Wilke, T. C. Ehlert and D. T Haworth, *J. Inorg. and Nucl. Chem.* **40**, 1985, (1978).
- [1.3] P. M. Henrichs, M. L. Cofield, R. H. Young and J. M. Hewitt, *J. Magn. Res.*, **58**, 85, (1984).
- [1.4] C. J. Terblanche, E. C. Reynhardt and J. A. van Wyk, Submitted for publication to *J. Chem. Phys.* (1998).
- [1.5] E C Reynhardt and C J Terblanche, *Chem. Phys. Let.*, **296**, 464, (1997).
- [1.6] K. Lefmann, B. Buras, E. J. Pedersen, E. S. Shabanova, P. A. Thorsen, F. B. Rasmussen and J. P. F. Sellschop, *Phys. Rev. B*, **50**, 623, (1994).
- [1.7] G. E. Pake and E. M. Purcell, *Phys. Rev.*, **74**, 1984, (1948).
- [1.8] G. E. Pake, *J. Chem. Phys.*, **16**, 327, (1948).
- [1.9] K. Schaumberg, E. Shabanova, J. P. F. Sellschop and T. Anthony, *Solid State Comm*, **91**, No. 9, 739, (1994).
- [1.10] M. J. R. Hoch and E. C. Reynhardt, *Phys. Rev. B*, **37**, 222, (1988).
- [1.11] C. J. Ammerlaan and R. van Kemp, *J. Phys. C: Solid State Phys.* **18**, 2623, (1985).
- [1.12] J. M. Baker and M. E. Newton, *Appl. Magn. Reson.*, **8**, 207, (1995).
- [1.13] J. H. N. Loubser and J. A. van Wyk, *Rep. Prog. Phys.*, **41**, 1201, (1978).

Chapter 2

Apparatus



2.1 Introduction.....	32
2.2 S-Band Dynamic Nuclear Polarisation System.....	33
2.3 X-Band Dynamic Nuclear Polarisation System and Electron Paramagnetic Resonance Spectrometer	36
2.4 Nuclear Magnetic Resonance Spectrometer	38
2.5 Low Temperature Equipment	39
2.6. References.....	40

2.1 Introduction

The main focus of this study is dynamic nuclear polarisation (DNP) of diamond and the equipment used in this study is described in this chapter. Most of the work done previously in this field has been carried out in systems where the DNP treatment and NMR measurements were conducted in the same system and hence at the same field. For example, Duivestijn *et al.* [2.1] used a system that included a Bruker CXP4-100 pulsed spectrometer operating at a ^{13}C nuclear magnetic resonance frequency of 15 MHz. This equates to a field of 1.5 T and a corresponding DNP frequency of 39.49 GHz. In the current investigation, the DNP processes and the NMR measurements were carried out in two completely independent systems. This arrangement allowed the DNP treatment to be applied at much lower frequencies than would have been possible if the DNP treatment and the NMR measurements were carried out at the same field i.e. at 4.7 T. Two frequencies bands were utilised in this investigation viz. s-band and x-band. A description of these systems is given in sections 2.2 and 2.3.

It is interesting to note that the NMR measurements were carried out in a field of 4.7 T and had the DNP process been applied in the same system, a DNP frequency of 134 GHz would have been required. This would have been prohibitive due to the very high cost of equipment at this frequency. In addition to this limitation, resonant cavities, and hence sample sizes, are very small at this frequency. In the example given above, the cavity length would be limited to about one wavelength i.e. $\lambda \approx 2\text{ mm}$. To ensure that samples are only exposed to the magnetic field component of the microwave radiation, they would be limited to a fraction of a millimetre.

The effectiveness of the DNP process under various conditions is determined via the measurement of the ^{13}C NMR signal strength. A brief description of the Bruker DSX 200 Avance spectrometer used in these measurements is given in section 2.4.

The effect of temperature on the paramagnetic impurity relaxation times was also investigated and a description of the Oxford Instruments system that facilitated measurement to 4.3 K is given in section 2.5

2.2 S-Band Dynamic Nuclear Polarisation System

The frequency range defined as s-band is from 2 GHz to 4 GHz and is determined by the pass band of s-band wave-guide. The actual frequency used was 2.35 GHz which corresponds to the licensed industrial heating frequency. This frequency was chosen due to the availability and relatively low cost of hardware.

This system consisted of a microwave transmitter, a high power klystron amplifier, a resonant cavity and a high power matched load into which the reflected power could be dumped. This list of items, bar a detector, makes up a typical EPR spectrometer, but unfortunately EPR spectroscopy is not possible in this system for the following reasons:

1. The relatively low frequency, or long wavelengths associated with s-band, leads to very large resonant cavities and hence low filling factors.
2. No field modulation was available.
3. EPR signals are very small due to the Boltzman distribution at magnetic fields of around 850 G.
4. Static field homogeneity was not very good.

There was therefore no feedback mechanism in this system to determine the exact position of the EPR resonance and a trial and error approach had to be adopted to identify the resonance field.

Photographs of the s-band magnet and resonance cavity are shown in figure 2.1 and a photograph of the klystron amplifier is shown in figure 2.2.

Figure 2.1. S-band DNP system. The magnet, wave guide and cavity are shown.



Figure 2.2. Klystron amplifier used in the s-band DNP system



In order to carry out pulsed DNP experiments at s-band, the pulse programming facility of the NMR spectrometer was used. Pulses were programmed on the spectrometer, which resulted in a direct current level (or DC signal) being transmitted to the microwave generator for the duration of the pulse. The pulse programming system was limited to three pulses viz.:

1. Zero DC level – no pulse or a time delay.
2. DC level – pulse 1 with 0° phase.
3. DC level – pulse 2 with 90° phase

Although this system had limitations, it was adequate for the investigation of the solid state and thermal mixing effects as well as nuclear orientation via electron spin locking (NOVEL), at this frequency.

2.3 X-Band Dynamic Nuclear Polarisation System and Electron Paramagnetic Resonance Spectrometer

A Bruker ESP380E pulsed electron paramagnetic resonance (EPR) spectrometer was used in measurements of the paramagnetic impurity relaxation times and in the investigation of DNP effects at x-band. The system consists of a standard continuous wave type microwave bridge, a pulse generator, electromagnet, 1 kW travelling wave tube (TWT) amplifier and console. A photograph of the Bruker ESP380E spectrometer is shown in figure 2.3.

Figure 2.3. Bruker ESP 380E pulsed EPR spectrometer



Relaxation times and DNP experiments were carried out in two x-band EPR cavities, the one being a standard rectangular cavity and the other a low Q dielectric resonator that is inserted into a cryostat allowing measurement down to 4.3 K. Photographs of cavities are shown in figures 2.4 and 2.5.

Figure 2.4. Standard rectangular x-band EPR resonator.



Figure 2.5. X-band low Q dielectric resonator and cryostat.



2.4 Nuclear Magnetic Resonance Spectrometer

Nuclear magnetic resonance measurements were carried out on a Bruker DSX 200 Avance spectrometer. This spectrometer is a member of the range of digital spectrometers manufactured by Bruker Analytik, that provides for ease of use and high performance in terms of pulse programming, data acquisition and signal processing. This particular spectrometer operates at 200 MHz for protons in a corresponding magnetic field of 4.7 T. A photograph of the spectrometer is shown in figure 2.6. The NMR measurement probe that was used in these measurements was a standard 50 MHz (^{13}C) probe that was adapted for use in the super wide bore (SWB) magnet.

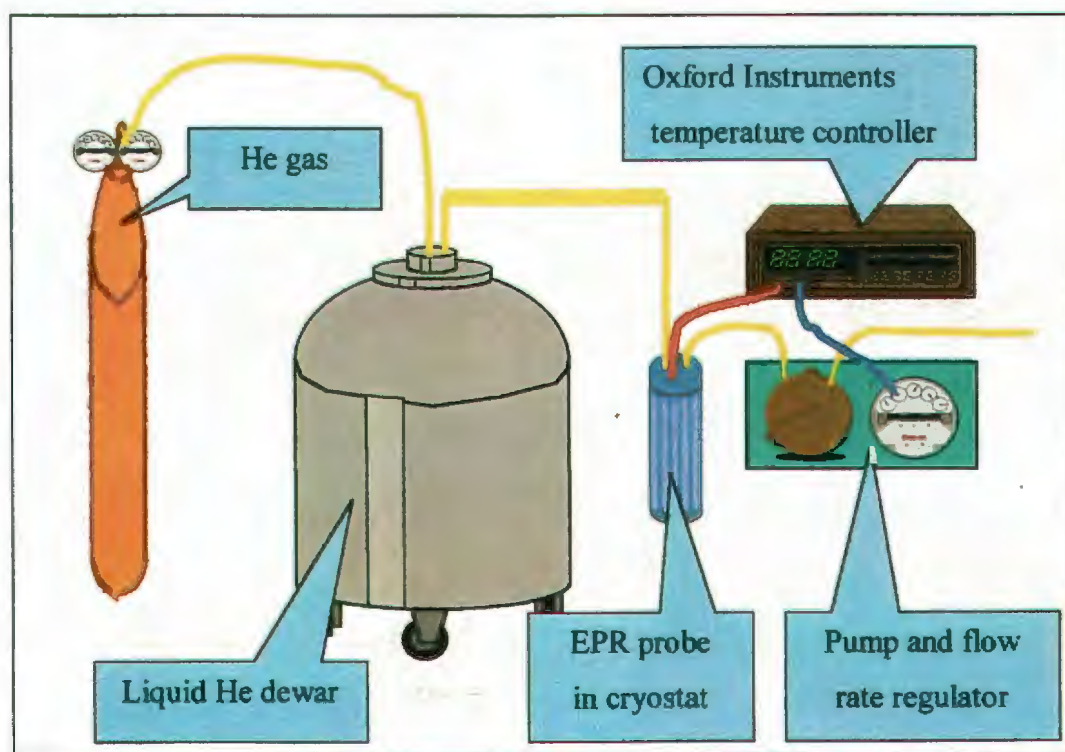
Figure 2.6. Bruker Avance DSX 200 nuclear magnetic resonance spectrometer.



2.5 Low Temperature Equipment

Low temperature EPR measurements were carried out using the Bruker ESP380E spectrometer and the low Q dielectric resonator. An Oxford Instruments ITC 500 series controller and cryogenic pump facilitated the temperature control. A diagram of the cooling circuit is shown in figure 2.7.

Figure 2.7. Cryogenic cooling circuit used in the low temperature measurements.



The basic method of operation of this system is as follows:

1. A required temperature or set point is entered into the temperature controller.
2. The set point is compared to the temperature measured by a thermocouple.

3. If the set point is lower than the measured temperature, liquid helium is sucked through the cryostat until the temperature is reached.
4. The liquid helium flow rate is then cut back by the controller to a rate where the set point temperature is maintained. This system is capable of controlling the temperature to within 0.1 K of the set point.
5. If the set point is higher than the measured temperature, the liquid helium flow rate is cut back completely and a heater is switched on.

2.6. References

- [2.1] M. J. Duivestijn, C. van der Lugt, J. Smidt and R. A. Wind, *Chem. Phys. Lett.* **102**, (1983).

Chapter 3

Experimental Techniques



3.1 The Nutation Experiment	43
3.2 Spin-Spin Relaxation Time Measurements	47
3.2.1 Pulse Sequences	47
3.2.2 Pulse Lengths and Delay Times	48

3.2.3 Low Temperature Spin-Spin Relaxation Time Measurements.....	50
3.3 Spin-Lattice Relaxation Measurements.....	50
3.3.1 Pulse Sequences	50
3.3.2 Pulse Lengths and Delay Times.....	52
3.3.3 Low Temperature Spin-Lattice Relaxation Time Measurements	54
3.4 Rotating Frame Spin-lattice Relaxation Time Measurements.....	54
3.4.1 Pulse Sequences	54
3.4.2 Pulse Lengths and Delay Times.....	56
3.5 Continuous Wave Dynamic Nuclear Polarisation at X-Band.....	58
3.6 Continuous Wave Dynamic Nuclear Polarisation at S-Band	60
3.7 NOVEL at X-Band.....	62
Figure 3.12. NOVEL pulse sequence.....	64
3.8 NOVEL at S-Band.....	66
3.9 Nuclear Polarisation Enhancement	67
3.10 The Dipolar Reservoir	68
3.11 Nuclear Magnetic Resonance Measurements	69
3.11.1 Nuclear Magnetic Resonance Pulse Sequences	70
3.11.2 Nuclear Magnetic Resonance Signal Processing	70
3.11.3 Probe Head Tuning.....	70
3.12 EPR Measurements	71
3.12.1 EPR Line Width Measurements.....	71
3.12.2 Electron Paramagnetic Resonance Spectra.....	71
3.12.3 Electron Relaxation Times.....	73
3.13 References.....	75

3.1 The Nutation Experiment

The length of a pulse is determined by its duration and power and the nutation experiment is used to measure the exact pulse length (or power and duration). The experiment is usually used to determine the length of a $\pi/2$ pulse. The pulse sequence used in the nutation experiment is essentially a pulse-echo sequence where the length of the excitation pulse t_{excite} , is increased, stepwise. Increasing the length of the excitation pulse has the effect of altering the phase and amplitude of the resulting echo. The nutation pulse sequence is described by the sequence: $[t_{excite} - \tau - t_{detection} - \tau - echo]$, where τ is a time delay between the pulses. These experiments were carried out mainly on the Bruker ESP380E spectrometer and the pulse sequence was programmed in the pulse tables. Examples of the pulse programs for the +x and Signal Digital Integrator (SDI) channels are shown in figures 3.1a and 3.1b below.

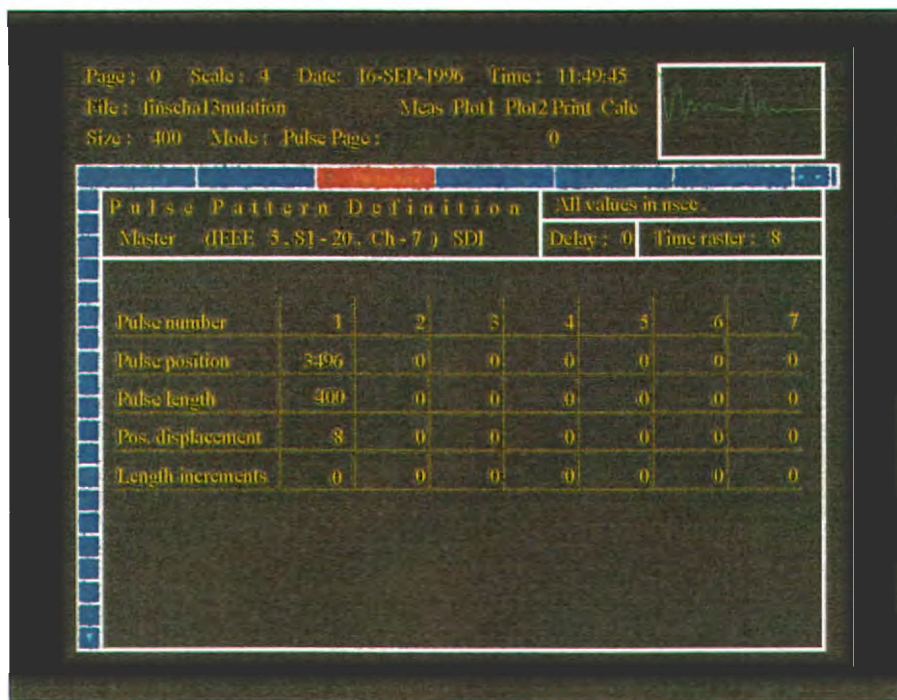
Figure 3.1a. Nutation experiment: +x pulse sequence programmed in the Bruker ESP380E graphic user interface (GUI) tables.

Page: 0 Scale: 4 Date: 16-SEP-1996 Time: 11:49:45
 File: fmscha13nutation Meas Plot1 Plot2 Print Calc
 Size: 400 Mode: Pulse Page: 0

Pulse Pattern Definition All values in nsec.
 Master: (IEE: 9, SI - 20, (Ch - 7) + 8) Delay: 2 Time raster: 8

Pulse number	1	2	3	4	5	6	7
Pulse position	288	1832	0	0	0	0	0
Pulse length	48	48	0	0	0	0	0
Pos. displacement	0	8	0	0	0	0	0
Length increments	8	0	0	0	0	0	0

Figure 3.1b. Nutation experiment: SDI pulse sequence programmed in the Bruker GUI tables.

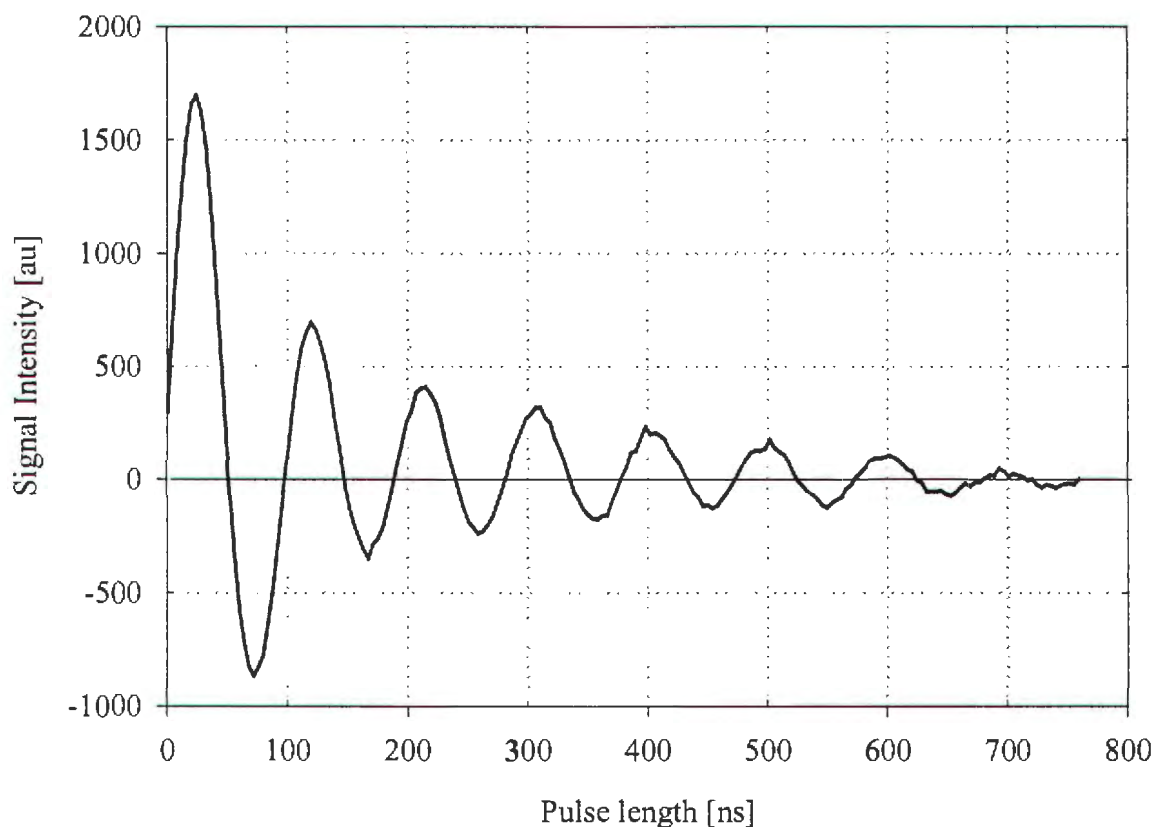


The data acquired in these experiments are in the form of the integral of the echo as a function of the pulse length and data are fitted to the equation that describes the electron magnetisation under the nutation pulse sequence conditions, i.e.:

$$m = m_0 \exp\left(-\frac{t}{T_{2e}}\right) \sin(\gamma_e H_1 t + \theta) \quad 3.1$$

An example of the results of a typical nutation experiment carried out at x-band is given in figure 3.2a.

Figure 3.2a. Nutation experiment performed at x-band.



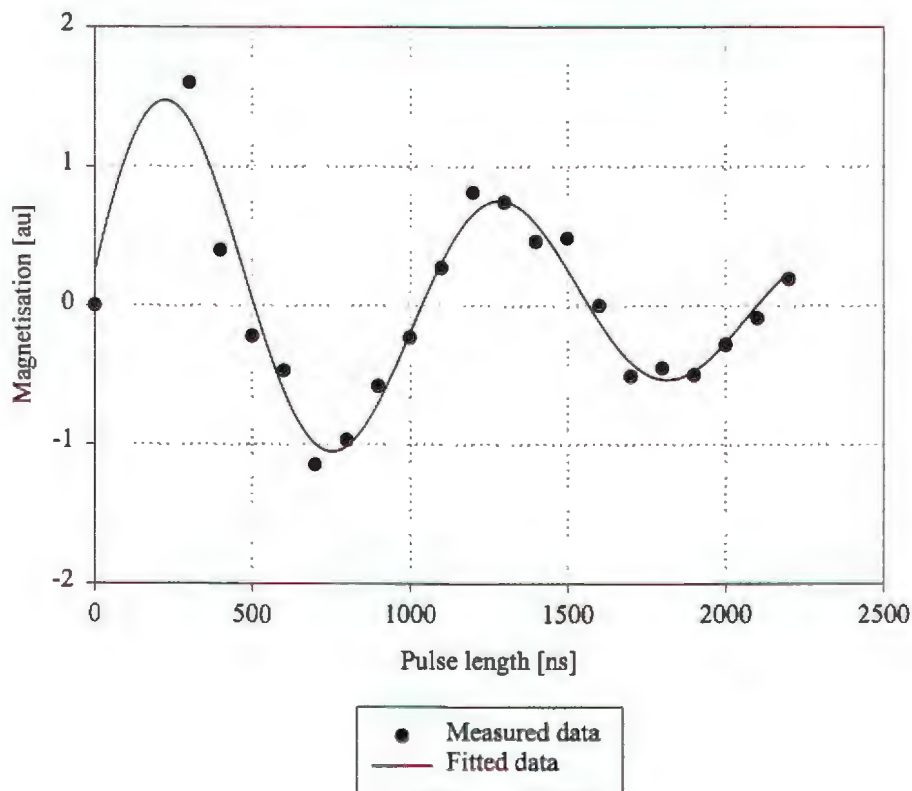
Performing the nutation experiment at s-band required an indirect observation of the effect of increasing the initial pulse. This experiment involved apply the NOVEL DNP process, described in chapter 8, for various initial pulse lengths and then observing the effect via the ^{13}C NMR signal. An example of a s-band nutation experiment is shown in figure 3.2b. The parameters estimated in fitting equation 3.1 to the measured data are listed in table 3.1:

Table 3.1. Parameters obtained from a best fit of equation 3.1 to the data displayed in figure 3.2.

Parameter	Fitted value
m_0 [au]	1.707
H_1 [G]	0.34
θ [rad]	0.147
T_{1e} [us]	1.572
R^{2*}	0.933

* R^2 is the square of correlation coefficient obtained for the fit of the experimental data and the theoretical equation 3.1.

Figure 3.2b. Nutation experiment result at s-band. The $\pi/2$ pulse length is 266 ns.



When the nutation experiment is carried out at a fixed power level, the value of H_1 is fixed, and the exact duration of the $\pi/2$ pulse is then determined from:

$$\frac{2\pi}{4\tau_{\frac{\pi}{2}}} = \omega_e = \gamma_e(H_1)_{\frac{\pi}{2}}. \quad 3.2$$

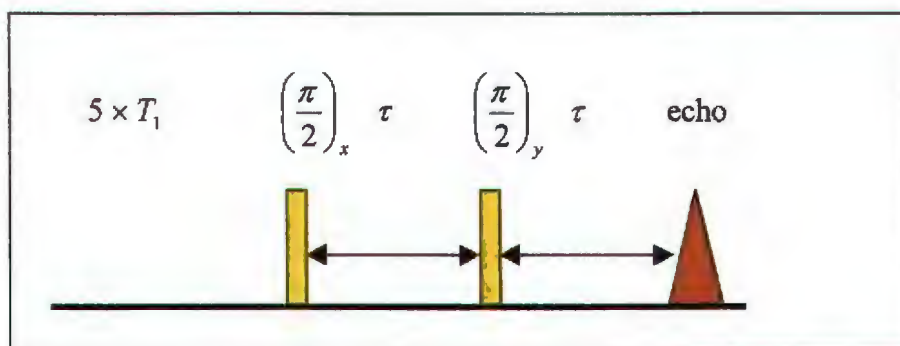
Inserting $H_1 = 0.34$ G (table 3.1), into equation 3.2 yields $\tau_{\pi/2} \approx 266$ ns .

3.2 Spin-Spin Relaxation Time Measurements

3.2.1 Pulse Sequences

The pulse sequence used to measure spin-spin or transverse relaxation times T_{2e} is shown in figure 3.3.

Figure 3.3 Spin-spin relaxation time (T_{2e}) pulse sequence.



In this sequence, the time, τ , between the excitation pulse, $(\pi/2)_x$, and the detection pulse, $(\pi/2)_y$, as well as the time between the detection pulse and the echo are varied. In these experiments, the integral of the echo is recorded as a function of the pulse separation and is fitted to the equation:

$$M(t) = M_0 \exp\left(\frac{-\tau}{T_{2e}}\right), \quad 3.3$$

which describes the behaviour of the electron magnetisation under the T_{2e} pulse sequence conditions. In the curve fitting procedure, a Marquard algorithm, supplied with the Bruker ESP380E spectrometer, was utilised.

Alternatively, the data can be plotted as the natural logarithm of the magnetisation as a function of τ . This plot results in a straight line with slope $-1/T_{2e}$, as can be seen from the equation below:

$$\ln\left(\frac{M(t)}{M_0}\right) = \left(-\frac{1}{T_{2e}}\right)\tau. \quad 3.4$$

The spin-spin relaxation time, T_{2e} , determined experimentally was used to calculate the paramagnetic impurity concentrations, C_e . This calculation is dealt with in detail in chapter 5.

3.2.2 Pulse Lengths and Delay Times

These experiments were conducted on the Bruker EPR system at x-band. Programming of the pulse sequence was done in the pulse programming tables that were described in section 3.1. An example of the pulse program, showing the pulse lengths and positions of the +x and the SDI channels, are given in figures 3.4a and 3.4b.

Figure 3.4a. Spin-spin relaxation time: +x pulse sequence programmed in the Bruker GUI tables.

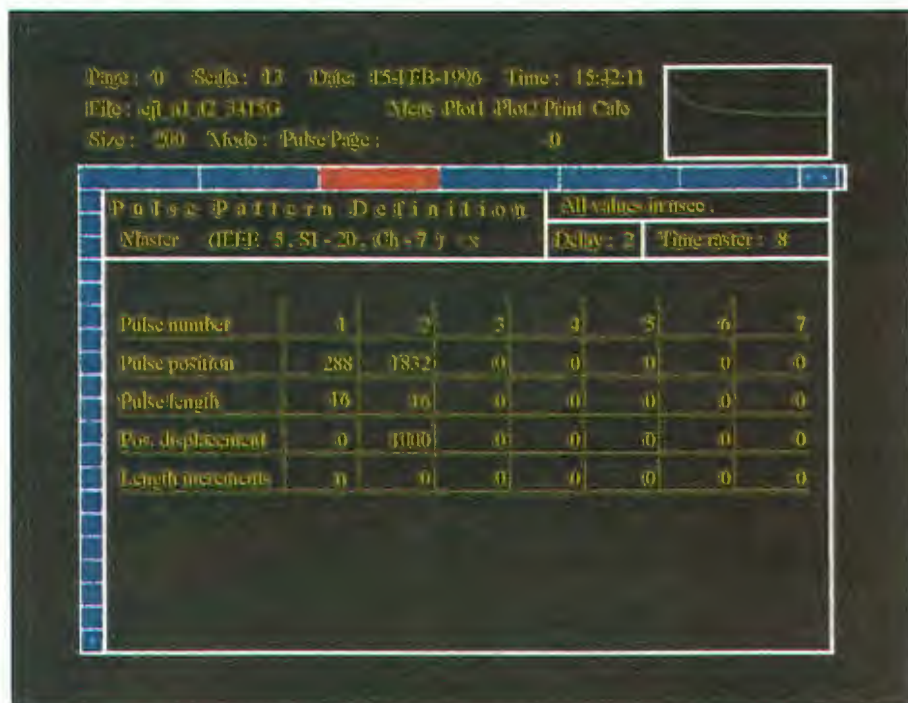
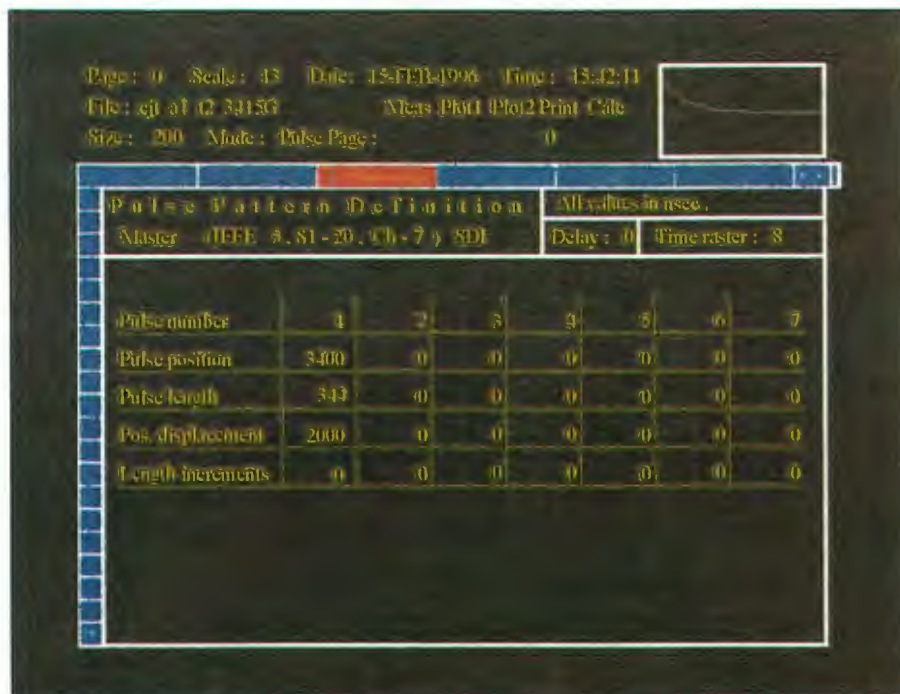


Figure 3.4b. Spin-spin relaxation time: SDI window programmed in the Bruker GUI tables.



As can be seen in figure 3.4a, the separation of the excitation and detection pulses begins at 1544 ns and is then increased in 1000 ns steps up to a few hundred microseconds. Since all spin-spin relaxation times fell in the microsecond range, these values could be used quite generally.

3.2.3 Low Temperature Spin-Spin Relaxation Time Measurements

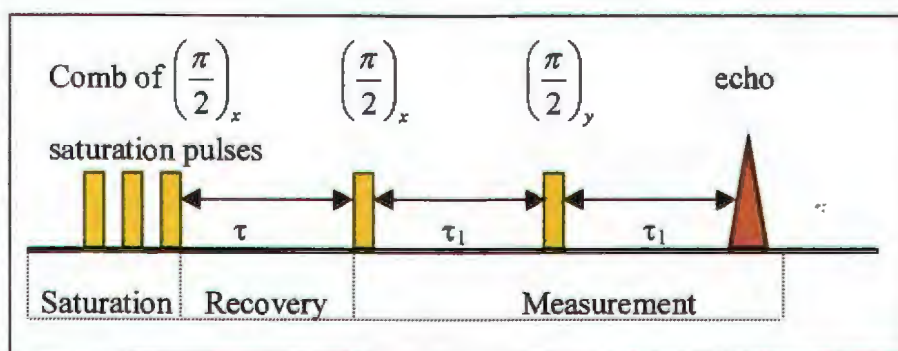
The effect of temperature on the spin-spin relaxation time was measured using the Bruker low Q dielectric resonator and cryostat that were discussed in Chapter 2. In these experiments the spin-spin relaxation time pulse sequence was applied at regular temperature intervals between room temperature and 4.3 K.

3.3 Spin-Lattice Relaxation Measurements

3.3.1 Pulse Sequences

A simple saturation recovery pulse sequence was used to measure the spin-lattice relaxation times. This pulse sequence is shown diagrammatically below:

Figure 3.5. T_1 pulse sequence



A subtlety in this pulse sequence that can lead to some misunderstanding is that it is essentially made up of the following pulses:

$$[n(\pi/2)_x - \tau - (\pi/2)_x - \tau_1 - (\pi/2)_y - \tau_1 - \text{echo}],$$

whereas the most common method of generating an echo in NMR is to use the pulse sequence:

$$[(\pi/2)_x - \tau - (\pi)_x - \tau - \text{echo}].$$

Since the bandwidth of the EPR pulse is narrower than the EPR line width, not all of the spins are excited by the first pulse. Therefore applying a second pulse with twice the length of the first, has no benefit. This is due to the fact that a longer pulse will have an even narrower bandwidth and will therefore interact with fewer spins i.e. narrower range of Larmor frequencies. In reality the optimum length of the two pulses is about $2\pi/3$, but explanation of the processes is much easier following the classic solid echo pulse sequence:

$$[(\pi/2)_x - \tau - (\pi/2)_y - \tau - \text{echo}].$$

The data acquired in this manner, i.e. integrated signal intensity as a function of τ was recorded and fitted to the equation:

$$M(\tau) = M_0 \left[1 - \exp\left(\frac{-\tau}{T_{1e}}\right) \right], \quad 3.5$$

where $M(\tau)$ is the integrated signal intensity after a time τ , M_0 the saturation magnetisation and T_{1e} the spin-lattice relaxation time. Fitting this equation to the measured data was done using the Marquard algorithm.

3.3.2 Pulse Lengths and Delay Times

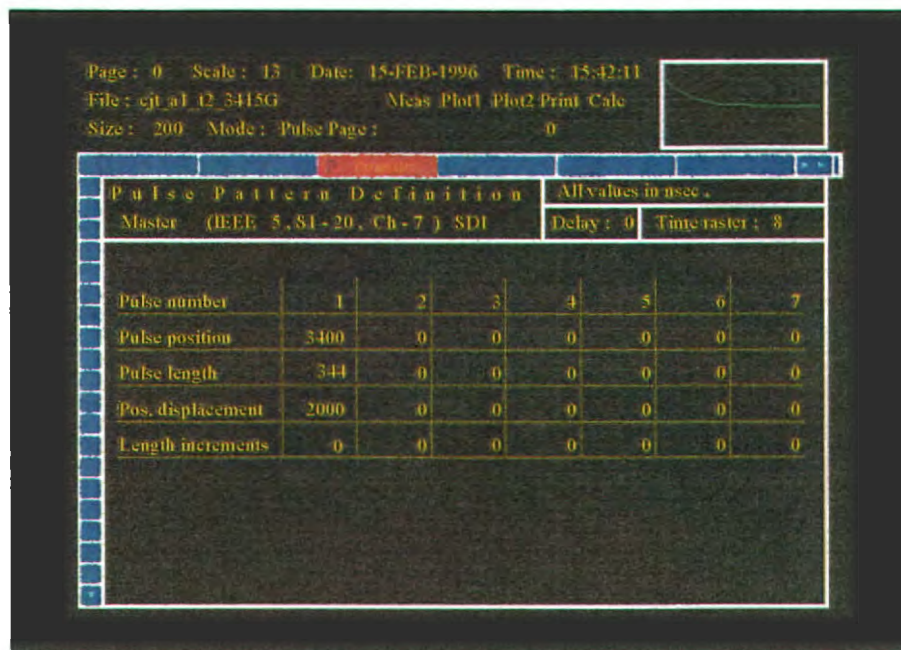
These experiments were also conducted at x-band, using the Bruker EPR spectrometer. This system requires different pulse programming methods for spin-lattice times up to 250 μs (T_{1e} short) and those longer than 1 ms (T_{1e} long). The system therefore suffers from a shortcoming in that T_{1e} 's falling into the range 250 μs to 1 ms cannot be measured accurately. The T_{1e} short pulse sequences are programmed in the tables in a similar way to that described for spin-spin relaxation times. Examples of typical T_{1e} short program tables are shown in figures 3.6a and 3.6b for the +x and SDI windows, respectively.

Figure 3.6a. Spin-lattice relaxation time: +x pulse sequence programmed in the Bruker GUI tables.

Page: 0 Scale: 18 Date: 13-FEB-1996 Time: 16:37:23
 File: ejt b4 d1 3467G Meas Plot1 Plot2 Print Calc
 Size: 200 Mode: Pulse Page: 0

Pulse Pattern Definition		All values in nsec.					
Master (IEEE 5, S1-20, Ch-7) +x		Delay: 2	Time raster: 8				
Pulse number	1	2	3	4	5	6	7
Pulse position	288	1768	0	0	0	0	0
Pulse length	16	16	0	0	0	0	0
Pos. displacement	0	0	0	0	0	0	0
Length increments	0	0	0	0	0	0	0

Figure 3.6b. Spin-lattice relaxation time: SDI window programmed in the Bruker GUI tables.



In the case of longer $T_{1\rho}$'s, a pulse programming system known as "Pulspel", must be used. An example of a " $T_{1\rho}$ long" program is given below.

```

;
;
; long T1 by rep rate saturation
;
;
begin defs
  dim s[100,1] ; dimension of data array [sx,sy]
end defs
;
;
begin lists
  asg1 +a ; sign program RE part
  bsg1 +b ; sign program IM part
end lists
;
;
begin exp [SDI QUAD intg] ; QUADrature detection with SDI
srt=10*srtu
  for x=1 to sx ;sweep loop
    dx=srt
    shot i=-2 to h ; accumulation loop
      p0 [+x] ; 1st pulse in +x channel
      d1 ; constant pulse separation
  
```

```

    p0 [+x]           ; 2nd pulse in +x channel
    d0                ; constant acquisition delay
    acq [sg1]        ; data acq with sign progr. sg1
  next i             ; end of accumulation loop
    b=c*srtu
    srt=srt+b
  next x             ;end of sweep loop
;
end exp

```

This pulse sequence was used when measuring T_{1e} at low temperatures where these times becomes exceeding long. This measurement method also has an upper limit of T_1 's of about 0.5 seconds. For longer T_1 's a manual method was devised and experiments were performed as follows. The sample was allowed to relax from zero magnetisation after a saturation pulse comb for a set time and then a single shot (pulse-echo) measurement made. The resulting echo integral was recorded on a digital storage oscilloscope and the signal intensity recorded as a function of time.

3.3.3 Low Temperature Spin-Lattice Relaxation Time Measurements

The effect of temperature on the spin-lattice relaxation time was measured in the same way as described in section 3.2.3, using the Bruker low Q dielectric resonator and cryostat (section 2.4). In these experiments the appropriate spin-lattice relaxation time pulse sequence was also applied at regular temperature intervals between room temperature and 4.3 K.

3.4 Rotating Frame Spin-lattice Relaxation Time Measurements

3.4.1 Pulse Sequences

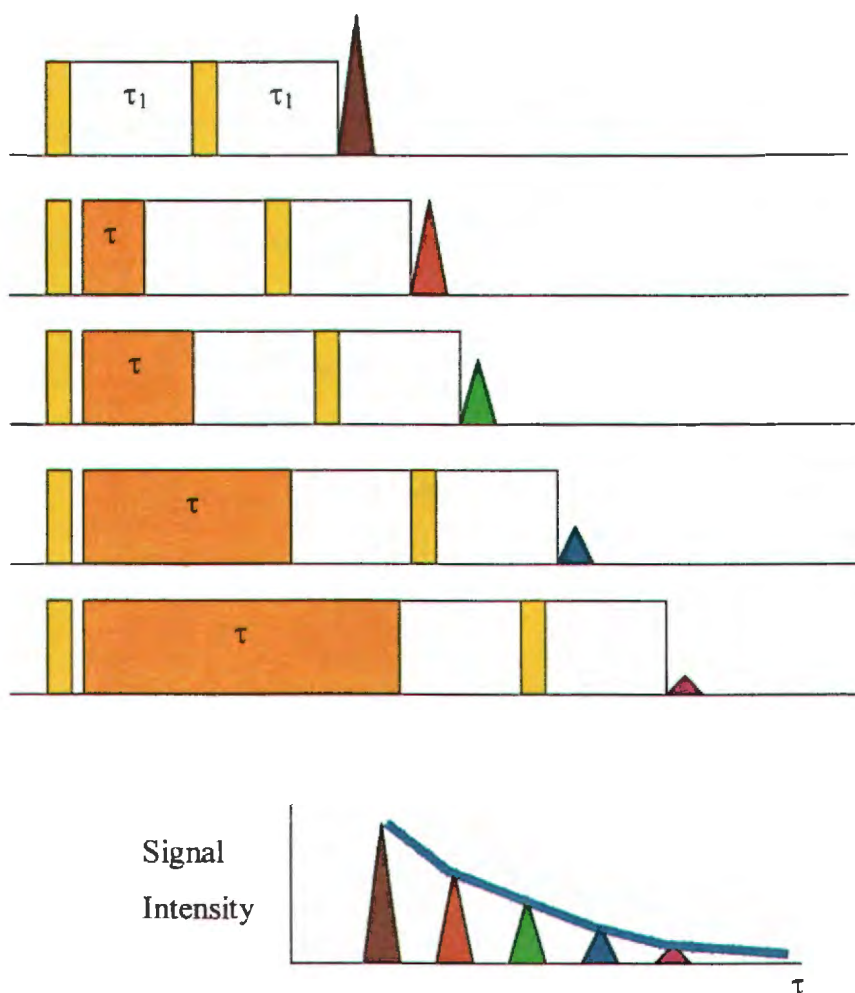
The measurement of the spin-lattice relaxation time in the rotating frame involves rotating the magnetisation into the x - y plane and then applying a second pulse that is shifted in phase by $\pi/2$ and of variable length [3.1]:

$$[(\pi/2)_x - (\tau)_y - (\pi/2)_y - \tau_1 - \text{echo}].$$

The second pulse is applied at the Larmor frequency so rotates at the same precession frequency as the magnetisation M_0 . Viewed from the rotating frame the magnetisation and the H_1 associated with the pulse appears to be stationary and the magnetisation only experiences H_1 and not H_0 . H_1 is now analogous to the H_0 and the magnetisation is said to be spin-locked. Immediately after the application of the first pulse, the magnitude of magnetisation is M_0 and is parallel to H_1 , which is much smaller than H_0 . The magnetisation will relax to a new equilibrium magnetisation M at a rate that is given by the time constant $T_{1\rho}$. This relaxation rate will be affected by motions at the Larmor frequency in the rotating reference frame and is therefore sensitive to motion in the MHz range rather than the GHz range. The same information could in theory be acquired by performing standard T_{1e} experiments at very low fields but the lack of sensitivity due the Boltzmann distribution factor precludes such measurements. The $T_{1\rho}$ technique maintains the sensitivity of the high field, but allows the investigation of much slower motions.

Measurement of $T_{1\rho}$ is accomplished by varying the length of the spin locking pulse and measuring the residual magnetisation in the x - y plane, parallel to the y -axis as a function of the spin-locking pulse length. Figure 3.7 demonstrates the measurement process.

Figure 3.7. Diagram of the $T_{1\rho}$ measurement process.



The blue line in figure 3.7 represents the decay of the electron magnetisation (integral of the resulting echo) as a function of the spin-locking pulse length and is given by:

$$M(\tau) = M_0 \exp\left(-\frac{\tau}{T_{1\rho}}\right) \quad 3.6$$

3.4.2 Pulse Lengths and Delay Times

The pulse sequence programmed in the $+x$, $+<x>$ and SDI channels that was used to measure the relaxation time in the rotating frame, is shown in figure 3.8a, b and c.

Figure 3.8a. Spin-lattice relaxation time in the rotating frame: +x pulses programmed in the Bruker GUI tables.

Page: 0 Scale: 14 Date: 2-JUN-1997 Time: 15:42:32
 File: T1rho_exp_ejtb2 Meas Plot1 Plot2 Print Calc
 Size: 200 Mode: Pulse Page: 0

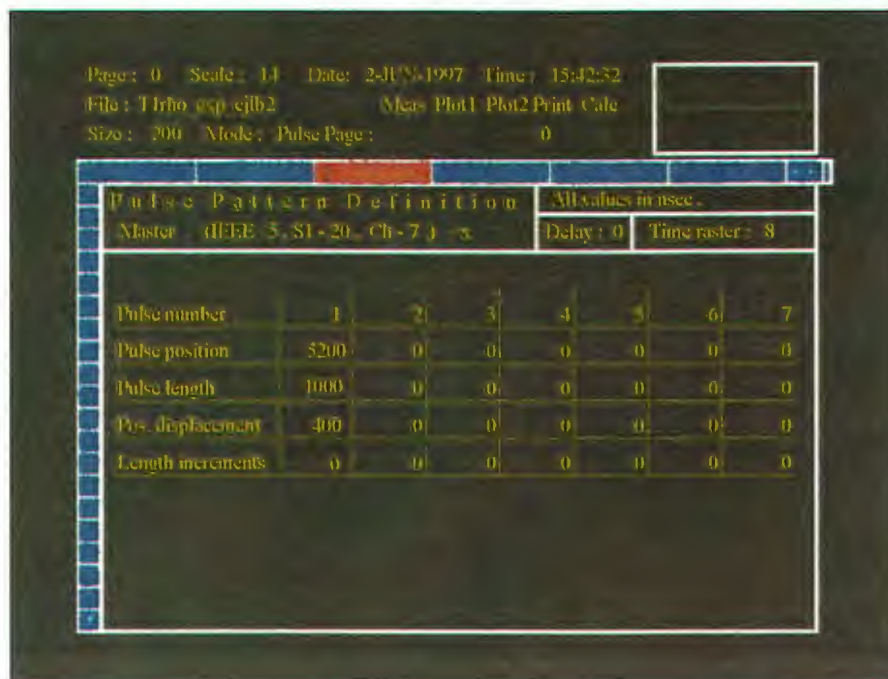
Pulse Pattern Definition								All values in nsec.	
Master (IEEE 5, S1-20, Ch-7) -x								Delay: 2	Time raster: 8
Pulse number	1	2	3	4	5	6	7		
Pulse position	288	2784	0	0	0	0	0		
Pulse length	1000	1000	0	0	0	0	0		
Pos. displacement	0	200	0	0	0	0	0		
Length increments	0	0	0	0	0	0	0		

Figure 3.8b. Spin-lattice relaxation time in the rotating frame :+<x> pulses programmed in the Bruker GUI tables.

Page: 0 Scale: 14 Date: 2-JUN-1997 Time: 15:42:32
 File: T1rho_exp_ejtb2 Meas Plot1 Plot2 Print Calc
 Size: 200 Mode: Pulse Page: 0

Pulse Pattern Definition								All values in nsec.	
Master (IEEE 5, S1-20, Ch-7) -x								Delay: 0	Time raster: 8
Pulse number	1	2	3	4	5	6	7		
Pulse position	1296	0	0	0	0	0	0		
Pulse length	1000	0	0	0	0	0	0		
Pos. displacement	0	0	0	0	0	0	0		
Length increments	200	0	0	0	0	0	0		

Figure 3.8c. Spin-lattice relaxation time in the rotating frame: SDI pulses programmed in the Bruker GUI tables.



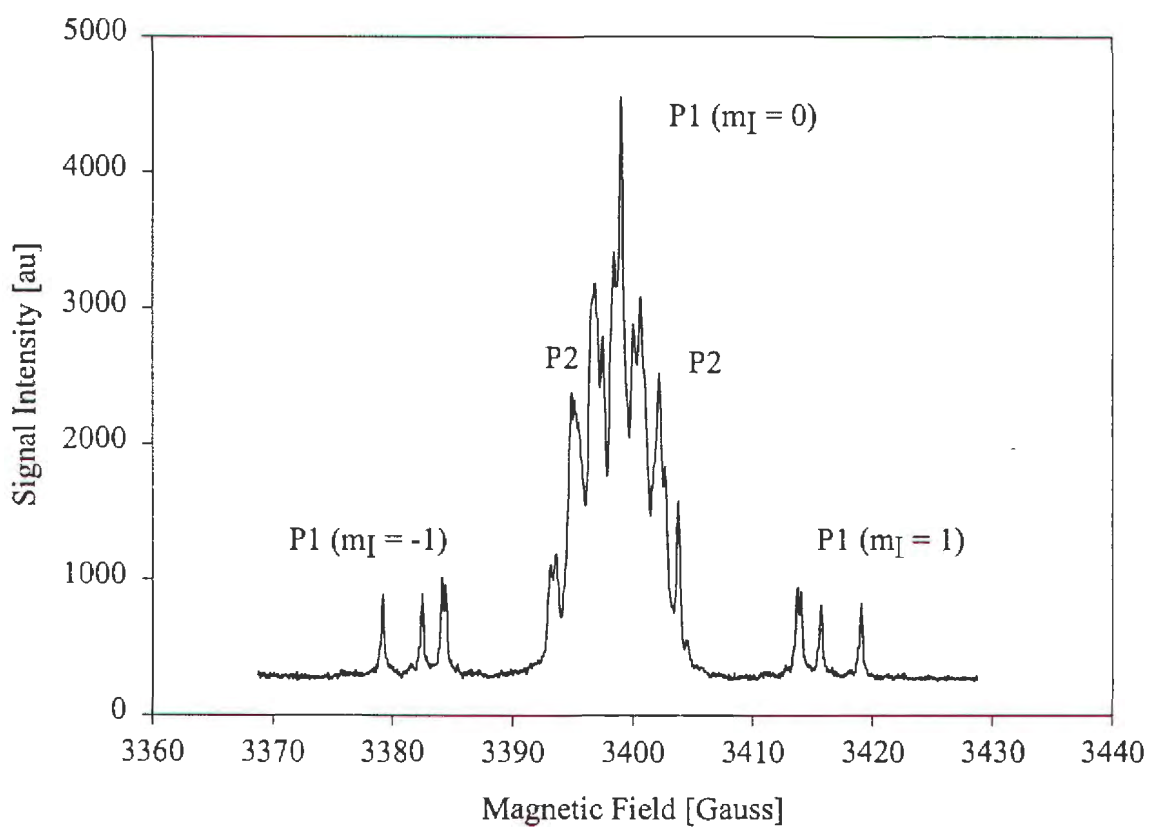
3.5 Continuous Wave Dynamic Nuclear Polarisation at X-Band

Solid state experiments at x-band were also carried out using the Bruker ESP300E EPR spectrometer. Experiments could be performed with a high degree of precision and repeatability and could be carried out on both the central and hyperfine spectral lines. These experiments consisted of the following steps:

1. Obtain the EPR spectrum. An example of a typical EPR spectrum for a type Ia diamond is shown in figure 3.9.
2. Determine the resonance field, i.e. the centre of the particular line to be used in the solid state experiment.
3. Adjust the static field to the resonance field plus or minus 1.3 G
4. Set the modulation amplitude to 1.0 G and the modulation frequency to 100 kHz (for maximum effect).

5. Apply the microwave power under these conditions for the desired experimental time. The maximum power incident into the cavity was 220 mW.
6. Transfer the sample in a field of approximately 3500 G to the NMR spectrometer and measure the ^{13}C magnetisation.

Figure 3.9. Typical EPR spectrum of a type Ia diamond.



In the discussion of the theory of the solid state and thermal mixing effects (chapter 7), it is stated that at x-band, the field offset from resonance, H_F , for the maximum solid effect, occurs when $H_0 \gamma_n / \gamma_e = 1.3$ G. When the EPR line width, H_L is of the order of the field offset from resonance, H_F , the thermal mixing and unresolved solid effects are possible. The relative importance of the solid state, unresolved solid state, and the thermal mixing effects depends on the line width of each particular sample.

Since samples with high P2 centre concentrations have broad lines, the central P1 line is difficult to identify and it was assumed that it occurs at the centre of mass of the hyperfine lines. This situation can be seen in figure 3.9

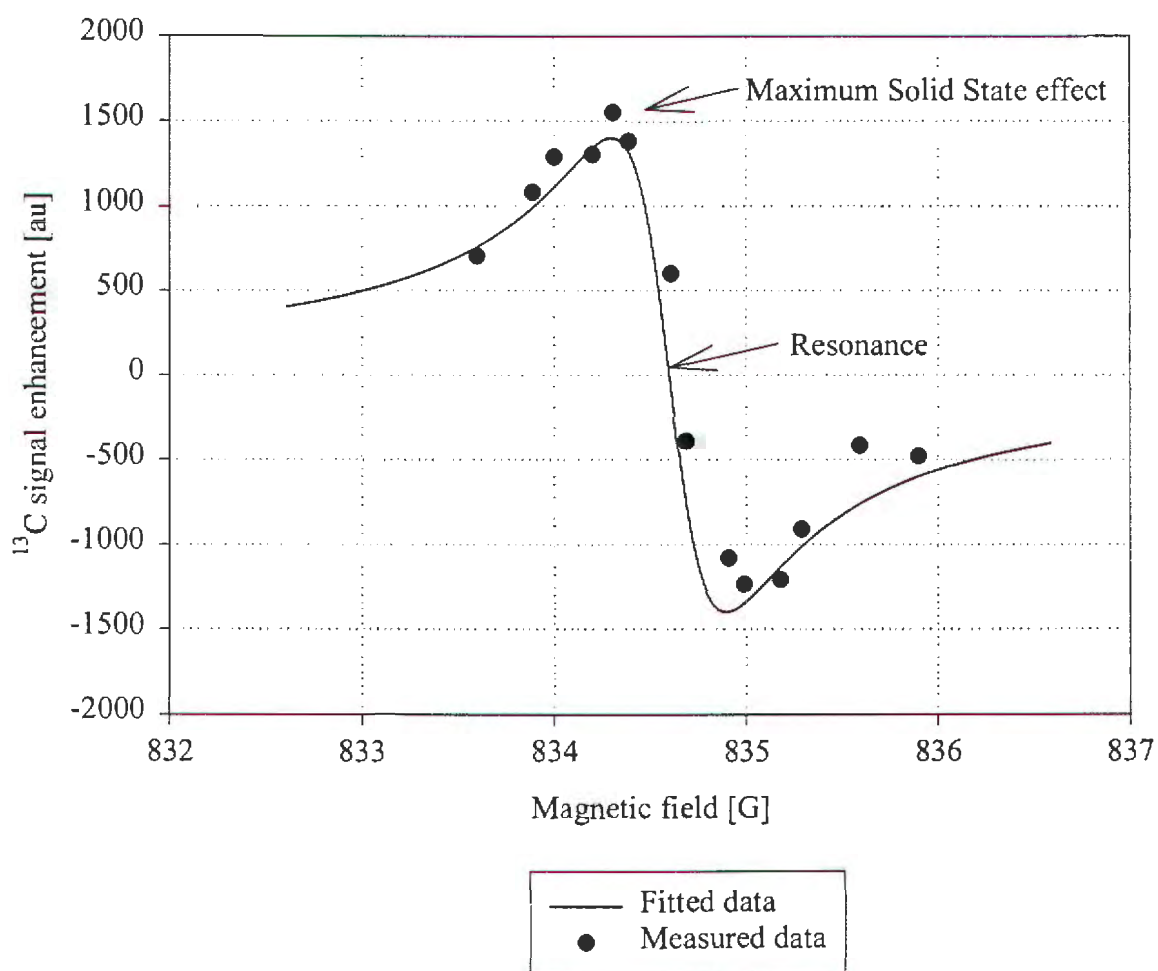
3.6 Continuous Wave Dynamic Nuclear Polarisation at S-Band

Performing solid state experiments at s-band is in principle the same as at x-band but at s-band there is an additional complication. In the description of the s-band DNP system it was mentioned that EPR measurements could not be performed using this system. The result of this situation is that there is no feedback mechanism to determine the exact position of the electron spin resonance and it hence had to be calculated and then optimised. This optimisation process involved performing the solid state experiment over a range of fields in the vicinity of the calculated resonance field and determining the field where the polarisation inverts or where the effect is zero. This point coincides with the position of the resonance. The DNP experiments were then performed in much the same way as in the x-band case. At s-band, the maximum solid state effect occurs when $H_F = 0.3$ G. Figure 3.10 shows the results of a typical optimisation process. The positions of the resonance and maximum solid state effect are indicated.

An advantage of the s-band system over the x-band system is that the input power is much higher. The maximum input power of the x-band system is 220 mW, whereas the power available in the s-band system is up to 1 kW. The effect of incident power on the DNP processes could be investigated thoroughly in this system.

At this frequency (2.4 GHz or 850 G) $H_F \approx 0.3$ G and typical P1 line widths at x-band are of the order of $H_L \leq 0.5$ G (see figure 3.15) and therefore the condition $H_F \approx H_L$ is quite easy to meet. Due to the fact that the EPR line width is dependent on the impurity concentration only, which will obviously not change with field, it is expected that the EPR line width is independent of the magnetic field.

Figure 3.10. Solid state effect as a function of field offset at s-band



Once the field for optimum ^{13}C polarisation had been determined, the exposure of the sample to the microwaves could be varied and DNP time constants determined. This was accomplished by fitting the following equation:

$$M(\tau) = M_0 \left[1 - \exp\left(-\frac{\tau}{T_1^+}\right) \right], \quad 3.7$$

to the experimental data. Here $M(\tau)$ and M_0 are the ^{13}C polarisation after a DNP time τ and at equilibrium, respectively. T_1^+ is the relaxation time under DNP conditions. These methods were used to perform experiments to determine the effects of microwave power and impurity concentration on the DNP process. The results of these experiments are described in chapter 7.

3.7 NOVEL at X-Band

This method of facilitating a transfer of polarisation from the electron spin system to the nuclear spin system involves bringing the electrons into a spin-locked state and satisfying the Hartmann-Hahn condition:

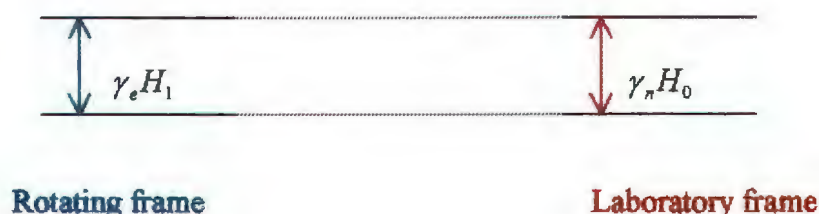
$$\gamma_e H_1 = \gamma_n H_0. \quad 3.8$$

The spin-locked state is achieved by applying a $(\pi/2)_x$ pulse, followed immediately by a locking pulse that is phase shifted by $\pi/2$.

For the Hartmann-Hahn condition to be satisfied the frequency of the pulses are tuned to the electron paramagnetic resonance frequency ω_e . The optimum length of the locking pulse is determined by the electron relaxation rate in the rotating field, $T_{1\rho}$, and thus limits the duration of the spin-locked state. This implies that the electron spin system must be allowed to relax to its laboratory frame equilibrium state, before the NOVEL

sequence can be repeated. This is shown as the recovery time in figure 3.12 and was found by experiment that $5T_{1e}$'s was the optimum recovery time. During the application of the locking pulse the electron magnetisation precesses around the rotating field H_1 at a frequency ω_R . If H_1 is chosen so that $\omega_R = \omega_n$ the NOVEL effect is activated. The energy level diagram for this situation is shown in figure 3.11:

Figure 3.11. Energy level diagram for the satisfaction of the Hartmann-Hahn condition.



The dipolar interaction between the two spin species allows for the transfer of electron polarisation to the nuclei via energy conserving electron-nuclei flip-flop transitions. In terms of heat reservoirs, the cold electron spin reservoir is brought into contact with the warmer nuclear spin reservoir and polarisation is thereby transferred.

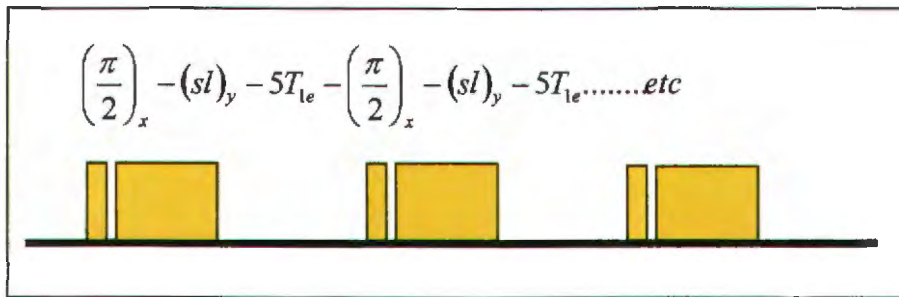
The x-band NOVEL experiments were performed on the Bruker ESP380E spectrometer and involved the following steps:

1. Acquire the EPR spectrum and set the static field to the central transition of the P1 centres.
2. Perform a nutation experiment and determine the power level for a $\pi/2$ pulse as described in section 3.1.
3. Apply the NOVEL pulse sequence shown in figure 3.12, with the $(\pi/2)_x$ pulse determine in the last step and the magnetic field component of the spin-locking pulse $(sl)_y$, set to satisfy the Hartmann-Hahn condition i.e. :

$$H_1 = \frac{\gamma_n}{\gamma_e} H_0. \quad 3.9$$

Inserting a typical value of 3500 G for H_0 gives $(H_1)_{LOCK} = 1.3$ G.

Figure 3.12. NOVEL pulse sequence



4. The amplitude of the spin-locking pulse is determined from:

$$A_{LOCK} = \frac{(H)_{LOCK}}{(H_1)_{\pi/2}} A_{\pi/2}. \quad 3.10$$

The magnitude of $A_{\pi/2}$ is measured on a fast digital oscilloscope.

The pulse programs for the +x and +<x> channels are shown in figures 3.13a and b.

Figure 3.13a. NOVEL +x channel pulse programmed in the Bruker GUI tables.

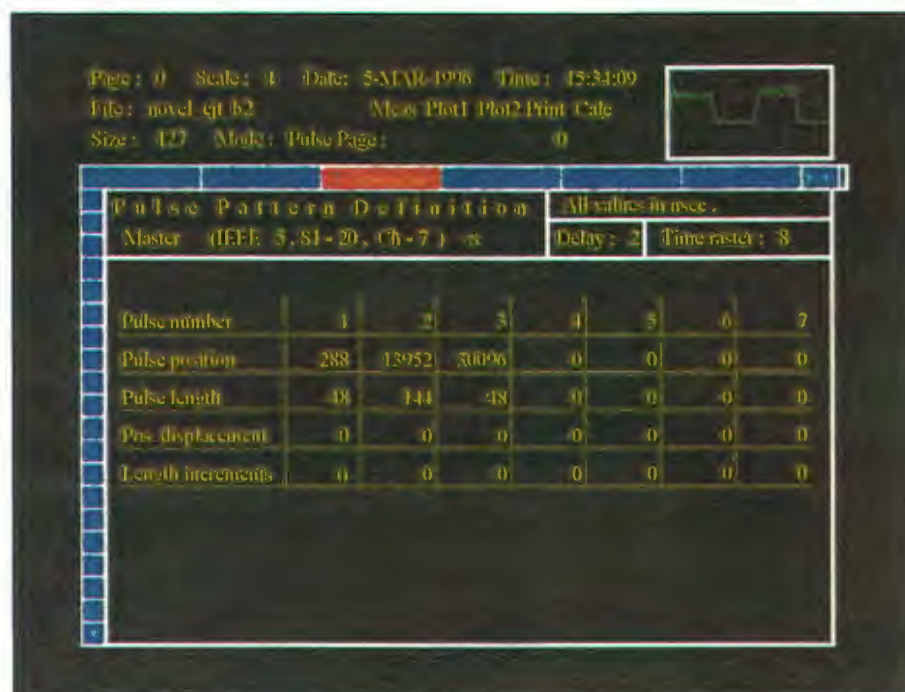
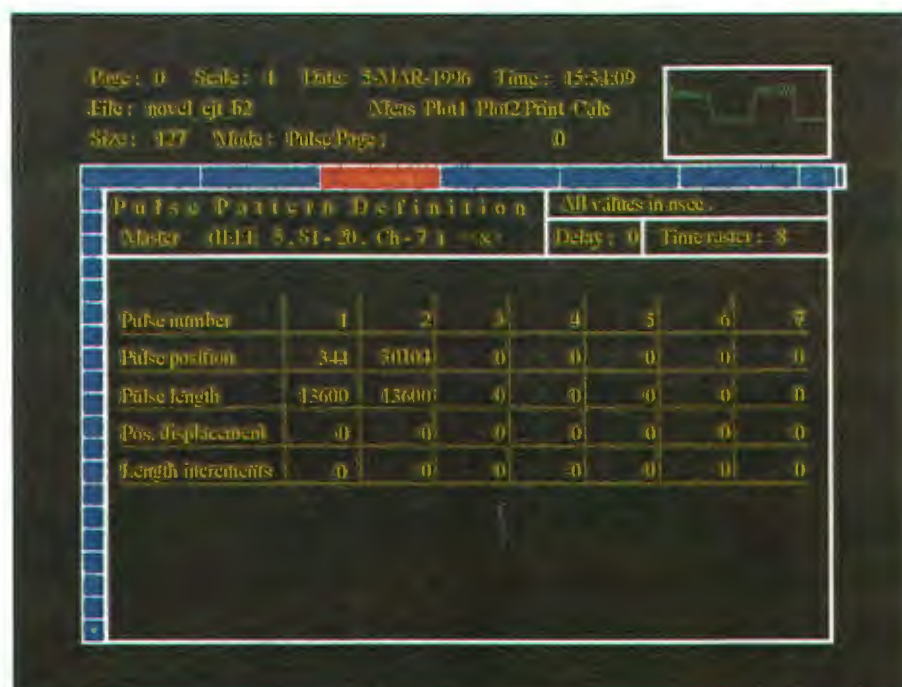


Figure 3.13b. NOVEL +<x> channel pulse programmed in the Bruker GUI tables.



The NOVEL effect was then optimised by measuring the polarisation as a function of the spin-locking pulse length, the phase difference between the $(\pi/2)_x$ and the spin-locking pulse, the amplitude of the spin locking pulse and the recovery time.

The NOVEL polarisation rate was measured by applying the NOVEL pulse sequence for various times, τ , and fitting the equation:

$$M = M_0 \left(1 - \exp \left(- \frac{\tau}{T_{1NOVEL}^+} \right) \right), \quad 3.11$$

to the data. These results are reported in chapter 8.

3.8 NOVEL at S-Band

In the case of the s-band system, pulsed EPR spectroscopy is also not possible for all of the reasons applicable to the continuous wave case, but with the additional problem of long dead times after a microwave pulse at this frequency.

The position of exact resonance was found by determining the field where the continuous wave DNP enhancement inverts from positive to negative or is zero. The NOVEL pulse sequence was then applied at this “resonance” field and the microwave power increased in small steps until the Hartmann-Hahn condition was satisfied. A limitation of the s-band system hardware is that the first pulse and the spin-locking pulse are of the same amplitude. At 850 G, a H_1 field of 0.32 G is required to satisfy the Hartmann-Hahn condition. Solving equation 3.2 for this field gives a $\pi/2$ pulse of 288 ns. This pulse length is very close to the 266 ns measured experimentally. Satisfying the Hartmann-Hahn condition in this system is a rather problematic measurement as small variations in the cavity tuning and matching due to thermal expansion have noticeable effects on the

H_1 field. A second difficulty was the tuning of the cavity to a suitable mode in which the H_1 field is perpendicular to the H_0 field and is a maximum at the position of the sample. Although the cavity tuning was performed with the aid of a Hewlett-Packard Vector Network Analyser (HP8510B) it was difficult to identify the correct or most suitable mode and a trial and error approach had to be adopted. This included electrically loading the cavity and observing the behaviour of the resonant frequency. Migration to higher frequencies on loading indicates the presence of a mode of which the magnetic field component is co-linear with the axis of a cylindrical cavity. The data acquired under these trying circumstances are however quite reasonable and some valuable information was obtained. The exact $\pi/2$ pulse length and H_1 field strength were determined in the nutation experiment shown in figure 3.2. The details of the nutation experiment are given in section 3.1. These results will be discussed in chapter 8.

3.9 Nuclear Polarisation Enhancement

With a view to estimating the ^{13}C signal enhancement, the experimentally measured signal, M_0 , is compared to the Zeeman polarisation, M_{0Z} , at the DNP field to determine the signal enhancement from:

$$\eta_{\text{exp}} = \frac{M_0}{M_{0Z}}. \quad 3.12$$

The ^{13}C Zeeman signals at the DNP fields (3500 G and 850 G) were not detectable on the Bruker Avance 200 MHz NMR spectrometer, even when the samples were left in the DNP fields for many hours. An estimate of the signal strength was however calculated by measuring the Zeeman polarisation at 4.7 Tesla and multiplying this signal intensity by the ratio of the static field strengths i.e. $H_{0\text{DNP}}/H_{0\text{NMR}}$. This is plausible as it follows from the Boltzman distribution that the signal strength is approximately proportional to the static field.

3.10 The Dipolar Reservoir

In the investigation of the various DNP techniques, the polarisation processes were performed in one system and the NMR measurements in another. During transfer between the two systems, the magnetisation is preserved in the dipolar reservoir as follows. After polarisation, if the sample is removed from the polarisation field there will be no macroscopic polarisation visible. When the sample is reintroducing into a magnetic field the magnetisation reappears in a time much shorter than T_{1n} , provided that the removal and reintroduction takes place in a time much shorter than T_{1n} . This is therefore an adiabatic reversible process. In this process, the original ordering with respect to the external magnetic field is preserved in another form in the presence of a low field. In each small region within the sample the magnetisation becomes aligned with the local field it experiences. Since the local fields are randomly oriented, there will be no net macroscopic magnetisation of the sample. When the sample is reintroduced into a magnetic field the magnetisation again assumes an orientation parallel to this field and most of the original polarisation is returned. The spin order of the system, when local fields orientate the magnetisation, is known as dipolar order.

The magnitude of the original magnetisation is determined by the DNP process that was applied, but is much higher than the equilibrium magnetisation at the local field, which is determined from the Boltzmann distribution. The magnetisation will therefore decay from the highly polarised state to the new equilibrium conditions. The time constant for this exponential decay is known as the dipolar relaxation time, T_{1D} . This time constant is usually comparable or shorter than T_{1n} .

The effectiveness of this process is therefore dependent on the sample having a relatively long T_{1n} . In diamond, T_{1n} is determined by the paramagnetic impurity concentration indicating that very pure diamonds with exceeding long T_{1n} 's will retain the induced magnetisation for longer periods than for diamonds with high impurity concentration.

This is indeed what was observed in this study. It was also observed that if the sample is kept in a low magnetic field during the transfer between the two systems, the decay of the polarisation is slower than for zero field. This is due to the dipolar relaxation time being proportional to the local field, which can be deduced from equation 3.16:

$$M(t) = (M_0 - M_{loc}) \exp\left(\frac{-t}{T_{1D}}\right), \quad 3.13$$

where M_{loc} is the equilibrium magnetisation at the local field [3.1]. It can also be deduced from this equation that higher local fields will result in longer T_{1D} 's. Hence placing the sample in a weak magnetic field, higher than the local field, will therefore increase the dipolar relaxation time and the magnetisation therefore decays more slowly in this field.

Although the samples were transferred from the DNP stage to the NMR measurement stage in a magnetic field of about 3500 G, some loss of signal intensity occurred. This loss is estimated at about 20% for samples with relatively high impurity concentrations (i.e. $C_e \geq 10$ ppm) and must also be taken into account when determining enhancement factors and interpreting the results.

3.11 Nuclear Magnetic Resonance Measurements

In investigating the dynamic nuclear polarisation of diamond, various experimental conditions were created and the DNP effect determined. A commonality in these experiments is that the relative effectiveness of the DNP process is determined from the ^{13}C nuclear magnetic resonance signal. Measurement of the NMR signal was carried out on the Bruker Avance 200 MHz system described in chapter 2.

3.11.1 Nuclear Magnetic Resonance Pulse Sequences

The NMR measurements simply involved applying a $\pi/2$ pulse, acquiring the free induction decay (FID) signal and processing that signal.

3.11.2 Nuclear Magnetic Resonance Signal Processing

After a Fourier transformation into the frequency domain, the intensity of a NMR signal must be handled carefully if comparisons between measurement must be made. Various factors, such as amplifier gain, probe head tuning etc. can affect the signal and these must be kept constant between measurements. If signals are relatively strong, simply comparing the peak height or signal-to-noise ratio (SNR) calculated by the software will suffice. In the case of small NMR signals, the calculation of the SNR becomes unreliable. It was found that integrating the signal and determining the area relative to the equilibrium ^{13}C Zeeman polarisation gave the most consistent results. This method was used in all experiments.

Another important parameter to keep track of when conducting DNP experiments is the resulting phase of the NMR signal. This was achieved by phasing the ^{13}C Zeeman signal for a maximum positive signal. Subsequent DNP induced ^{13}C signals were then phase by the same angle.

An exponential filter was applied to the time domain NMR signals to remove some of the high frequency noise. In addition a correction to a known baseline was also made.

3.11.3 Probe Head Tuning

To ensure consistent measurements it would be desirable to tune the NMR probe prior to each measurement. Tuning involves exposing the sample to a frequency band and adjusting the resonance frequency and impedance of the detection circuit. Exposing a polarised sample to this tuning frequency band will however destroy the polarisation in the sample. For samples with short relaxation times this is acceptable, but this is not the case for ^{13}C polarisation in diamond, therefore regular tuning cannot be done. This will be one of the sources of scatter in the measured data.

This problem was partially overcome by tuning the probe with an unpolarised sample placed in the sample holder. The sample holder could be inserted into the NMR measurement coil in a repeatable manner. Tuning was then carried out as described above. It is important to place the sample in the NMR measurement coil in the same position for each measurement because the position of the sample has an effect on the resonance of the detection circuit. Different sample positions will hence lead to inconsistent results.

3.12 EPR Measurements

3.12.1 EPR Line Width Measurements

The line widths were measured from peak-to-peak of the first derivative EPR signals. The spectra were measured on a Bruker ESP300E spectrometer as well as on a Varian CW spectrometer. Where possible, the spectrometers were set-up so that the modulation amplitude was no more than 20% of the peak-to-peak line width. Under these circumstances the broadening should not be more than about 10% [3.2]. In the samples where the modulation amplitude resulted in excessive broadening, the true line widths were obtained by using the tables listed by Kiflawi *et al.* [3.3].

3.12.2 Electron Paramagnetic Resonance Spectra

Spectra for the diamonds were recorded on the Bruker EPR spectrometer in both continuous wave and pulsed mode. A continuous wave spectrum for sample B2 is shown in figure 3.14, which clearly shows the central ($m_l = 0$) line and the four hyperfine lines ($m_l = \pm 1$) for P1 centres. Acquisition of this spectrum and similar spectra for the other samples was done at x-band at low power to avoid excessive line broadening. The pulsed mode spectra for the diamonds used in the study of DNP effects are shown in figure 3.15 and the relevant time constants for these diamonds are listed in table 3.2. Similar data for the diamonds used in the development of the techniques for determining the paramagnetic impurity concentrations in diamond are listed in table 3.3. These spectra were obtained by recording the integral of the pulse echo as a function of static field. The

echoes were obtained by applying a $[(\pi/2)_x - \tau - (\pi/2)_y - \tau - \text{echo}]$ pulse sequence. The $(\pi/2)_x$ pulse length was set to 16 ns and the delay time τ to 2 μ s. It can be seen in figure 3.15 that the number of observed hyperfine lines varies from sample to sample depending on their orientation with respect to the applied static field. An explanation of this behaviour is given in chapter 4.

Figure 3.14. Continuous wave EPR spectrum of sample B2.

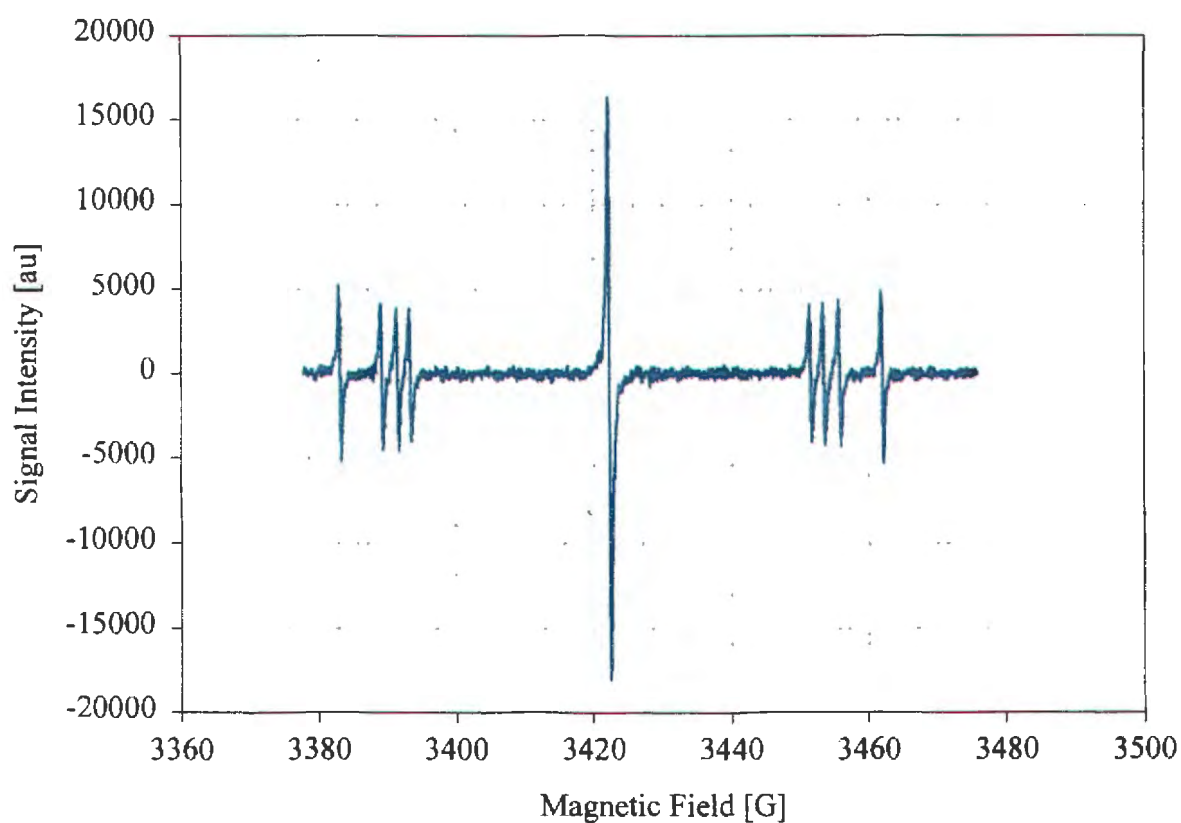
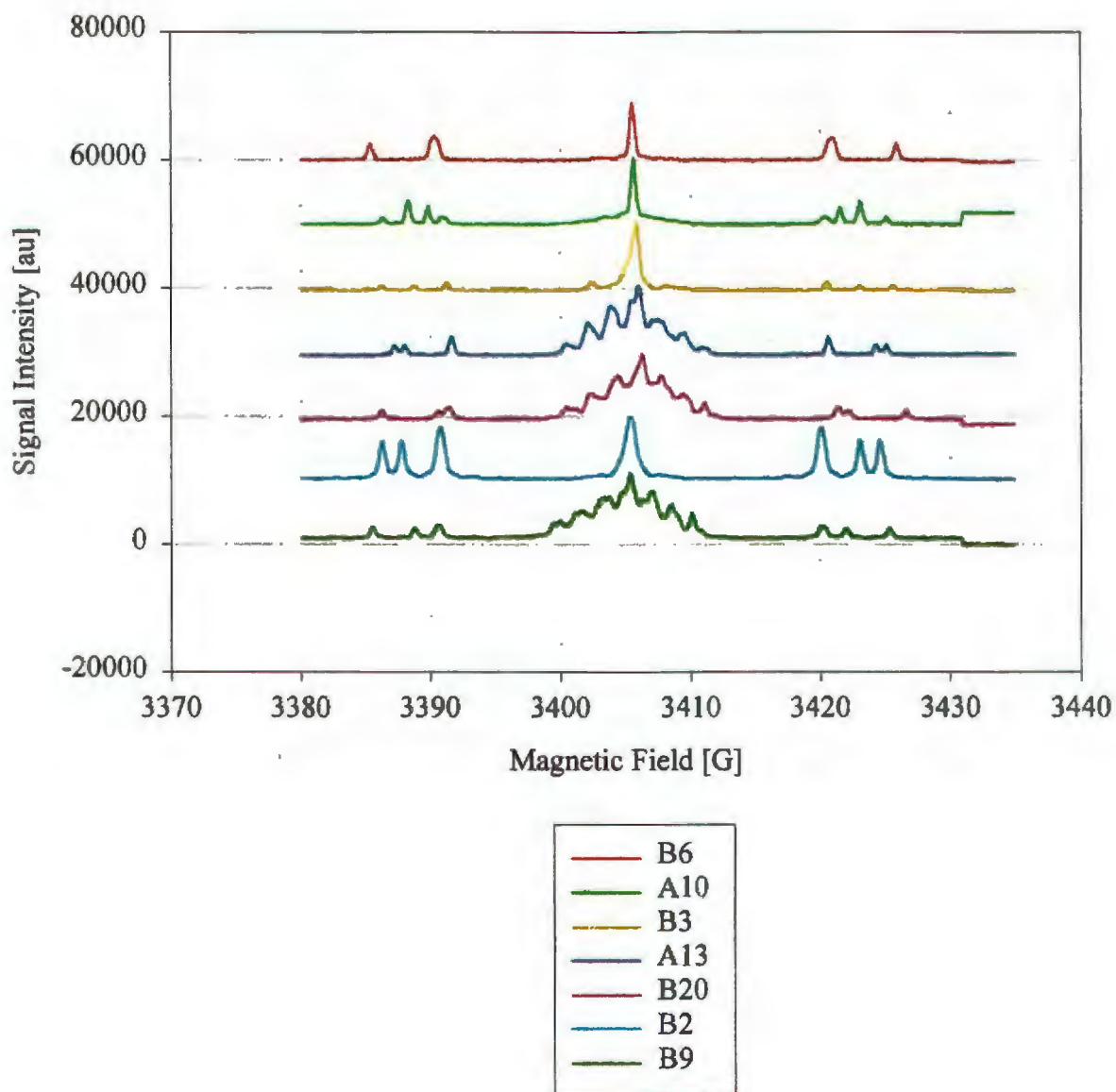


Figure 3.15. Pulse EPR spectra of the samples used in this study.



3.12.3 Electron Relaxation Times

Electron relaxation times were measured in the manner described in section 3.2 and 3.3.

The room temperature relaxation time constants for the diamond used in the study of the

DNP processes are given in Table 3.2. and those used in the determination of the temperature dependence of the relaxation times are given in table 3.3.

Table 3.2. Relaxation time constants of the diamonds used in the DNP study.

Sample Reference	Mass (ct)	Type	Central line		Hyperfine line	
			T _{1c} (ms)	T _{2c} (μs)	T _{1h} (ms)	T _{2h} (μs)
B6	1.554	Ia	2.2 ± 0.1	1.8 ± 0.1	500 ± 30	800 ± 100
A10	2.076	Ia	2.3 ± 0.1	1.6 ± 0.1	120 ± 2	530 ± 20
B3	1.230	Ib	1.5 ± 0.1	1.5 ± 0.1	12.5 ± 0.1	30.2 ± 0.02
A13	1.880	Ia	3.3 ± 0.1	2.5 ± 0.1	47 ± 1	137 ± 6
B20	0.741	Ia	4.3 ± 0.1	1.6 ± 0.1	8.4 ± 0.2	30 ± 2
B2*	1.890	Ib	0.75 ± 0.01	1.4 ± 0.1	3.10 ± 0.03	7.7 ± 0.1
B9	1.250	Ia	4.1 ± 0.2	1.7 ± 0.2	4.5 ± 0.1	16.3 ± 0.2

* Sample B2 includes N3 centres which will influence the relaxation time of the central line.

Table 3.3 Diamond samples used in the investigation of the temperature dependence of the relaxation times.

Sample Reference	Mass (ct)	Type	Central line		Hyperfine line	
			T _{1c} (ms)	T _{2c} (μs)	T _{1h} (ms)	T _{2h} (μs)
NLO3	1.2	Ib	1.49	0.63	2.08	-
NLO2	2.3	Ia	2.06	0.69	1.75	-
D10	3.4	Ia	1.50	1.13	1.43	1.07
E4	4.5	Ib	7.05	3.29	1.48	29.61
B2	5.6	Ia	7.00	2.64	19.04	10.6

These samples were selected by virtue of their impurity concentrations and impurity types ranging from high and low P1 defect centres only (Ib diamonds) and high to low P1+P2 centres combined (Ia and IIa diamonds).

3.13 References

- [3.1] E. Fukushima and S. B. W. Roeder, *Experimental pulsed NMR*, (Addison-Wesley Publishing Company, 1993), p241.
- [3.2] J. H. N. Loubser and J. A. van Wyk, *Rep. Prog. Phys.* **41**, (1978).
- [3.3] I. Kiflawi, A. E. Spear, J. A. van Wyk and G. S. Woods, *Phil. Mag. B*, **69**, 1141, (1994).

Chapter 4

Common Defects in Diamond



4.1 Introduction to Defects in Diamond.....	79
4.2 Description of P1, P2 and N3 centres.....	80
4.2.1 Dispersed Substitutional Nitrogen: The P1 Centre	80
4.2.2 Aggregated Nitrogen. The P2 Centre	83

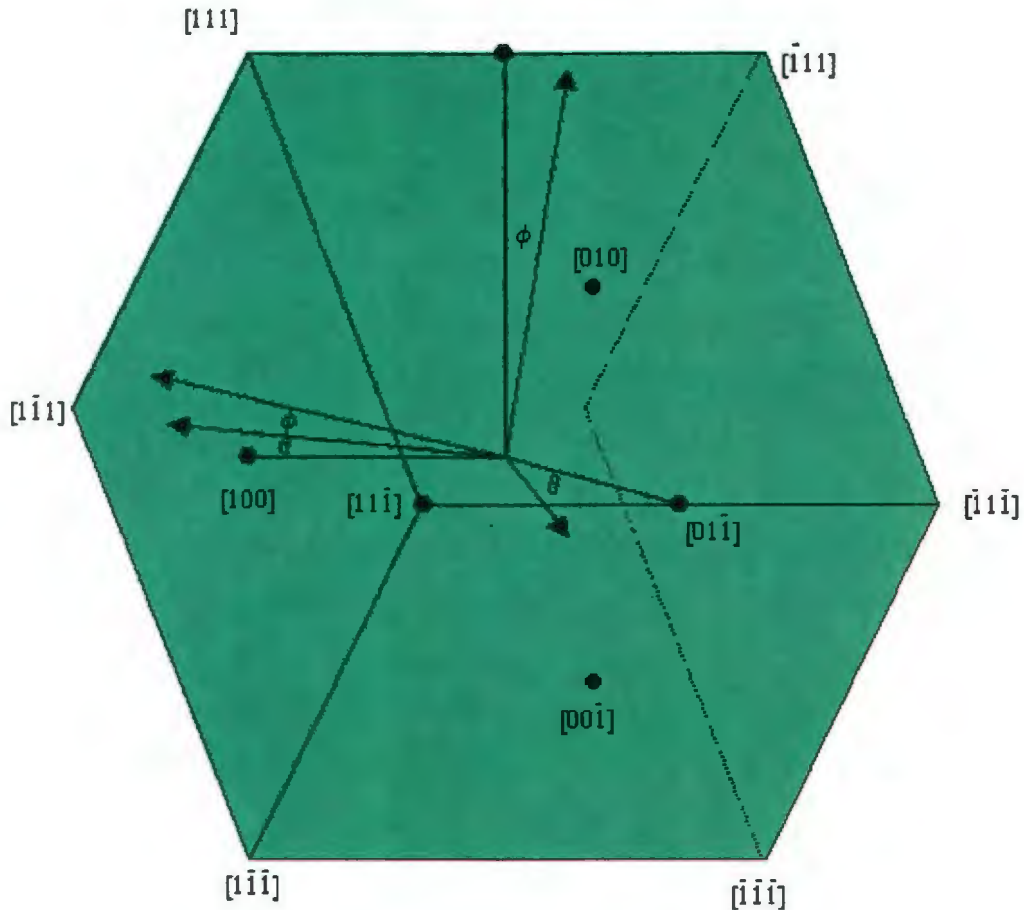
4.2.3 The N3 Centre	84
4.3 Diamond Types	87
4.3.1 Type I.....	87
4.3.2 Type II	88
4.4 Sample Characterisation	88
4.5 References.....	89

4.1 Introduction to Defects in Diamond

Defects are responsible for the colour and clarity of diamond and play an important role in determining their value. Consequently much time and effort has been spent in this area of diamond research although most of it has been concentrated (understandably so) in the optical domain [4.1]. Of more interest to this study are the paramagnetic impurities and their electrical properties. In these studies, natural diamond is most often used without specific knowledge of the nature and concentration of the defects, which has led to a considerable amount of speculation and guess work when interpreting some of the observed behaviour [4.2]. The labelling system for defect centres in diamond is a derivative of the system proposed by Watkins [4.3] for silicon and germanium. All EPR defects will hence be labelled by designating the initial letter of the laboratory where it was discovered followed by a number indicating the order of discovery as near as possible. The practice of Watkins in labelling principal axes is also followed. Here the major axis is labelled 1, whereas the minor axes are labelled 2 and 3. The directions of these principle axes are specified relative to the axes shown in figure 4.1 below.

Many defect centres have been proposed and discussed in the literature but by far the most common paramagnetic impurities are nitrogen impurities in the form of the so-called P1 and P2 centres. In chapter 6 where the temperature dependence of the relaxation rates are investigated, the anomalous behaviour of two of the samples seems to be related to the presence of the N3 centre. These three centres are discussed in some detail in section 4.2.

Figure 4.1. Principal axes and directions used in describing defect centres [4.2].



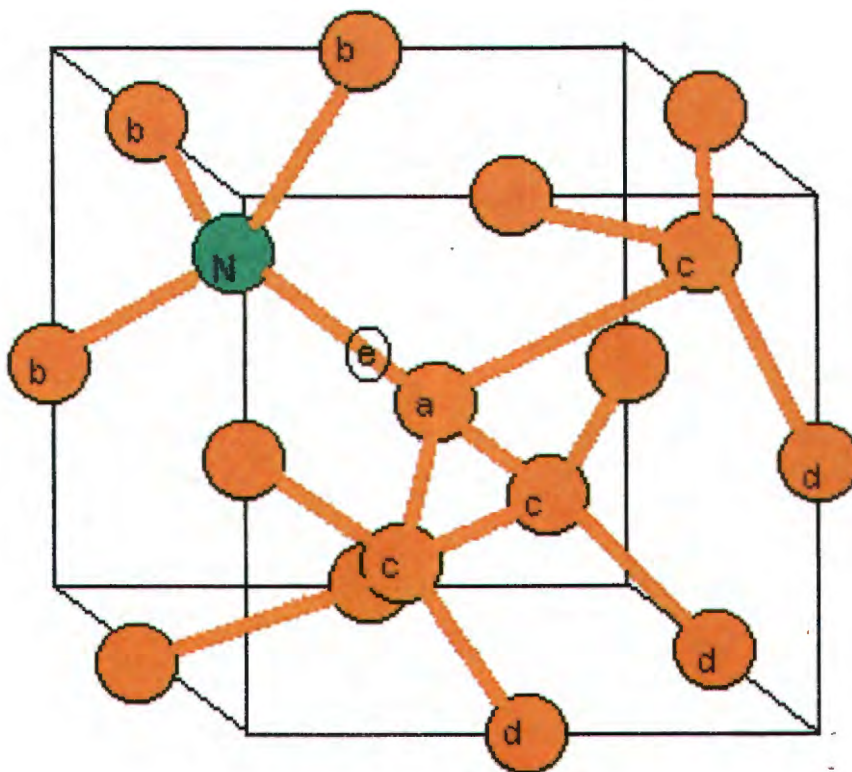
4.2 Description of P1, P2 and N3 centres

4.2.1 Dispersed Substitutional Nitrogen: The P1 Centre

The first defect centre that was observed and assigned using the EPR technique is the P1 centre and is accredited to Smith *et al.* [4.4]. The P1 centre consists of single substitutional nitrogen as shown in figure 4.2. Since nitrogen has five valence electrons it forms covalent bonds with only three neighbouring carbon atoms. The fourth sp^3 hybrid orbital is then occupied by a lone pair, leaving one carbon with an unpaired electron [4.5]. The vector from this carbon nucleus to the nitrogen nucleus, co-insides with one of the four $\langle 111 \rangle$ directions of the tetrahedral molecule. The EPR signal of an isolated P1

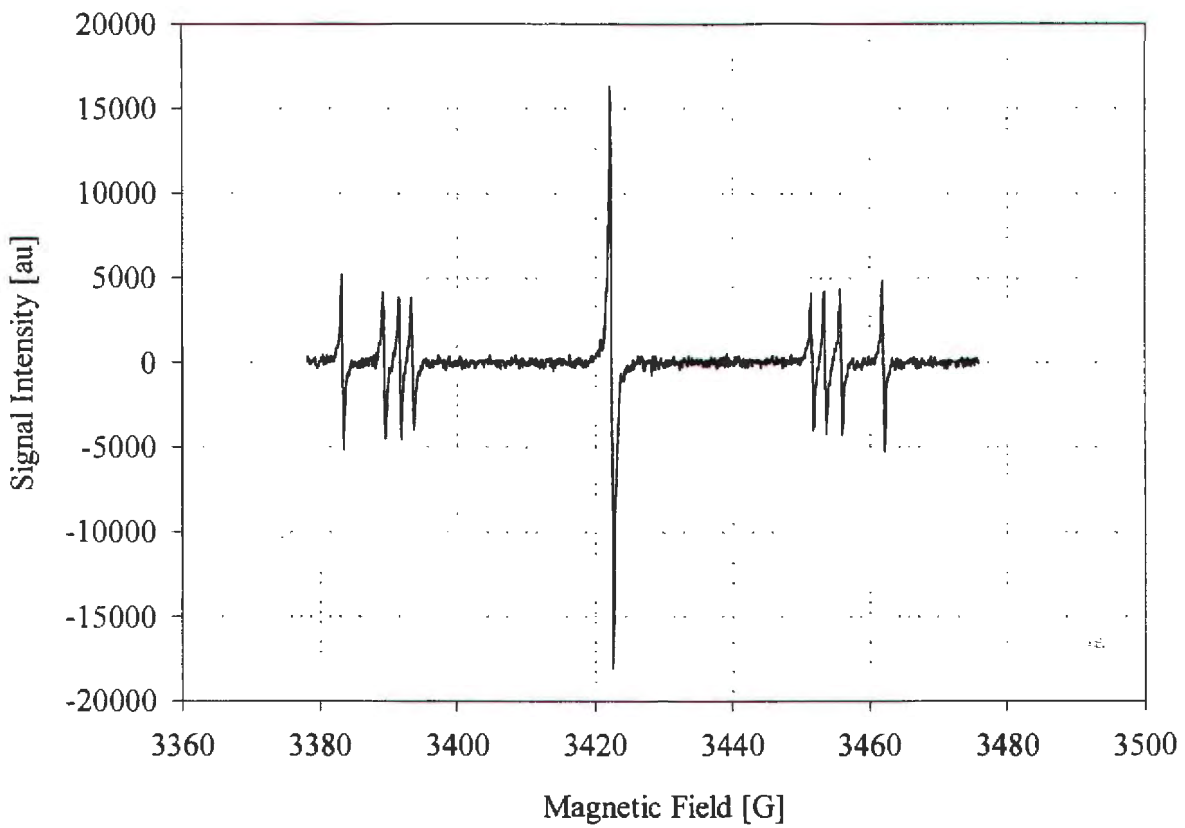
centre consists of the central ($m_l = 0$) line and two hyperfine transitions ($m_l = \pm 1$) on either side of the central line. In the case of a single crystal the N-C bonds are equally distributed along the four $\langle 111 \rangle$ directions resulting in four pairs of hyperfine lines (four on each side of the central line) as can be seen in figure 4.3. If the external field is applied in one of the $\langle 111 \rangle$ directions, three of the N-C bonds will make equal angles with the applied field resulting in these three lines overlapping.

Figure 4.2. Diamond lattice in the vicinity of substitutional nitrogen (after Loubser and van Wyk [4.2])



A typical EPR spectrum of a diamond containing these defects is shown in figure 4.3. Elucidation of this spectrum shows that the paramagnetic electron ($S = 1/2$), interacts with the ^{14}N ($I = 1$) and also with the ^{13}C ($I = 1/2$) nuclei in positions a, b, c and d in figure 4.2.

Figure 4.3 A typical EPR spectrum of a diamond containing P1 defects.



4.2.2 Aggregated Nitrogen. The P2 Centre

The P2 defect centre consists of three nitrogen nuclei and a vacancy in neighbouring positions in the $\{111\}$ plane [4.6]. The proposed model for the P2 centre is shown in figure 4.4. A typical EPR spectrum for a diamond containing both P1 and P2 centres is shown in figure 4.5.

Figure 4.4. Proposed model of a P2 defect centre [4.6]

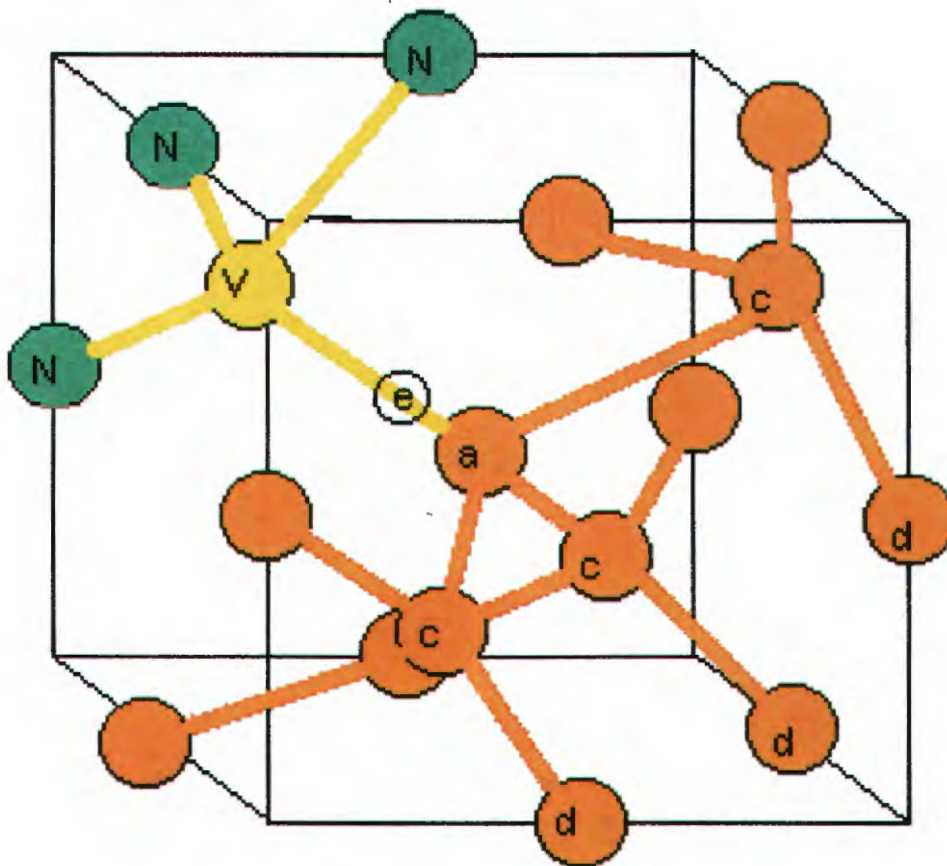
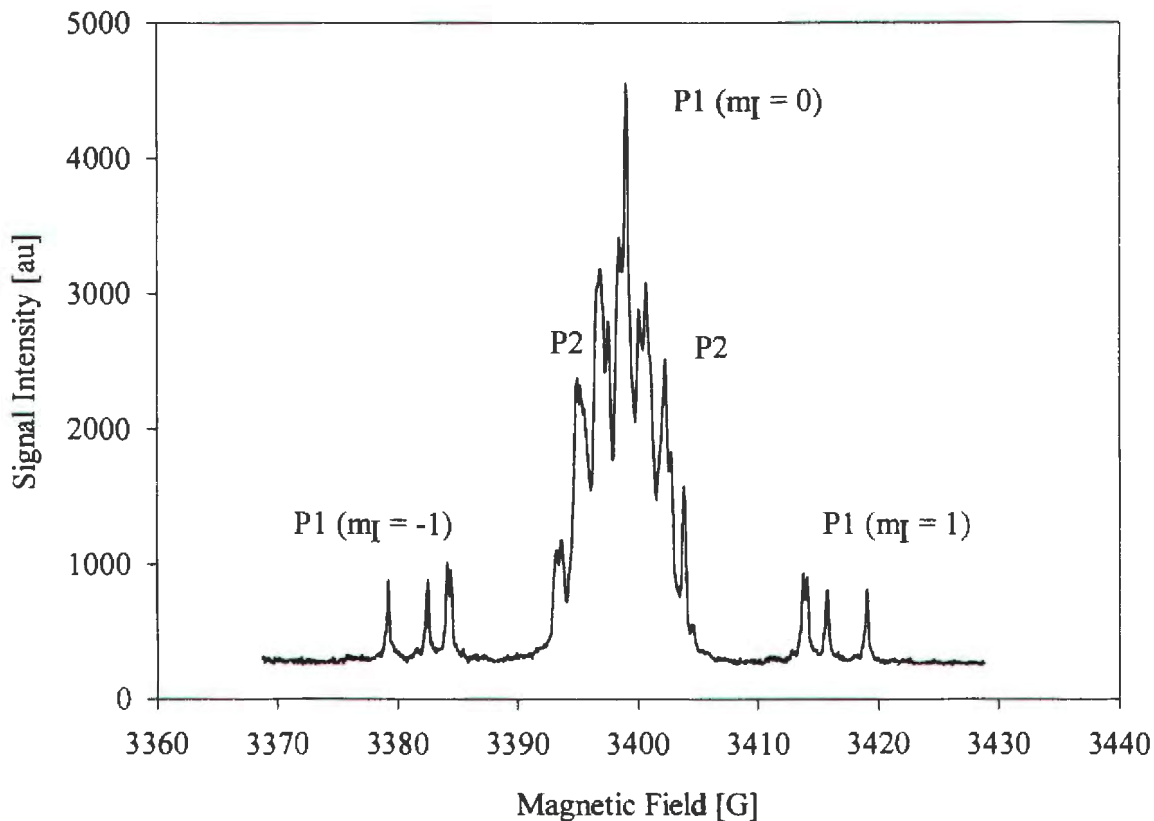


Figure 4.5. Typical EPR spectrum of a type Ia diamond.

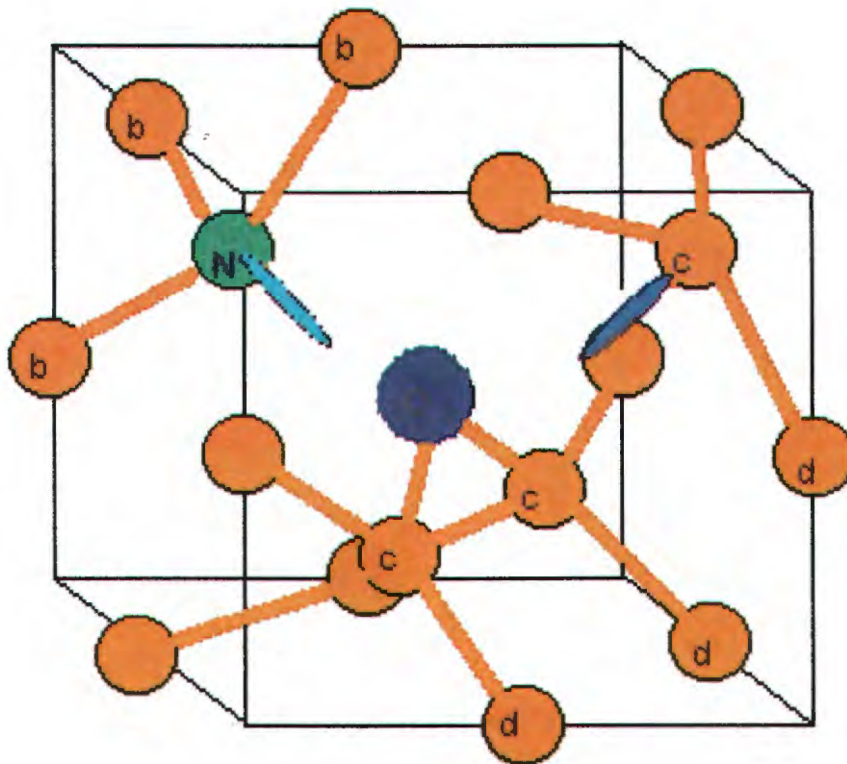


4.2.3 The N3 Centre

This defect centre was first reported by Scherbakova *et al.* [4.7] in 1972. It frequently occurs with P1 [4.8] centres and OK1 [4.9] centres in natural type Ib diamonds. In Scherbakova's model, the N3 centre is proposed to consist of 3 nitrogen nuclei and a vacancy, where the 3 nitrogen nuclei are usually but not always in the form of platelets in cube planes. These planar defects range in size from about 10 nm to a few micrometers

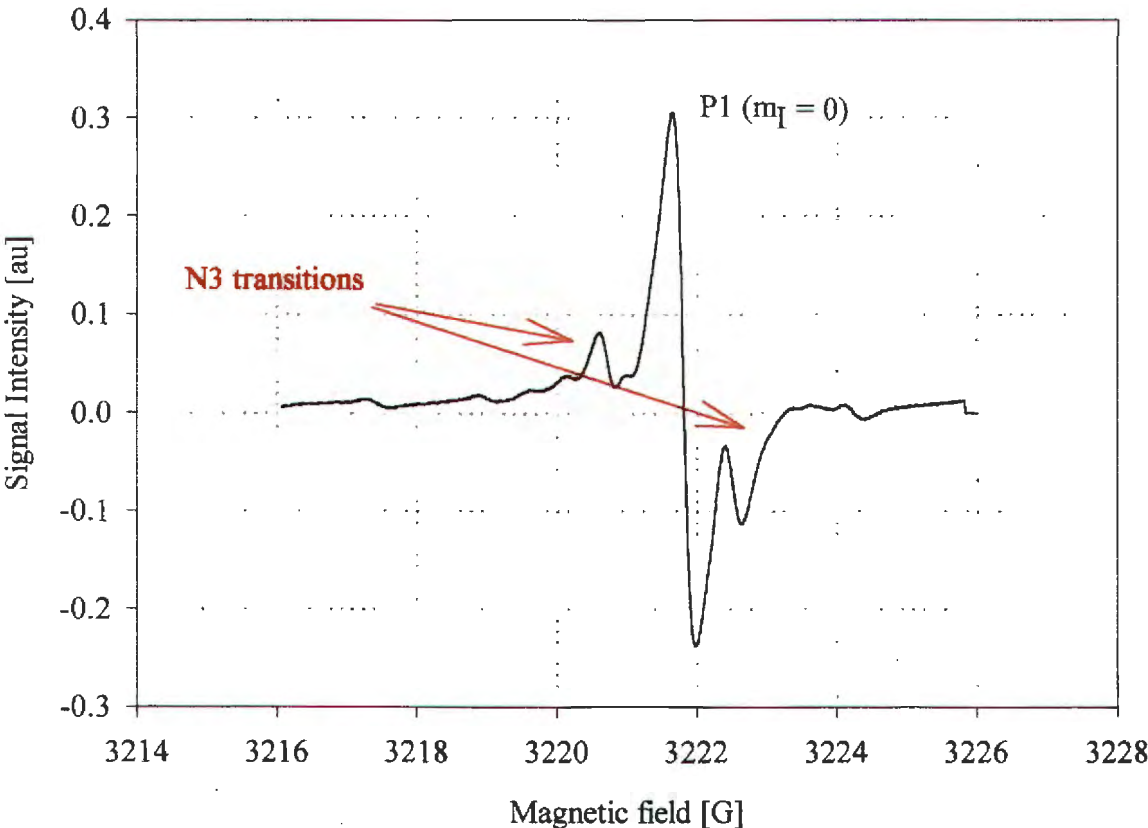
and are found in concentration between 10^{14} and 10^{16} per cm^3 . The model proposed by van Wyk *et al.* [4.10] that replaces the vacancy with oxygen, is shown in figure 4.6.

Figure 4.6. Proposed model for the N3 centre. Full electron orbitals on the oxygen are not shown [4.10]



A typical EPR spectrum of a diamond containing N3 centres is shown in figure 4.7. The N3 centre produces a number of lines that are situated on both sides of the central line. Note that these lines are not symmetrical about the central line.

Figure 4.7 Typical EPR spectrum of diamond containing N3 centres.



4.3 Diamond Types

4.3.1 Type I

Diamonds that contain significant amounts of nitrogen are termed type I diamond. There are a number of sub-classes of type I diamonds, which are discussed below. The sub-classes depend on the type of nitrogen aggregation present.

4.3.1.1 Type Ia

Type Ia diamonds are the most commonly found diamonds. The nitrogen in type Ia diamonds is all in the form of aggregates and are typically found in concentrations ranging from 200 ppm to 5000 ppm [4.11]. Type Ia diamonds can be specified more accurately if the form of aggregation is also specified. The sub-classes of type Ia are given below.

4.3.1.2 Type IaA

In these diamonds, nitrogen exists as A centres that consist of 2 nitrogen nuclei on adjacent lattice sites [4.11]. These defect centres are not paramagnetic so cannot be detected or explored using EPR techniques.

4.3.1.3 Type IaA/B

In this case, nitrogen impurities occur in a combination of A and B centres. B centres consists of 4 nitrogen lattice sites and a vacancy [4.11].

4.3.1.4 Type IaB

In these diamonds, all of the nitrogen impurities are in the form of the B centres described above.

4.3.1.5 Type Ib

In these quite rare diamonds the nitrogen occurs as dispersed substitutional atoms and is usually found in the concentration range from 150 ppm to 600 ppm [4.12]

4.3.2 Type II

Diamonds that fall into this type class are essentially nitrogen free, although all natural diamonds contain some nitrogen. The concentration range in this class is between 4 ppm and 40 ppm [4.12]. Type II diamonds are also divided into the “a” and “b” sub-classes described above.

4.3.2.1 Type IIa

Nitrogen concentrations in these diamonds are very low, but will occur in the forms described for the type I diamond.

4.3.2.2 Type IIb

Type IIb diamonds display semi-conducting properties. The semi-conducting behaviour is due to the presence of substitutional boron acceptor atoms in the lattice [4.1]. These diamonds are extremely rare and are generally only found at specific deposits.

4.4 Sample Characterisation

The samples used in the study of the dynamic nuclear polarisation of diamond were listed in table 3.2 and those used to determine the temperature dependence of the electron relaxation times were listed in table 3.3. These samples were chosen to allow an investigation into the effect of impurity concentration on the DNP processes and the temperature dependence of the electron spin-lattice relaxation rates. The latter was investigated for the central and hyperfine lines. These lines were indicated in a typical EPR spectrum of a Ia diamond shown in figure 4.5.

4.5 References

- [4.1] J. E. Field, *The Properties of Natural and Synthetic Diamond*. (Academic Press, 1992).
- [4.2] J. H. N. Loubser and J. A. van Wyk, *Rep. Prog. Phys.*, **41**, 1978.
- [4.3] G. D. Watkins, *Proc. 7th Conf. on Physics of Semiconductors*, edited by P. Baruch (Paris: Dunod) p97, (1965).
- [4.4] W. V. Smith, P. P. Sorokin, I. L. Gelles and G. J. Lasher, *Phys. Rev Lett*, **2** 39, (1959).
- [4.5] E. C. Reynhardt and G. L. High, *Dynamic Nuclear Polarisation of Diamond. I: Solid state and thermal mixing effects*, Accepted for publication in *J. Chem. Phys.* (1998).
- [4.6] J. A. van Wyk, *J. Phys. C: Solid State Phys.* **15**, 981, (1982).
- [4.7] M. Y. Shcherbakova, E. B. Sobolev and V. A. Nadolinnyi, *Sov. Phys.-Dokl.*, **17**, 513 (1972).
- [4.8] W. V. Smith, P. P. Sorskin, I. L. Gelles and G. J. Lasher, *Phys. Rev.*, **115**, 1546, (1959).
- [4.9] P. E. Klingsporn, M. D. Bell and W. J. Leivo, *J. Appl. Phys.*, **41**, 2977, (1970).
- [4.10] J. A. van Wyk, J. H. N. Loubser, M. E. Newton and J. M. Baker, *J. Phys. Condens. Matter*, **4**, 2651, (1992).
- [4.11] J. F. P. Sellschop, in *The Properties of Diamond*, edited by J. E. Field, (Academic Press, London, 1979), p107.
- [4.12] G. Davis, *J. Phys. C***9**, L537, (1976).

Chapter 5

Determination of the Paramagnetic Impurity Concentration in Diamond from the EPR Line Width and the Spin-spin Relaxation Time.



5.1 Introduction.....	93
5.2 Background theory	93
5.2.1 Impurity Concentration Determined from the EPR Line Width.....	93

5.2.2 Impurity Concentration Determined from the Spin-Spin Relaxation Time.....	96
5.3 Results.....	97
5.3.1 Synthetic Diamond Samples	97
5.3.2 Natural Diamond Samples	97
5.3.3 Impurity Concentration as a Function of Line Width.....	97
5.3.4 Impurity Concentration as a Function of Spin-Spin Relaxation Time.....	99
5.4 Discussion	101
5.5 References	102

5.1 Introduction

The behaviour of the relaxation times and the dynamic nuclear polarisation of natural diamonds, as a function of impurity concentration, is investigated in Chapters 6, 7 and 8. Knowledge of the paramagnetic impurity concentration in natural diamond samples is a prerequisite for proper investigations of the various aspects reported in these chapters. A reliable method of measuring the impurity concentration of diamonds with a view to selecting the most appropriate samples was therefore sought. The methods developed are reported in this chapter.

5.2 Background theory

Kittel and Abrahams [5.1] showed that for a highly dilute spin system, the width of the resonance line should be proportional to the impurity concentration if only magnetic dipolar interactions are considered. It is also known that the spin-spin relaxation time, T_{2e} , is dependent on the impurity concentration. The availability of pulsed EPR spectrometers has made the measurement of T_{2e} relatively straightforward. Hence, knowledge of the dependencies of the EPR line width and the spin-spin relaxation time on the paramagnetic impurity concentration should allow the determination or estimation of the paramagnetic impurity concentration.

5.2.1 Impurity Concentration Determined from the EPR Line Width.

The EPR line width is due to homogeneous and inhomogeneous broadening. Homogeneous broadening is mainly due to dipolar interactions between spins of the same frequency. Inhomogeneous broadening is due to interactions between spins of different frequencies, hyperfine interactions and inhomogeneities in the applied field.

For a dilute spin system, the distance between paramagnetic centres is [5.2]:

$$r_{e-e} = 0.55N_e^{-\frac{1}{3}}, \quad 5.1$$

where N_e is the number of paramagnetic impurities per cubic centimetre. In the case of diamond, with a FCC crystal structure ($a = 3.57 \text{ \AA}$, $Z = 4$), equation 5.1 becomes:

$$r_{e-e} \approx 1.24 \times 10^{-6} C_e, \quad 5.2$$

where C_e is the impurity concentration in ppm.

The distance between paramagnetic impurity centres is related to the line width via the second moment of the EPR line [5.3]:

$$M_2 = \frac{9}{20} (g\beta)^2 r_{e-e}^{-6} + \frac{1}{5} f \gamma_n \hbar^2 \sum_k r_k^{-6}, \quad 5.3$$

where f is the natural abundance of ^{13}C nuclei (1.1%) and the summation is over the all the ^{13}C nuclei surrounding a paramagnetic centre. Substituting equation 5.2 into equation 5.3 and performing the summation yields:

$$M_2 = 4.55 \times 10^{-3} C_e^2 + 0.0055 \text{ [G}^2\text{]}. \quad 5.4$$

If it is assumed that the line shape function of an EPR line can be describe by a gaussian function:

$$g(H) = \frac{1}{\Delta\sqrt{2\pi}} \exp\left[-\frac{(H - H_0)^2}{\Delta^2}\right], \quad 5.5$$

where Δ is the gaussian width. The second moment is then given by:

$$M_2 = \frac{\Delta^2}{2}. \quad 5.6$$

The peak-to-peak width, as indicated in figure 5.1, is given by [5.3]:

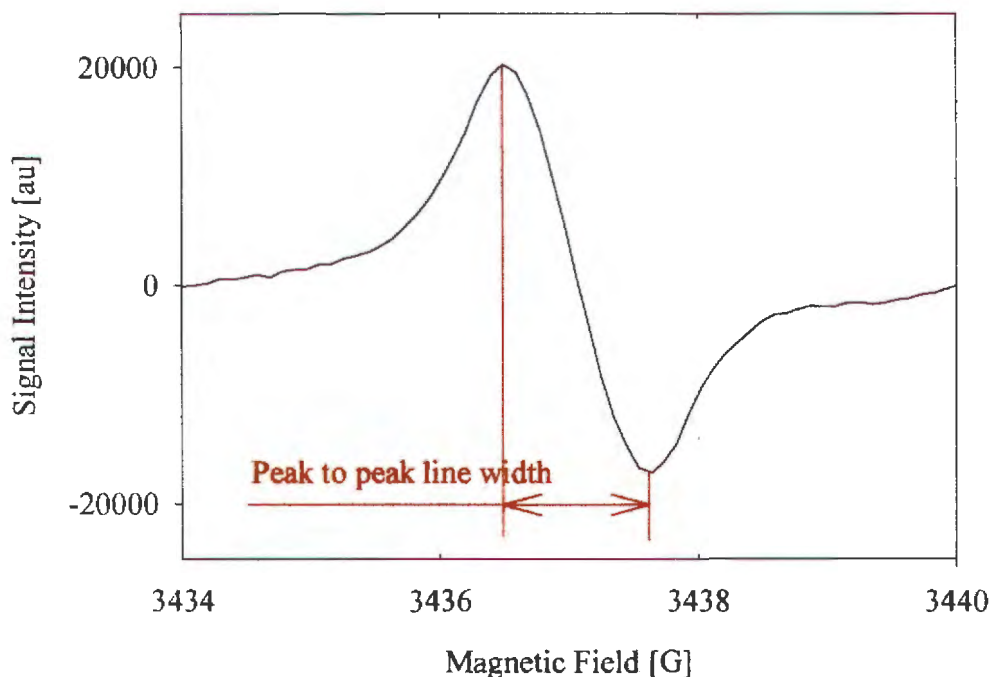
$$\delta = \frac{2}{\sqrt{\pi}} \Delta = \sqrt{1.2 \times 10^{-4} C_e^2 + 0.014} \text{ [G].} \quad 5.7$$

or

$$C_e = 8.33 \times 10^3 \delta^2 - 1.17 \times 10^2 \text{ ppm.} \quad 5.8$$

The impurity concentration can be determined by substituting the experimentally determined line width into this equation.

Figure 5.1. Central transition of the EPR spectrum of a Ib diamond with peak-to-peak line width indicated.



5.2.2 Impurity Concentration Determined from the Spin-Spin Relaxation Time.

The determination of the spin-spin relaxation time employs a pulse echo measurement technique that refocuses or rephases magnetisation that has been dephased due to inhomogeneous broadening. The resulting time constant, T_{2e} , measured from the echo decay, is only dependent on homogeneous broadening sources such as paramagnetic impurities [5.4]. Broadening sources such as field homogeneities and interactions between spins of different Larmor frequencies will not influence the measured T_{2e} value. The value of T_{2e} is dependent on the line or position in the spectrum that is measured. This dependency is accounted for as follows:

1. Hyperfine line: only P1 centres contribute to this measurement, because there is no overlap between these lines and the P2 lines.
2. Central line: at this position overlap between P1 and P2 lines does occur for Ia diamonds and the measurement contains contributions from both centres.

The spin-spin relaxation rate of the central line is then given by [5.3]:

$$\frac{1}{T_{2e}} = \frac{1}{T_{2(P1 \leftrightarrow P1)}} + \frac{1}{T_{2(P1 \leftrightarrow P2)}}, \quad 5.9$$

Where $(P1 \leftrightarrow P1)$ indicates the spin-spin relaxation time for P1 centres only and $(P1 \leftrightarrow P2)$ for P1 and P2 centres together. For the hyperfine lines ($m_l = \pm 1$), only the first term on the right hand side of equation 5.9, contributes, but for the central line ($m_l = 0$), both terms contribute.

For a gaussian line [5.3]:

$$\frac{1}{T_{2e}} = \frac{\gamma_e}{2\pi} \sqrt{\frac{M_2}{2}}, \quad 5.10$$

where M_2 is in G^2 and T_{2e} in seconds.

Substituting equation 5.4 into equation 5.10 and simplifying yields:

$$\frac{1}{T_{2e}} = 1.4 \times 10^4 (C_{eP1} + C_{eP2}) s^{-1}, \quad 5.11$$

where C_{eP1} is the concentration of P1 centres and C_{eP2} is the concentration of P2 centres.

5.3 Results

5.3.1 Synthetic Diamond Samples

A homogeneous distribution of P1 centres within the samples, as well as a range of impurity concentrations was a requirement for these measurements. For this purpose a suite of synthetic diamonds was prepared by cutting samples from single growth centres in larger crystals, which were grown by the reconstitution method [5.5]. Each sample was approximately 0.02 cts. The paramagnetic impurity concentrations were determined by comparing the doubly integrated first derivative signals of these signals with those of freshly powdered $CuSO_4 \cdot 5H_2O$. The concentration of the copper sulphate sample was assumed to be 2.41×10^{21} spins per gram. For low concentration type Ia samples, the concentration was estimated by comparing the spectra, normalised with respect to the same microwave power, spectrometer gain, modulation amplitude, sample mass and cavity Q factor. The range of impurities for the synthetic diamond was from 3 to 400 ppm.

5.3.2 Natural Diamond Samples

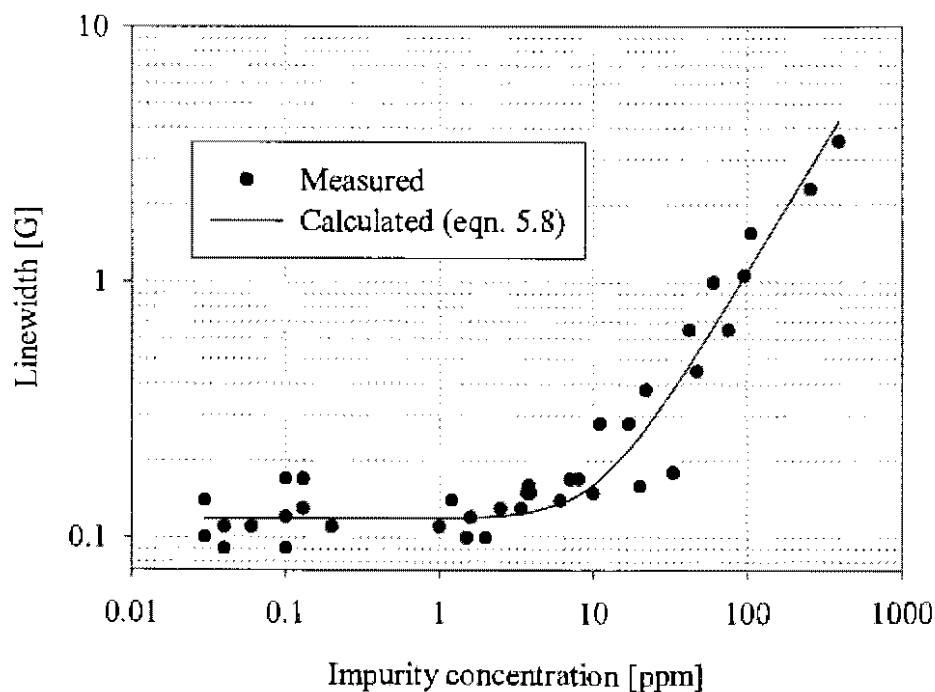
A suite of natural Ia diamonds with impurity concentrations, including both P1 and P2 centres, of between 0.03 and 8 ppm was identified.

5.3.3 Impurity Concentration as a Function of Line Width

The data obtained in these measurements and the calculated values (solid line) are given in figure 5.2. The calculated values are in good agreement with the measured values. At

impurity concentrations above about 10 ppm the first term in equation 5.7 dominates and the line width increases linearly with impurity concentration. At concentrations below about 10 ppm the second term starts to dominate. At these concentrations, ^{13}C -electron dipolar interactions become more important than electron-electron dipolar interactions. It appears that hyperfine broadening of the EPR line by neighbouring ^{13}C nuclei does not contribute to the broadening of the EPR line significantly. Broadening by field inhomogeneities is also negligible.

Figure 5.2. The dependence of the P1 EPR line width on the concentration of P1 and P2 paramagnetic centres. The solid line represents the calculated values from equation 5.8.



Zhang *et al.* [5.6] reported a line width of 0.04 G in a synthetic type IIa diamond with $C_e = 0.1$ ppm and an abundance of 0.05%. Inserting this natural abundance (f) into equation 5.3, gives the second term in the expression for the second moment as $2.5 \times 10^{-4} \text{ G}^2$ and equation 5.7 becomes:

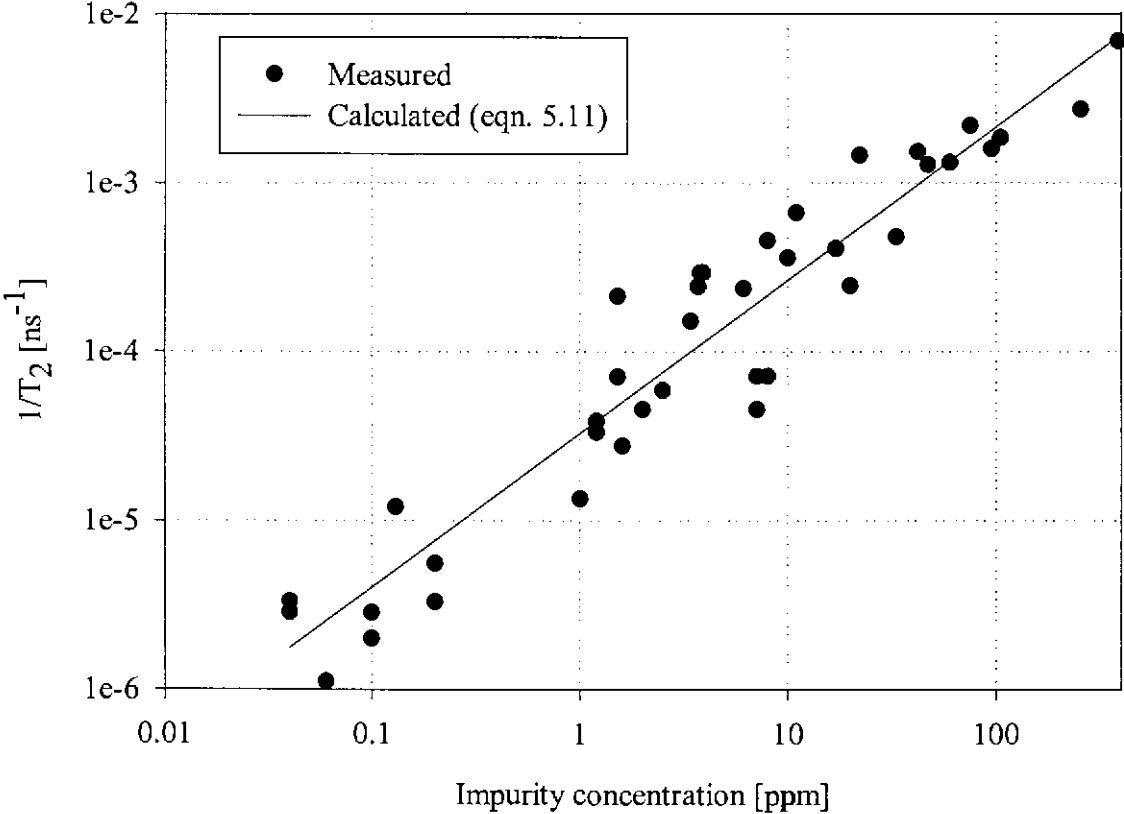
$$\delta = \sqrt{1.2 \times 10^{-4} C_e^2 + 0.014} \text{ G.} \quad 5.12$$

Inserting the value of 0.1 ppm yields a line width of 0.03 G, which is reasonably close to the value of 0.04 G for P1 centres quoted by Zhang *et al.* [5.6]

5.3.4 Impurity Concentration as a Function of Spin-Spin Relaxation Time

The data obtained in these measurements and the calculated values (solid line) are given in figure 5.3. Samples with observable P2 concentration are indicated. Good agreement between measured and calculated values was obtained. It was noted in these measurements that T_{2e} was the same for all of the hyperfine lines in samples containing only P1 centres (Ib diamonds) and with very low P2 concentrations. In diamonds with comparable P1 and P2 concentrations, in general, T_{2e} of the central line was shorter than for the hyperfine lines. Since P2 lines overlaps with the central P1 line they therefore contribute to the relaxation rate via cross relaxation mechanisms.

Figure 5.3. Dependence of the spin-spin relaxation rate of P1 centres in diamond, on the concentration of paramagnetic centres. The solid line represents the calculated relaxation times from equation 5.11



The impurity concentrations of the diamonds listed in table 3.2 were measured using this technique are listed in table 5.1 below.

Table 5.1. Impurity concentrations

Sample Reference	C_e	T_{2e}	C_e	T_{2e}
	Central line P1 + P2 (ppm)	Central line (μ s)	Hyperfine line P1 (ppm)	Hyper fine line (μ s)
B6	39.6 ± 2.0	1.8 ± 0.1	0.1 ± 0.02	800 ± 100
A10	44.6 ± 2.0	1.6 ± 0.1	0.13 ± 0.02	510 ± 20
B3	47.6 ± 2.0	1.5 ± 0.1	2.38 ± 0.02	30 ± 2
A13	28.6 ± 2.0	2.5 ± 0.1	0.52 ± 0.01	137 ± 6
B20	44.6 ± 2.0	1.6 ± 0.1	2.38 ± 0.02	30 ± 2
B2	51.0 ± 2.0	1.4 ± 0.1	9.3 ± 0.1	7.7 ± 0.2
B9	42.0 ± 4.0	1.7 ± 0.1	4.4 ± 0.1	16.3 ± 0.2

The above concentrations were determined using the equation 5.11 in the following form:

$$C_e = \frac{7.14 \times 10^{-5}}{T_{2e}} \text{ ppm}, \quad 5.13$$

where $1 \text{ ppm} \approx 10^{17} \text{ cm}^{-3}$.

5.4 Discussion

The measurement of T_{2e} of P1 paramagnetic centres in diamond is an effective method of determining the P1 concentration. Performing this measurement on the hyperfine line gives the P1 centre concentration only, while the measurement on the central line gives the combined P1 and P2 centre, concentration. At impurity concentrations above about 10 ppm the EPR line width is also an effective method of determining the total paramagnetic impurity concentration. For concentration below about 10 ppm the inhomogeneous broadening of the line by neighbouring ^{13}C nuclei results in a concentration independent line width and paramagnetic impurity concentration cannot be determined. However, in the case of T_{2e} , inhomogeneous broadening does not contribute to T_{2e} and the paramagnetic impurity concentration can therefore be determined to very low levels.

5.5 References

- [5.1] C. Kittel and E. Abrahams, *Phys. Rev*, **91**, 1071, (1953)
- [5.2] M. J. R. Hoch and E. C. Reynhardt, *Phys. Rev.*, **B37**, 9222, (1988).
- [5.3] J. A. van Wyk, E. C. Reynhardt, G. L. High, I. Kiflawi, *J. Phys. D: Appl. Phys.*, **30**, 1790, (1997).
- [5.4] J. Isoya, C. P. Lin, M. K. Bowman, J. R. Norris, S. Yazu and S. Sato, *Proc. 1st Int. Conf. New Diamond Sci. and Tech.*, Tokyo, Edited by S Saito *et al.*, (Tokyo: KTK Terra) 357, (1988).
- [5.5] I. Kiflawi, A. E. Spear, J. A. van Wyk and G. S. Woods, *Phil. Mag. B*, **69**, 1141, (1994).
- [5.6] S. Zhang, S. C. Ke, M. E. Zvanut, T. H. Tohver and Y. K. Vohra. *Phys. Rev. B*, **49**, 3019, (1993).

Chapter 6

Temperature Dependence of the Spin-Lattice and Spin-Spin Relaxation Times in Natural Diamond.



6.1 Theory.....	105
6.1.1 The Ideal Crystal Case.....	105
6.1.2 The Van Vleck Theory of Relaxation via Spin-orbit Coupling.	116
6.1.3 The Orbach Process of Relaxation via a Real Intermediate State.....	117
6.1.4 Jahn Teller Effect	118

6.1.5 Cross Relaxation Mechanisms	121
6.2 Results	122
6.2.1 Spin-lattice Relaxation Times	122
6.2.2 Spin-spin Relaxation Times	128
6.3 Discussion.....	128
6.4 References.....	131
APPENDIX 6A. The Strain Tensor	132
6A.1 One-dimensional strain.....	132
6A.2 Two-dimensional strain	133
6A.3 Three-dimensional strain.....	135

6.1 Theory

Thermal contact between a paramagnetic spin system and a heat reservoir is vital to the observation of magnetic resonance effects. Without this contact the radiation used to stimulate a magnetic resonance signal would heat the spin system to an infinite temperature after which no further absorption of energy can occur and the signal would disappear. A coupling mechanism, lattice phonons, between the spin system and heat reservoir was proposed by Waller [6.1] in the early 1930's, long before magnetic resonance experiments became routine. Energy transfer between the spin system and the lattice, i.e. spin-lattice relaxation, occurs when lattice vibrations cause the dipolar interaction between spins to fluctuate at a frequency that will stimulate transitions of the spins from one energy state to another. This frequency is generated as the distance between interacting spins is modulated about an equilibrium position. These distances can be expressed in terms of thermal strains in the crystal lattice.

The existence of the phonon spectrum gives rise to a number of processes through which relaxation can take place. The processes most likely to be applicable to diamond are discussed below.

6.1.1 The Ideal Crystal Case

The generation of phonons is explained in terms of the strain tensor that is discussed in Appendix 6A. The strain tensor can be expanded as a Taylor series. The first term in the expansion is linear in strain and accounts for the emission or absorption of a single phonon of energy $\hbar\omega_0$. This relaxation process is referred to as the *direct process*. The spin system energy changes by the Zeeman energy and the lattice energy changes by the same amount, thus conserving energy. The direct process leads to a linear dependence of the spin-lattice relaxation rate on temperature T , when $kT \ll \hbar\omega_0$, i.e. at low temperatures. This can be recognised from the fact that the Zeeman splitting for reasonable magnetic fields is of the order of a few kelvin, so only the low energy phonons participate in this process. Hence, only a small fraction of the phonon spectrum, with an even smaller density of states than for the predominant phonons, i.e. thermal

phonons with energy of the order of kT , participates in this process. From the foregoing one can deduce that this is a rather inefficient process which leads to slow relaxation rates in the low temperature regime.

At higher temperatures Waller [6.1] introduced a Raman-like process arising from the second order term in the expansion of the strain tensor. This process involves an inelastic two-phonon emission and absorption process, where a phonon is scattered off a paramagnetic ion and the difference between the initial and final energies of the incident and scattered phonon is $\hbar\omega_0$. This process includes the more abundant higher energy thermal phonons, which results in much higher relaxation rates, compared to the direct process. The Raman process leads to relaxation rates that depend on temperature as T^7 , for temperatures below the Debye temperature [6.2].

Before exploring other relaxation mechanisms and their associated temperature dependencies, some aspects of the phonon spectrum are discussed. In solids the attainment of thermal equilibrium can be broken down into two steps; first, the system reaches an internal thermal equilibrium with spin temperature T_s in a time T_2 . Secondly, the system tends to the lattice temperature T with a time constant $T_1 \gg T_2$. As mentioned earlier, the mechanism through which thermal equilibrium is reached with the lattice, is lattice vibrations or phonons. The basic problem is to determine the phonon spectrum in a lattice at a particular temperature.

A theoretical derivation of the phonon spectrum is given by Abragam [6.2] and begins by considering the motion of nuclei in a cubic lattice. The position of a nucleus is given by:

$$\bar{R} = \bar{r} + \bar{u}(\bar{r}) = \bar{p}a + \bar{u}_p, \quad 6.1$$

where a = lattice spacing,

\bar{r} = equilibrium position,

$\bar{u}_p = \bar{u}_p(t)$ = displacement from equilibrium and

$\bar{p} = (p_1, p_2, p_3)$ are integer values.

Assuming that there are N atoms in the lattice, then consequently there will be $3N$ degrees of freedom. Motion in the lattice is proportional to the time dependence of the $3N$ components of the N vectors $\bar{u}_p(t)$.

The time dependence of the $3N$ components is rather complicated, but one can construct $3N$ linear combinations of these components, called normal co-ordinates, which behave like harmonic oscillators and are defined by the wave-like expansion:

$$\bar{u}(\bar{r}) = \bar{u}_p = \sum_f \sum_{j=1}^3 q(\bar{f}, j) \exp\left(i \frac{\bar{r} \cdot \bar{f}}{a}\right) \bar{e}(\bar{f}, j), \quad 6.2$$

where $\bar{f} = (f_1, f_2, f_3)$ is the phase vector that has N discrete values in the interval $(-\pi, \pi)$.

The spacing between these phase points is $N/(2\pi)^3$. For $N \approx 10^{23}$ the phase vector can assume 10^{20} values and \bar{f} can therefore be considered as continuous. At each point in phase space there are 3 vectors $\bar{e}(\bar{f}, j)$ describing the motion and 3 normal co-ordinates $q(\bar{f}, j)$ where j is the polarisation index. Each normal co-ordinate obeys the laws of a harmonic oscillator i.e.:

$$\ddot{q}(\bar{f}, j) + \omega^2(\bar{f}, j)q(\bar{f}, j) = 0. \quad 6.3$$

The vibrational or phonon spectrum is determined by $\omega(\bar{f}, j)$'s dependence on the phase vector \bar{f} and the polarisation index j . An approximate solution is found by using Debye's assumption that the propagation velocity of the wave described by equation 6.2,

is independent of the direction of propagation and the polarisation of the wave [6.2]. The following relationship results:

$$\omega(\vec{f}, j) = \frac{v}{a} |\vec{f}|. \quad 6.4$$

The number of modes of oscillation $\sigma(\omega)$, having frequencies in the range ω and $\omega + d\omega$, is given by [6.2]:

$$\sigma(\omega) = \frac{3N}{8\pi^3} 4\pi f^2 df = \frac{3N}{8\pi^3} 4\pi \frac{a^3}{v^3} \omega^2 d\omega, \quad 6.5$$

and the phonon spectrum is obtained by integration of equation 6.5 to yield:

$$\int \sigma(\omega) d\omega = \int \frac{3N}{8\pi^3} 4\pi \frac{a^3}{v^3} \omega^2 d\omega \quad 6.6$$

or

$$\sigma(\omega) = \frac{3Na^3}{2\pi^2} \frac{\omega^2}{v^3}. \quad 6.7$$

Due to the fact that the number of modes is limited to $3N$, this number must also limit the above integral. The limit of integration in turn implies an upper cut-off frequency that is defined as Ω .

Performing the integration with the imposed limits, one obtains:

$$\int_0^{\Omega} \sigma(\omega) d\omega = 3N \quad 6.8$$

$$\int_0^{\Omega} \frac{3Na^3}{2\pi^2v^3} \omega^2 d\omega = 3N$$

$$\frac{1}{3} \omega^3 \Big|_0^{\Omega} = 2\pi \frac{v^3}{a^3},$$

so that the cut-off frequency is

$$\Omega = \sqrt[3]{(6\pi^2)} \frac{v}{a}, \quad 6.9$$

and the phonon spectrum is then given by

$$\sigma(\omega) = \frac{9N\omega^2}{\Omega^3}. \quad 6.10$$

The cut-off frequency is usually defined in terms of the Debye temperature, Θ , that is given by:

$$k\Theta = \hbar\Omega. \quad 6.11$$

For most substances the Debye temperature is of the order of 200 K to 300 K and the corresponding cut-off frequency is around $2\pi \times 10^{13}$ Hz. In the case of diamond, Θ is of the order of 2000 K, which gives $\Omega \approx 2\pi \times 10^{14}$ Hz [6.3].

The use of the word “phonons” to describe lattice vibrations by definition implies that such vibrations are quantised. For this discussion the co-ordinates, q , of the lattice oscillators are considered to be quantum mechanical operators. The wave like expansion given in equation 6.2 is re-written as:

$$\bar{u}_p = \sum_f \sum_{j=1}^3 \bar{e}(\bar{f}, j) \left\{ q(\bar{f}, j) \exp\left(i \frac{\bar{r} \cdot \bar{f}}{a}\right) + q^*(\bar{f}, j) \exp\left(-i \frac{\bar{r} \cdot \bar{f}}{a}\right) \right\}, \quad 6.12$$

where q and q' are quantum mechanical operators that are hermitian and conjugate.

For every mode (\bar{f}, j) there is a lattice oscillator with a frequency $\omega(\bar{f}, j)$ and a corresponding set of energy levels $\left(n + \frac{1}{2}\right) \hbar \omega(\bar{f}, j)$, where n is an integer. The only non-vanishing matrix elements of the operators q and q' are:

$$(n|q|n+1) = (n+1|q^*|n) = \left(\frac{\hbar}{2M}\right)^{\frac{1}{2}} \omega^{\frac{1}{2}} \exp(-i\omega t) \sqrt{(n+1)}, \quad 6.13$$

where $M = Nm$ is the mass of the crystal and m the mass of a single atom or ion.

One can then describe a particular situation where a lattice oscillator (\bar{f}, j) is in an energy state $|n\rangle$ by saying there are n lattice phonons (\bar{f}, j) in the crystal. With this convention, operator q describes the absorption and q' the release or creation of phonons. Phonons obey Bose statistics so that the number $n(\bar{f}, j)$, of phonons (\bar{f}, j) , present in a crystal at a temperature T will be given by Planck's law:

$$n(\bar{f}, j) = \left[\exp \frac{\hbar \omega(\bar{f}, j)}{kT} - 1 \right]^{-1}. \quad 6.14$$

The next step in determining how the phonon spectrum affects the relaxation rate requires an understanding of the transition probability induced by the spin-phonon coupling. The connection between transition probability and relaxation rate is given in Waller's theory by $1/T_1 \approx W$ [6.1] and can be represented mathematically by a Hamiltonian:

$$\hbar H = \hbar \sum_q F^{(q)} A^{(q)}, \quad 6.15$$

where $F^{(q)}$ and $A^{(q)}$ are lattice and spin operators, respectively. F has units of frequency and A is dimensionless with matrix elements of the order of unity. The operator F is a function of the relative positions of two neighbouring nuclei or ions in the lattice. The relative positions are given by:

$$\bar{R}_{12} = \bar{R}_1 - \bar{R}_2 = \bar{r}_1 - \bar{r}_2 + \bar{u}_1(\bar{r}_1) - \bar{u}_2(\bar{r}_2). \quad 6.16$$

If one expands $\bar{u}_1(\bar{r}_1)$ and $\bar{u}_2(\bar{r}_2)$ as a Taylor series (consider only the x component here) one obtains:

$$\bar{u}_1(\bar{r}_1)_x = \bar{u}_1(0)_x + \bar{r}_1 \cdot \frac{\partial \bar{u}_1(\bar{r}_1)}{\partial x} + \bar{r}_1^2 \cdot \frac{\partial^2 \bar{u}_1(\bar{r}_1)}{\partial x^2} + \dots \quad 6.17$$

and

$$\bar{u}_2(\bar{r}_2)_x = \bar{u}_2(0)_x + \bar{r}_2 \cdot \frac{\partial \bar{u}_2(\bar{r}_2)}{\partial x} + \bar{r}_2^2 \cdot \frac{\partial^2 \bar{u}_2(\bar{r}_2)}{\partial x^2} + \dots \quad 6.18$$

so that to a first approximation the component $(\bar{u}_1 - \bar{u}_2)_x$ is given by:

$$(\bar{u}_1 - \bar{u}_2)_x = \bar{u}_1(0) - \bar{u}_2(0) + \bar{r}_1 \frac{\partial \bar{u}_1(\bar{r}_1)}{\partial x} - \bar{r}_2 \frac{\partial \bar{u}_2(\bar{r}_2)}{\partial x}. \quad 6.19$$

If one assumes that $\bar{u}_1(0) \approx \bar{u}_2(0)$ and $\frac{\partial \bar{u}_1(\bar{r}_1)}{\partial x} = \frac{\partial \bar{u}_2(\bar{r}_2)}{\partial x}$ equation 6.19 becomes:

$$\bar{R}_{12x} = \bar{r}_{1x} - \bar{r}_{2x} + \bar{r}_1 \frac{\partial \bar{u}_1(\bar{r}_1)}{\partial x} - \bar{r}_2 \frac{\partial \bar{u}_1(\bar{r}_2)}{\partial x} \quad 6.20$$

The assumption that \bar{u} does not change appreciably over an atomic distance a is only true for wavelengths $\lambda = 2\pi v/\omega$, which are much greater than the inter-atomic spacing. The assumption will no longer hold when $\omega \approx \Omega$, but will not affect the order of magnitude of the results that follow.

Based on the foregoing, the frequency operator F can be expanded as a function of stresses in a crystal. The stress W_{ik} is related to the displacement vector \bar{u} as follows:

$$W_{ik} = \frac{1}{2} \left(\frac{\partial u_i}{\partial x_k} + \frac{\partial u_k}{\partial x_i} \right) \quad (i, k = 1, 2, 3) \quad 6.21$$

Again, using a Taylor expansion, the frequency operator can be written as:

$$F = F_0 + F_1 W + F_2 W^2 + F_3 W^3 + \dots, \quad 6.22$$

where these terms have the following form: $F_1 W = \sum_{i,k} F_{1,ik} W_{ik}$. The operator F_1 is a two-index tensor, F_2 a four-index tensor and so on. The magnetic coupling between two spins is then given by:

$$\hbar H_1 \approx \hbar F A \approx \frac{\gamma_1 \gamma_2 \hbar^2}{R^3} \left\{ \bar{I}_1 \cdot \bar{I}_2 - \frac{3(\bar{I}_1 \cdot \bar{R})(\bar{I}_2 \cdot \bar{R})}{R^2} \right\}, \quad 6.23$$

with

$$F_0 = \frac{\gamma_1 \gamma_2 \hbar^2}{r^3}; \quad F_1 = r \frac{\partial F_0}{\partial r}; \quad F_2 = r^2 \frac{\partial^2 F_0}{\partial r^2}; \text{ etc.} \quad 6.24$$

The first term in equation 6.22, F_1W , accounts for the direct process and has an associated probability [6.2] of:

$$P_1 \approx 9\pi F_1 \frac{F_1 \omega_0^2}{\Omega^3} \frac{kT}{mv^2} \approx 9\pi \Omega \left(\frac{F_1}{\Omega} \right)^2 \left(\frac{\omega_0}{\Omega} \right)^2 \left(\frac{k\Theta}{mv^2} \right) \left(\frac{T}{\Theta} \right) \approx \frac{1}{T_1}. \quad 6.25a$$

where v is the velocity of sound in diamond.

Rewriting equation 6.25a in the nomenclature used by Pake [6.4], the relaxation rate becomes:

$$\frac{1}{T_1} \approx \frac{54\pi v^2}{\hbar^2 \rho v^5} \left(\frac{\beta^2}{r^3} \right)^2 kT. \quad 6.25b$$

The relaxation rate due to the direct process is therefore dependent on the velocity of sound in diamond as v^5 , which results in a relatively low relaxation rate.

It follows that T_1 is linearly dependent on temperature T and proportional to the square of frequency ω_0^2 (or field H_0^2). This can be summarised as follows:

$$\frac{1}{T_1} = CH_0^2 T. \quad 6.26$$

The physical reason for the inefficiency of the direct process is the low spectral density of phonons with a frequency close to ω_0 which can stimulate such a transition.

The second term in equation 6.22 (i.e. F_2W^2) accounts for two phonon processes that induce transitions. The *Raman process*, which involves the absorption of one phonon and the emission of another, is discussed here. This process is far more effective in

stimulating transitions as the spectral density of phonons that are able to contribute to this mechanism is many times higher than for the direct process.

These phonons must satisfy the relationship $\omega - \omega' = \omega_0$, and ω can take on any value between ω_0 and Ω . It is important to note that phonons satisfying the relationship $\omega + \omega' = \omega_0$ will also stimulate transitions, but the spectral density of phonons satisfying this relationship will also be limited by the same way the direct process was. The transition probability is then given by [6.2]:

$$\begin{aligned}
 P_2 &\approx \frac{2\pi}{\hbar} \int \sigma(\omega) \hbar^2 F_2^2 \frac{\omega^4}{v^4} \frac{n(n+1)\hbar^2}{4M^2\omega^2} \frac{\sigma(\omega)}{\hbar} d\omega \\
 &\approx \frac{81\pi}{2} \left(\frac{F_2\hbar}{mv^2} \right) \int_0^\Omega \frac{\exp(\hbar\omega/kT)}{(\exp(\hbar\omega/kT)-1)^2} \frac{\omega^6}{\Omega^6} d\omega.
 \end{aligned} \tag{6.27}$$

In the high temperature limit, i.e. when $T \approx \Theta$, then $kT \gg \hbar\Omega$ and one can expand $\exp(\hbar\omega/kT)$ as $1 + \hbar\omega/kT$ to obtain:

$$\begin{aligned}
 P_2 &\approx \frac{81\pi}{10} \left(\frac{kT}{mv^2} \right)^2 \frac{F_2^2}{\Omega} \approx \frac{81\pi}{10} \left(\frac{\hbar F_2}{mv^2} \right)^2 \Omega \left(\frac{T}{\Theta} \right)^2 \\
 P_2 &\approx \frac{81\pi}{10} \left(\frac{F_2}{\Omega} \right)^2 \left(\frac{k\Theta}{mv^2} \right)^2 \left(\frac{T}{\Theta} \right)^2 \Omega
 \end{aligned} \tag{6.28}$$

i.e. the transition probability P_2 is proportional to T^2 and ω_0 .

In the low temperature limit, i.e. $T \ll \Theta$, we introduce a variable $x = \hbar\omega/kT$ such that $X = \hbar\Omega/kT = \Theta/T$. The transition probability then becomes:

$$P_2 \approx \frac{81\pi}{2} \left(\frac{F_2 \hbar}{mv^2} \right)^2 \left(\frac{T}{\Theta} \right)^7 \Omega \int_0^X \frac{x^6 e^x}{(e^x - 1)^2} dx. \quad 6.29a$$

In the limit as $X \rightarrow \infty$, $P_2 \propto T^7$.

Rewriting equation 6.29a in the nomenclature used by Pake [6.4], yields a relaxation rate of:

$$\frac{1}{T_1} \approx \frac{163\pi^2 6!}{\rho^2 v^{10}} \left(\frac{\beta^2}{r_3} \right)^2 \left(\frac{kT}{h} \right)^7. \quad 6.29b$$

The relaxation rate for the Raman process is therefore dependent on the velocity of sound as v^{10} , which will result in a relatively low relaxation rate.

To summarise, the characteristics of the relaxation rate for the Raman process for $T \geq \Theta$ are its direct dependence on the frequency ω_0 and the square of temperature, T^2 . For $T \ll \Theta$ the temperature dependence of the relaxation rate goes as T^7 , or in mathematical terms:

$$\frac{1}{T_1} = \begin{cases} C'H_0 T^2 & \text{for } T \geq \Theta \\ C''H_0 T^7 & \text{for } T \ll \Theta \end{cases}$$

If we now compare the transition probability for the direct process P_1 to the transition probability for the Raman process P_2 , assuming that $F_1 \approx F_2$, we get:

$$\frac{P_2}{P_1} \approx \frac{kT}{mv^2} \left(\frac{\Omega}{\omega_0} \right)^2, \quad 6.30$$

where

$$\frac{kT}{mv^2} = \frac{N_0 kT}{N_0 mv^2} = \frac{RT}{Av^2} \quad 6.31$$

For the following typical values:

$$\begin{aligned} R &= 8.4 \times 10^7 \text{ J K}^{-1}, \\ T &= 300 \text{ K}, \\ A &= 20 \text{ and} \\ v^2 &= 10^5 \text{ m/s with } kT/mv^2 = 0.03. \end{aligned}$$

and for a reasonable magnetic field (around 1 Tesla), $\omega_0 \approx 10^9$ (for electrons) and $\Omega \approx 10^{14}$ so that:

$$\frac{P_2}{P_1} \approx 0.03 \times \left(\frac{10^{14}}{10^9} \right)^2 = 3 \times 10^8. \quad 6.32$$

This large number emphasises the importance of the Raman process over the direct process.

In perfect crystals the above theory would be adequate to model the relaxation rate as a function of temperature, but in the case of natural diamond these models do not account adequately for the observed behaviour. Diamond crystals have many defects that can contribute to the relaxation rate in various temperature regimes. The most pertinent and probable relaxation mechanisms are discussed below.

6.1.2 The Van Vleck Theory of Relaxation via Spin-orbit Coupling.

The mechanisms proposed by Waller [6.1] generally give T_1 's that are longer than those observed experimentally. Kronig [6.5] suggested that lattice phonons could influence T_1 by modulating the crystalline electric field. This effect is then experienced by the spins via spin-orbit coupling [6.6]. Van Vleck made calculations of T_1 based on the work of

Finn *et al.* [6.7] in which the Jahn Teller effect (see later) is analysed. The results of these calculations are [6.8].

For the direct process:

$$\frac{1}{T_1} \approx CH_0^4 T. \quad 6.33$$

For the Raman process one again considers two temperature regimes [6.4]:

$$\frac{1}{T_1} = \begin{cases} CH_0^0 T^9 & (T \ll \Theta) \\ CH_0^0 T^0 & (T \geq \Theta) \end{cases} \quad 6.34$$

The observed temperature dependence of the spin-lattice relaxation rate for diamond does not comply with this theory, so it is not pursued further.

6.1.3 The Orbach Process of Relaxation via a Real Intermediate State.

In this process, conceived by Orbach *et al.* [6.9], an ion in the upper Zeeman level can absorb a phonon and be excited into an intermediate state (for example a low-lying crystal-field excited state) and then drop back to the lower Zeeman level. Orbach [6.9] calculated this relaxation rate to have the following form:

$$\frac{1}{T_1} = \left(\frac{3G^2}{h\rho\nu_0^5} \right) \left(\frac{\Delta}{\hbar} \right)^3 \exp\left(-\frac{\Delta}{kT} \right), \quad 6.35$$

where Δ is a temperature corresponding to the crystal field level and G is a coefficient in the strain tensor that gives the change in crystal-field energy under strain. Details of such calculations can be found in another paper by Orbach [6.9]. The observed temperature dependence of the spin-lattice relaxation time, T_{1e} , of paramagnetic impurities in diamond, is not in agreement with the theory of the Orbach process. Therefore, it can be

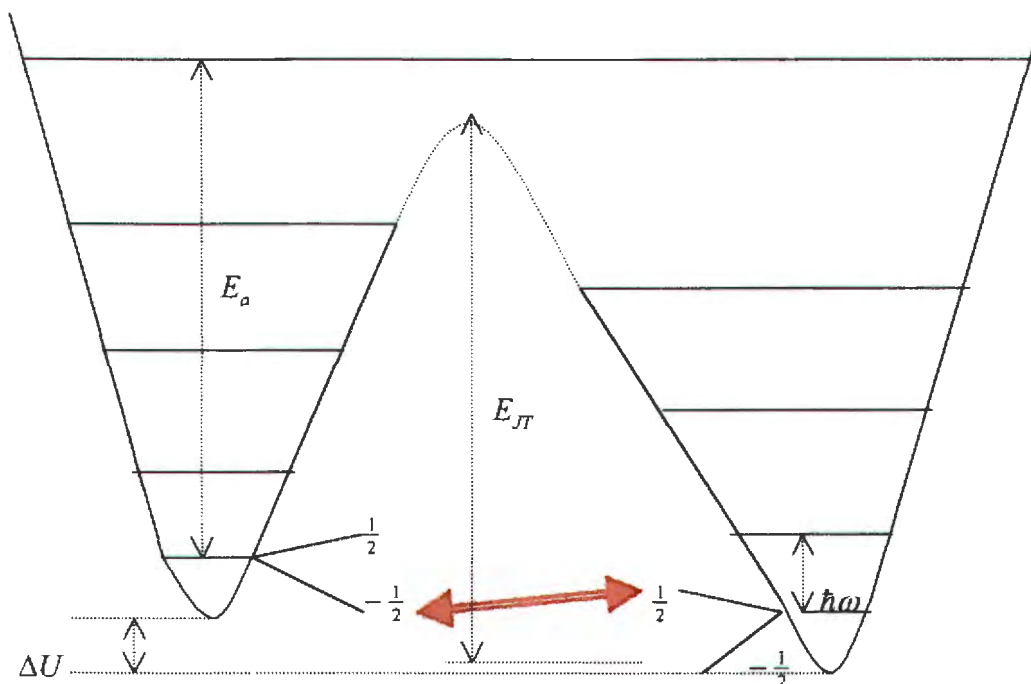
assumed that spin-lattice relaxation in the suite of diamonds under consideration, does not proceed via an intermediate state.

6.1.4 Jahn Teller Effect

Nitrogen in diamond forms typical Jahn Teller centres [6.10]. These centres occur when an ion is at a site of symmetry sufficiently high that a degenerate state would result for a rigid environment. The actual (elastic) environment spontaneously distorts to lift that degeneracy and lower the overall energy of the ion and its environment [6.11].

These centres can have considerable effect on the spin-lattice relaxation rate if reorientation occurs at a rate comparable to the electron Larmor frequency, $\omega_{0e} \approx 1/\tau_{JT} \approx 10^9$ Hz. Zaristkii *et al.* [6.10] mention two temperature regimes where Jahn Teller effects could be dominant. The first, at temperatures well below the Debye temperature, i.e. around 570 K, where the “static” Jahn Teller effect is active, and the second at temperatures around 900 K, where the “dynamic” Jahn Teller effect is active. The static Jahn Teller effect has a reorientation rate much lower than that associated with hyperfine interactions in diamond and the EPR spectrum is unaltered in this temperature regime. In the higher temperature regime, the reorientation rate is comparable or faster than the rate associated with hyperfine interactions and the EPR spectra is altered dramatically. In spite of this, at room temperature, the reorientation rate of static Jahn Teller centres may affect the spin-lattice relaxation rate of diamond. Zaristkii *et al.* [6.10] consider a spin-lattice relaxation mechanism, typical of Jahn Teller centres, that has a rate comparable to the standard spin-lattice relaxation rate so that $\tau_{JT} \approx \tau_{1e}$. The Jahn Teller mechanism may be spin-orbit phonon-induced tunnelling between various orientation states, which may result in an alteration of the projection of the electron spin. This process is shown schematically in figure 6.1 (after Zaristkii *et al.* [6.10]), where two of the four potential wells of a P1 centre are shown. These wells represent the four possible positions that a paramagnetic electron can assume. The double red arrow indicates the spin-lattice relaxation process in this system. The quantity $\hbar\omega$ is the energy of the vibrational states and ΔU is the difference in energy between the two states.

Figure 6.1. Schematic diagram of two of the potential wells in the four-well-potential of nitrogen in diamond. The double red arrow indicates the relaxation process.



The experimental results obtained by Zaritskii *et al.* [6.10] for the spin-lattice relaxation rates of nitrogen impurities in diamond indicated that the spin-lattice relaxation rate goes with temperature as:

$$\frac{1}{T_{1e}} = aT + bT^4 \quad 6.36a$$

and

$$\frac{1}{T_{1e}} = aT + bT^5, \quad 6.36b$$

for the two synthetic diamonds with nitrogen impurity concentrations of $N_a = 8 \times 10^{17} \text{ cm}^{-3}$ and $N_a = 9 \times 10^{18} \text{ cm}^{-3}$, respectively.

Zaritskii *et al.* [6.10] derived the relationship between spin-orbit phonon tunnelling and the relaxation rate for $kT \gg \Delta U$, the energy difference between two orientation states is:

$$\frac{1}{\tau_1} = \frac{12\lambda'_{ij}{}^2}{\pi\hbar k T_0} \left[\frac{T}{T_0} + \frac{3}{10} \left(\frac{T}{T_0} \right)^5 + \dots \right], \quad 6.37$$

where $\lambda'_{ij} = \langle j - | \mathbf{H}_{SO} | i + \rangle$, is the tunnelling matrix element of the electron spin-orbit operator and $T_0 = \frac{1}{\hbar} \sqrt{\frac{18\hbar^3 \rho v^5}{S}}$, with S a quadratic form describing the potential wells of the defect centre. Simplifying this equation yields:

$$\frac{1}{T_1} = \frac{K}{T_0^2} T + \frac{3}{10} \frac{K}{T_0^6} T^5 = aT + bT^5, \quad 6.38$$

where

$$K = \frac{12\lambda'^2}{\pi\hbar k}.$$

Rewriting K and T_0 in terms of a and b yields:

$$K = \sqrt{\frac{3}{10} \frac{a^3}{b}}$$

and

$$T_0 = \sqrt[4]{\frac{3}{10} \frac{a}{b}}$$

with

$$a = \frac{K}{T_0^2}$$

and

$$b = \frac{3}{10} \frac{K}{T_0^6}$$

This theory appears to describe the observed behaviour in diamond adequately and will be used in the discussion of the experimental results.

6.1.5 Cross Relaxation Mechanisms

This mechanism was proposed by Bloembergen *et al.* [6.12] for the establishment of thermal equilibrium between two nuclear species where a simultaneous flip-flop of two such spins does not conserve Zeeman energy. Abragam and Procter [6.13] discuss a similar process in their investigation into the concept of spin temperature. This process is only possible if the lines of the two resonances overlap. The probability, $W = 1/\tau$, of such a transition will be equal to the probability of a flip-flop, where Zeeman energy is conserved, i.e. $1/T_2$, multiplied by a factor describing the degree of overlap of the resonance lines. This overlap factor is of the form:

$$g(\nu) = \frac{\int G_a(\nu_a + u)G_b(\nu_b + u)du}{G_a(\nu_a)} \quad 6.39$$

In this equation a and b refer to two nuclear species with normalised line shape functions centred around ν . The variable u describes the widths of the resonance lines.

If gaussian line shapes are assumed and substituted into this equation it reduces to:

$$\exp\left(-\frac{[\nu_a - \nu_b]^2}{2[M_a^2 - M_b^2]}\right), \quad 6.40$$

where the M 's are the second moments of the respective lines. Due to the very sharp fall-off of the gaussian line shape, the overlap between the resonance lines is extremely small and the estimate of the contribution to the relaxation rate will also be small. A higher order transition, proposed by Abragam [6.2], involves the simultaneous flips of one spin of species a and two of species b . The energy $\hbar(\omega_a - 2\omega_b)$ associated with this process is more than three times lower than the two-spin process energy $\hbar(\omega_a - \omega_b)$. This mechanism can be thought of as an overlap of the line associated with species a with a satellite line associated with species b , occurring at $2\nu_b$. Replacing the energy of the two-spin process with the three-spin process in the above exponential, increases the overlap and hence the transitions probability. This is now given by:

$$\frac{1}{\tau} = \frac{1}{T_2} \frac{\langle \Delta \nu^2 \rangle_b}{\nu_b^2} \exp\left(\frac{-[\nu_a - 2\nu_b]^2}{2[M_a^2 - M_b^2]}\right). \quad 6.41$$

The factor $\langle \Delta \nu^2 \rangle_b / \nu_b^2$ accounts for the difference in area in the central and satellite lines. No overlap between hyperfine and central lines occurs in diamond so this relaxation method is not applicable. A further observation is that if the satellite line is orientation dependent, as is the case in diamond, then this contribution to the relaxation rate will also be orientation dependent. No such behaviour was observed in diamond.

6.2 Results

6.2.1 Spin-lattice Relaxation Times

The spin-lattice relaxation times, for the diamonds described above, are shown as a function of temperature in figures 6.2 to 6.6 below.

Figure 6.2. Temperature dependence of the spin-lattice relaxation time for central and hyperfine lines of diamond sample DL03. The solid lines represent the Jahn Teller model.

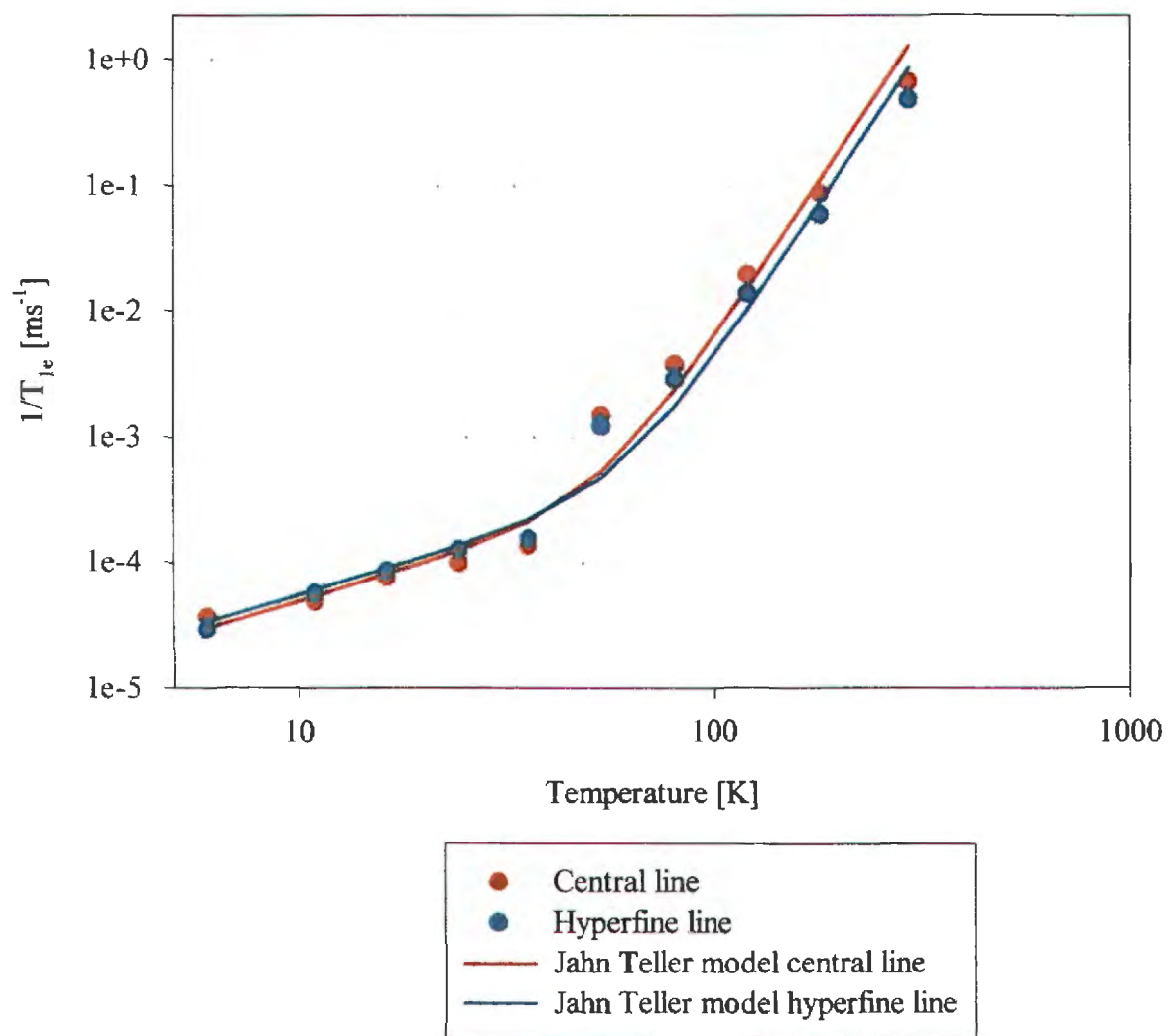


Figure 6.3. Temperature dependence of the spin-lattice relaxation time for central and hyperfine lines of diamond sample DL02. The solid lines represent the Jahn Teller model.

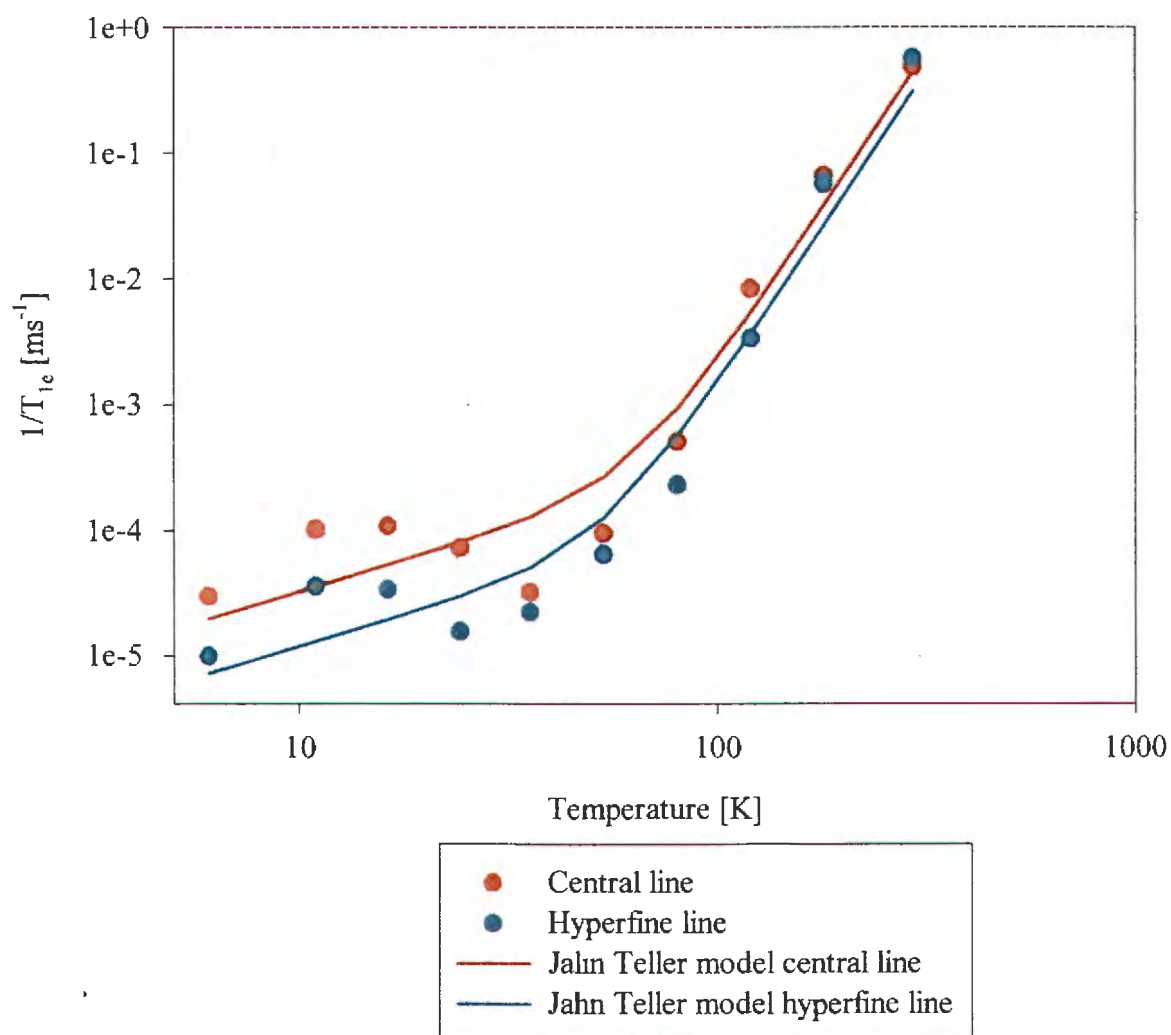


Figure 6.4 Temperature dependence of the spin-lattice relaxation time for central and hyperfine lines of diamond sample B2. The Jahn Teller model is not applicable here.

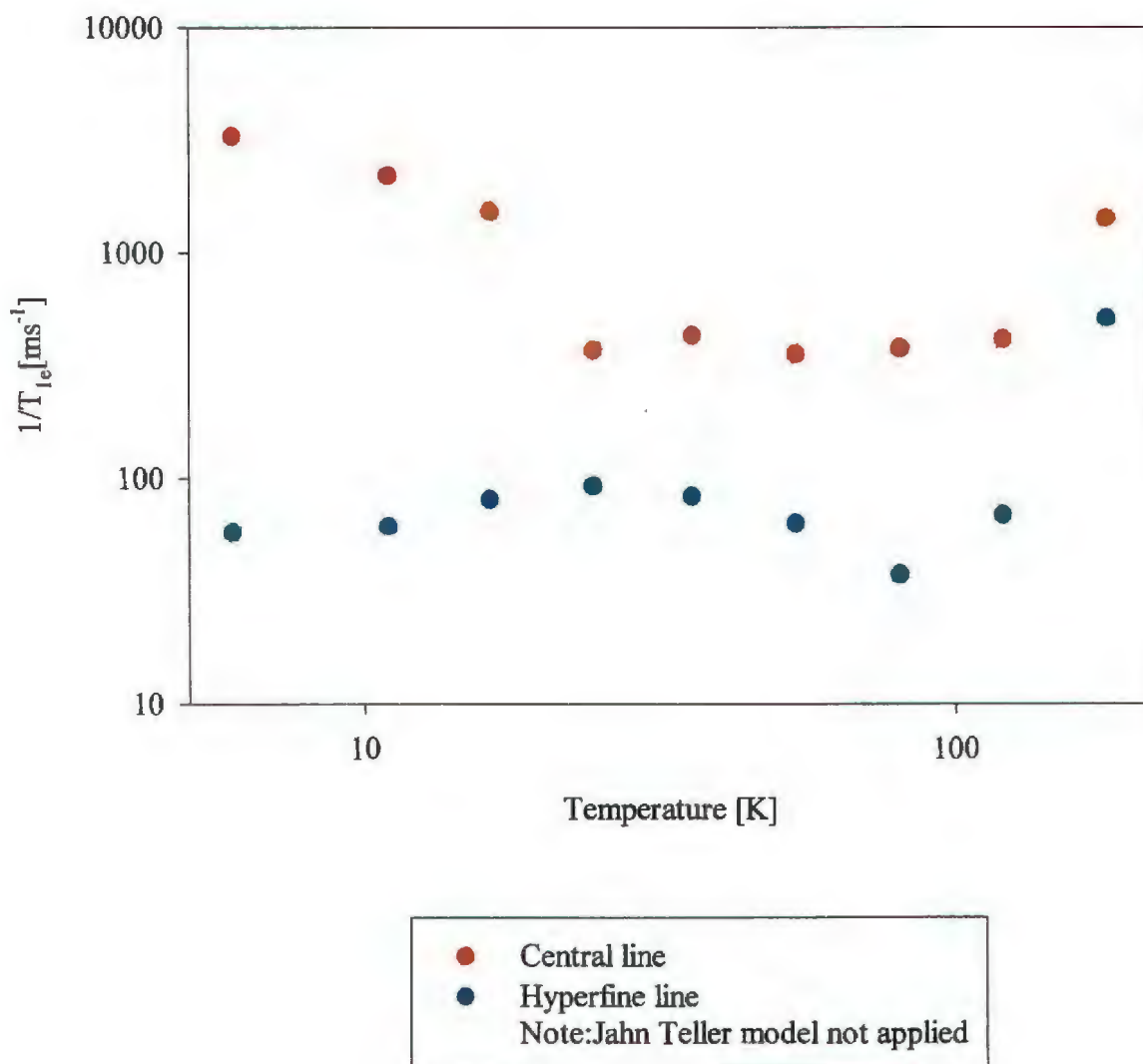


Figure 6.5. Temperature dependence of the spin-lattice relaxation time for central and hyperfine lines of diamond sample D10. The Jahn Teller model is not applicable here.

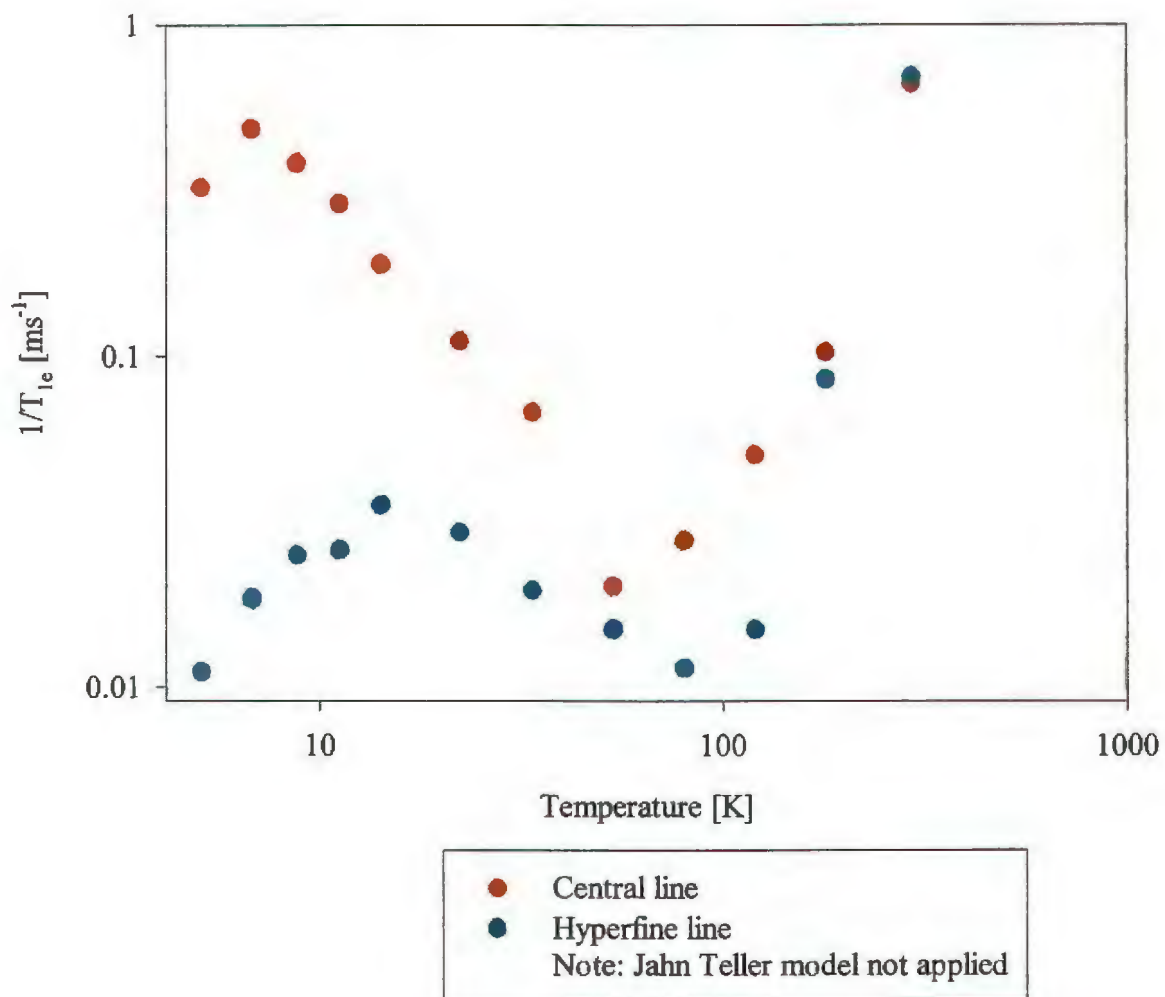
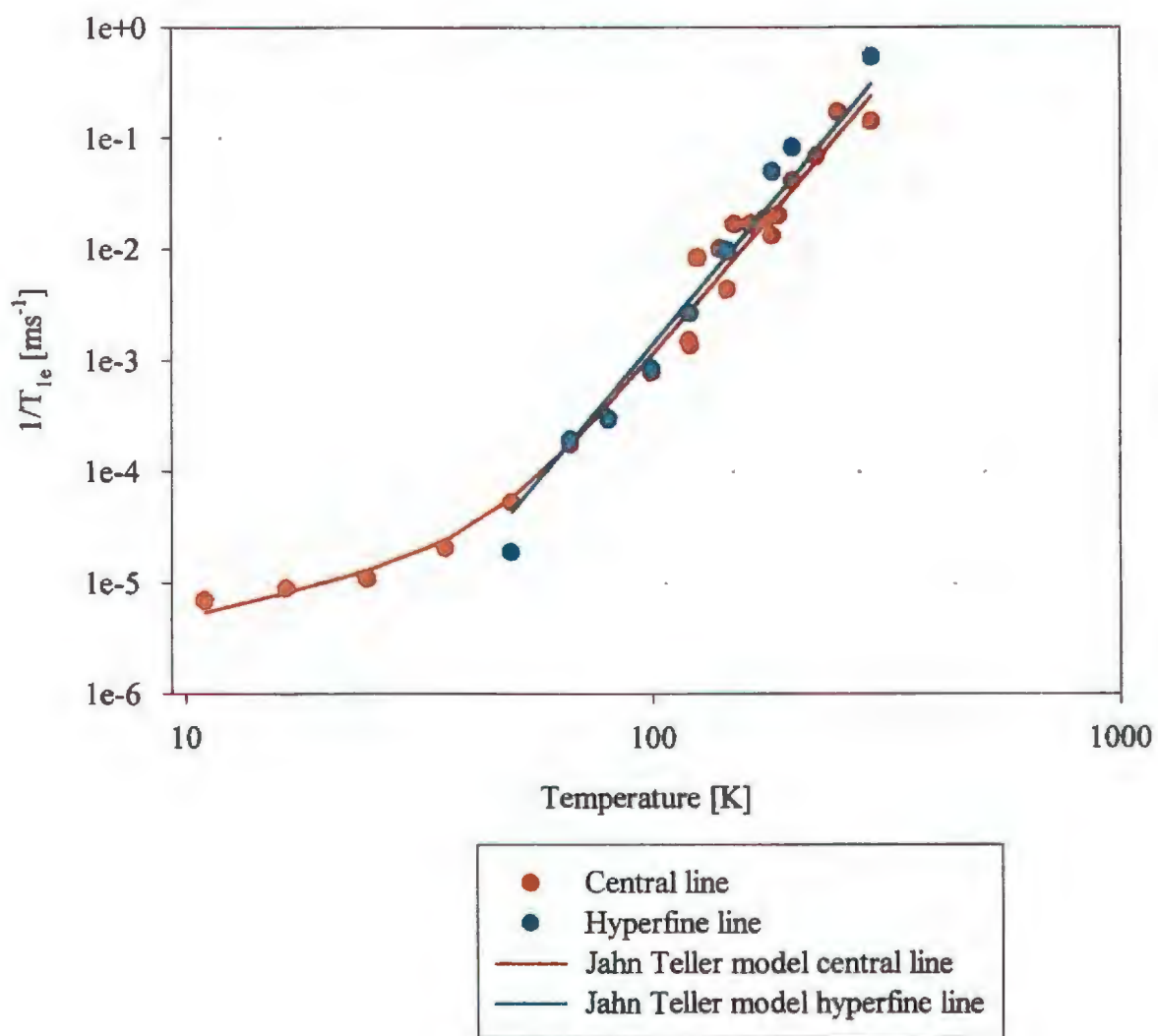


Figure 6.6. Temperature dependence of the spin-lattice relaxation time for central and hyperfine lines of diamond sample E4. The solid line represents the Jahn Teller model.



The behaviour of samples DLO3, DLO2 and E4 can be adequately described by the Jahn Teller model (solid lines in the figures) with the values of the coefficients a and b given in the table below

Table 6.2. Summary of curve fitting results

Sample	Central Line			Hyperfine Line		
	a [$\times 10^{-3}$ K/s]	b [$\times 10^{-10}$ K/s]	R^2	a [$\times 10^{-3}$ K/s]	b [$\times 10^{-10}$ K/s]	R^2
DLO3	5.0	5.9	0.998	5.6	3.3	0.998
DLO2	3.3	2.0	0.997	1.2	1.4	0.997
E4	0.5	1.1	0.769	0.0	1.4	0.995
D10	-	-	-	-	-	-
B2	-	-	-	-	-	-

6.2.2 Spin-spin Relaxation Times

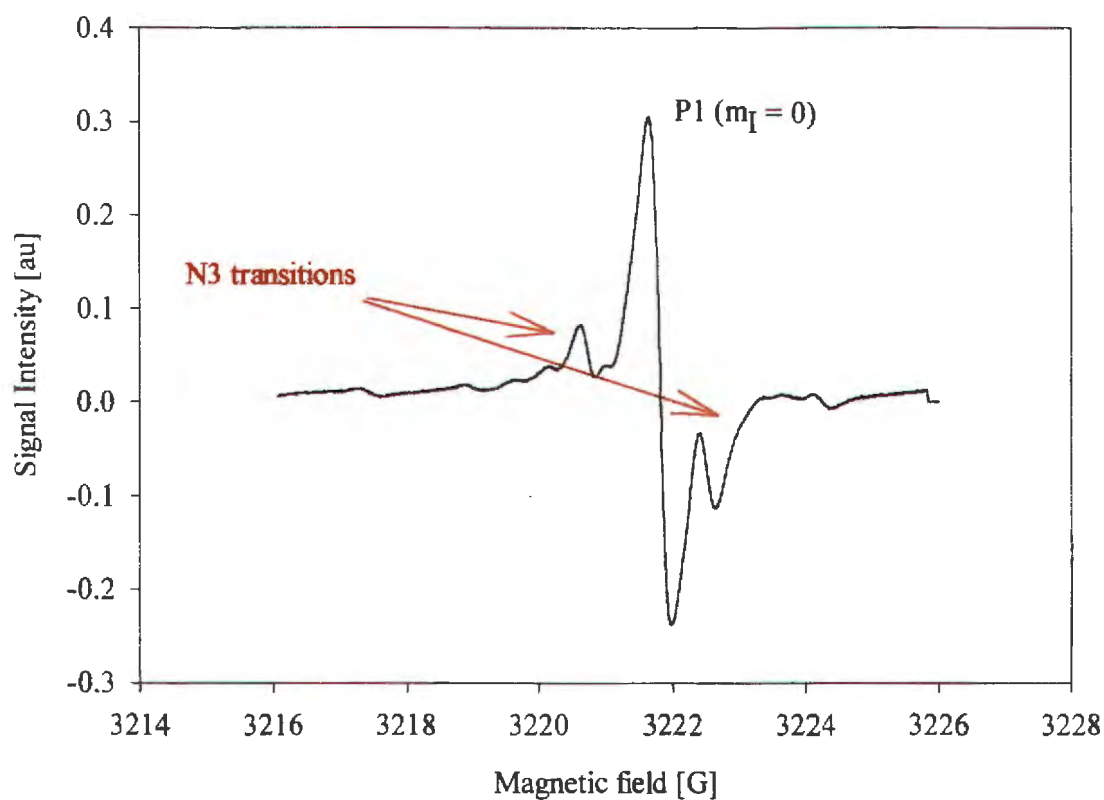
The spin-spin relaxation times of all the samples were found to be approximately temperature independent down to 4.2 K. Since the volume expansion coefficient for diamond is relatively low i.e. $\alpha \approx 0.8 \pm 0.1 \times 10^{-6}$ at 293 K and $\alpha \approx 0.4 \pm 0.1 \times 10^{-6}$ at 193 K [6.3], the paramagnetic impurity concentration is constant and the lattice is rigid, it is expected that T_{2e} should show very little variation with temperature.

6.3 Discussion

Samples D10 and B2 (and perhaps NLO2 as well) display some anomalous behaviour in the temperature range from around 20 K to 100 K. Over this temperature range, as the temperature decreases, the relaxation rate first increases and then decreases again as it approaches about 20 K. This behaviour would appear to indicate a process where an impurity makes transitions between lattice positions at a rate which would stimulate the relaxation process. It is interesting to note that these samples all contain N3 centres and it seems likely that these centres supply a relaxation mechanism, which is much more

effective at lower temperatures than the other relaxation mechanisms that have been discussed. The ESR spectrum of a sample containing N3 centres is shown in figure 6.7. The model of the N3 centre was discussed in chapter 4 and illustrated in figure 4.3 [6.14]. From the areas of the ESR lines it follows that samples D10 and B2 contain high and low relative concentrations of N3 centres, respectively. The higher concentration of N3 in sample D10 seems to result in a faster relaxation rate than observed in sample B2 in the same temperature range. One cannot draw too many conclusions from the results obtained for these two diamonds but the results support the suggestion that the N3 centres are responsible for the faster electron relaxation rates in these samples. Further investigation of this relaxation rate and the precise nature of the relaxation mechanism is recommended for further research.

Figure 6.7. EPR spectrum with the line associated with the N3 centre, indicated.



The results of this study indicate that P1 centres in diamond are typical Jahn Teller centres in agreement with the results of Zaritskii *et al.* [6.10]. The presence of other less common impurities, such as the N3 centre mentioned above, might be responsible for some interesting effects that influence relaxation in diamond. Many defects in diamond have been reported and theorised about in the literature and should be the subject of further investigations by these techniques. This information may aid in the understanding of the nature and form of these defects.

6.4 References

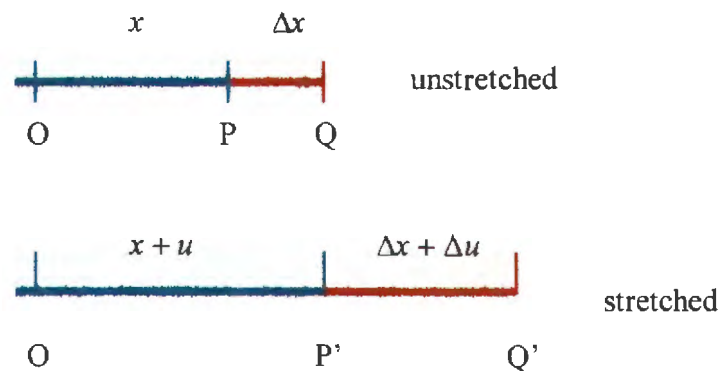
- [6.1] Waller I., *Z. Physik*, **79**, 370, (1932).
- [6.2] A. Abragam, *Principles of Nuclear Magnetism*, (Oxford University Press, 1961).
- [6.3] J. E. Field, *The Properties of Natural and Synthetic Diamond*, (Academic Press, 1992).
- [6.4] G. E. Pake, *Paramagnetic Resonance. An Introductory Monograph*, (W. A. Benjamin, Inc., New York, 1962)
- [6.5] Kronig R. de L., *Physica*, **6**, 33, (1939).
- [6.6] J. H. Van Vleck, *Phys. Rev.*, **74**, 1168, (1948).
- [6.7] C. P. B.Finn, R. Orbach R, W. P. Wolf, *Proc. Phys. Soc, (London)*, **A77**, 261, (1961).
- [6.8] J. H. van Vleck, *Phys.Rev.* **57**, 426, (1970).
- [6.9] R. Orbach, *Proc. Phys. Soc, (London)*, **A77**, 821, (1961).
- [6.10] I. M. Zaritskii, V. Ya. Bratus, V. S. Vikhnin, A. S. Vishnevskii, A. A. Konchits and V. M. Ustinstev, *Sov. Phys. Solid State*, **18**, (1976).
- [6.11] H. A. Jahn and E. Teller, *Proc. Roy. Soc. (London)* **A161**, 220, (1937).
- [6.12] N. Bloembergen, S. Shapiro, P. S. Pershan, J. O. Artman, *Phys. Rev.*, **114**, 445, (1959).
- [6.13] A. Abragam and W. G. Procter, *Phys. Rev.*, **109**, 1441, (1958).
- [6.14] J. A. Van Wyk, J. H. N. Loubser, M. E. Newton and J. M. Baker, *J Phys. Condens. Matter*, **4**, 107, (1992).

APPENDIX 6A. The Strain Tensor

The state of deformation in a solid due to thermal stresses is explained by first considering the simpler one-dimensional and two-dimensional cases. The strain tensor for three dimensions is then given.

6A.1 One-dimensional strain

Consider the piece of string shown in the figure below:



The strain is defined as the increase in length compared to the original length. In terms of the variables given in the diagram above:

$$w = \frac{\Delta x + \Delta u - \Delta x}{\Delta x} = \frac{\Delta u}{\Delta x} \quad 6A.1$$

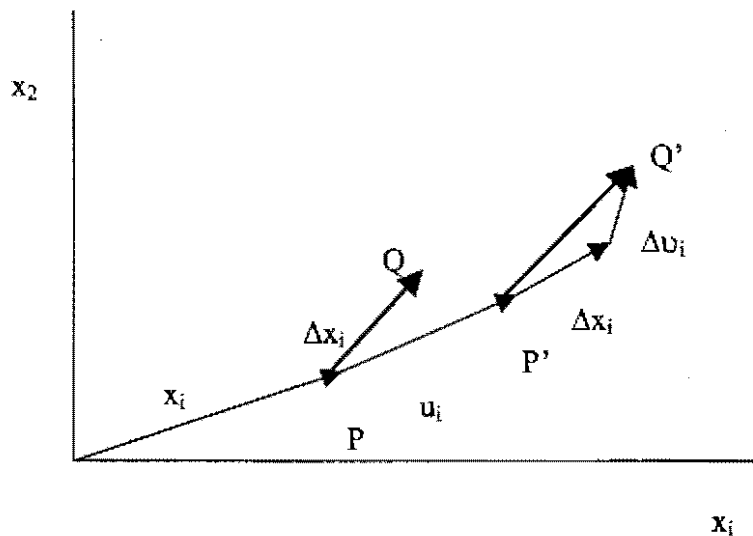
The strain *at* the point P is defined as:

$$e = \lim_{\Delta x \rightarrow 0} \frac{\Delta u}{\Delta x} = \frac{du}{dx} \quad 6A.2$$

Strain at a point is therefore the rate of change of displacement with distance.

6A.2 Two-dimensional strain

In the two-dimensional case, the displacement of points in a plane is considered using the same approach as in the one-dimensional case. These will be restricted to small displacements. The relevant vectors are given in the diagram below:



Let the point P with co-ordinates (x_1, x_2) be displaced to position P' with co-ordinates $(x_1 + u_1, x_2 + u_2)$. The vector \bar{u}_i is therefore the displacement of P . To specify the strain at this point we define the following quantities:

$$e_{11} = \frac{\partial u_1}{\partial x_1}; \quad e_{12} = \frac{\partial u_1}{\partial x_2}; \quad e_{21} = \frac{\partial u_2}{\partial x_1}; \quad e_{22} = \frac{\partial u_2}{\partial x_2}. \quad 6A.3$$

These can be written collectively as:

$$e_{ij} = \frac{\partial u_i}{\partial x_j} \quad (i, j = 1, 2) \quad 6A.4$$

The geometrical meaning of these quantities is seen by considering a point Q close to P such that $PQ = \Delta x_i$. After deformation Q moves to Q' so that $P'Q'$ is given by $\Delta \bar{x}_i + \Delta \bar{u}_i$. The vector $\Delta \bar{u}_i$ is the difference in the displacement between the two points P and Q originally separated by $\Delta \bar{x}_i$. Since the components of $\Delta \bar{u}_i$ are a function of position one can write:

$$\Delta u_1 = \frac{\partial u_1}{\partial x_1} \Delta x_1 + \frac{\partial u_1}{\partial x_2} \Delta x_2 \quad 6A.5$$

$$\Delta u_2 = \frac{\partial u_2}{\partial x_1} \Delta x_1 + \frac{\partial u_2}{\partial x_2} \Delta x_2 \quad 6A.6$$

or briefly,

$$\Delta u_i = \frac{\partial u_i}{\partial x_j} \Delta x_j = e_{ij} \Delta x_j \quad 6A.7$$

Since $\Delta \bar{u}_i$ and $\Delta \bar{x}_i$ are vectors e_{ij} must be a tensor. This tensor must describe the strain at a point P when there is a distortion of the plane and its components should vanish if there is no distortion. This is however not the case for a simple rotation of the plane so a correction must be made. If the tensor is written as the sum of its symmetrical and asymmetrical parts it can be shown that the symmetrical tensor describes a distortion and the asymmetrical tensor describes a pure rotation. Thus we write:

$$e_{ij} = \varepsilon_{ij} + \varpi_{ij} \quad 6A.8$$

where

$$\varepsilon_{ij} = \frac{1}{2}(e_{ij} + e_{ji}) \text{ and } \varpi_{ij} = \frac{1}{2}(e_{ij} - e_{ji}).$$

We therefore define the symmetrical part of e_{ij} , that is ε_{ij} as the strain. Thus in full:

$$\begin{bmatrix} \varepsilon_{11} & \varepsilon_{12} \\ \varepsilon_{21} & \varepsilon_{22} \end{bmatrix} = \begin{bmatrix} e_{11} & \frac{1}{2}(e_{12} + e_{21}) \\ \frac{1}{2}(e_{12} + e_{21}) & e_{22} \end{bmatrix} \quad 6A.9$$

6A.3 Three-dimensional strain

The same arguments are extended to three dimensions so that the variation of the displacement u_i with position x_i in the body is used to define a tensor with nine components as follows:

$$e_{ij} = \frac{\partial u_i}{\partial x_j} \quad (i, j = 1, 2, 3) \quad 6A.10$$

As was the case for two dimensions, this tensor can be split into symmetrical and asymmetrical parts which describe the extensions per unit length (i.e. the strain) and rotations of the body about the principal axes. The strain tensor is then given by:

$$\varepsilon_{ij} = \frac{1}{2}(e_{ij} + e_{ji}), \quad 6A.11$$

or in full,

$$\begin{bmatrix} \varepsilon_{11} & \varepsilon_{12} & \varepsilon_{13} \\ \varepsilon_{21} & \varepsilon_{22} & \varepsilon_{23} \\ \varepsilon_{31} & \varepsilon_{32} & \varepsilon_{33} \end{bmatrix} = \begin{bmatrix} e_{11} & \frac{1}{2}(e_{12} + e_{21}) & \frac{1}{2}(e_{13} + e_{31}) \\ \frac{1}{2}(e_{12} + e_{21}) & e_{22} & \frac{1}{2}(e_{23} + e_{32}) \\ \frac{1}{2}(e_{13} + e_{31}) & \frac{1}{2}(e_{23} + e_{32}) & e_{33} \end{bmatrix} \quad 6A.12$$

The diagonal components are the tensile strain and the off diagonal components are the shear strain.

Chapter 7

Dynamic Nuclear Polarisation of Diamond: Solid State and Thermal Mixing Effects



7.1 Theory.....	139
7.1.1 Background Theory of Dynamic Nuclear Polarisation	140
7.1.2 The Solid State Effect.....	143
7.1.3 Thermal Mixing Effect	145
7.1.4 Time Dependence of the Nuclear Polarisation.....	148
7.1.5 Nuclear Relaxation Times and Signal Enhancement	153
7.2 Results	158

7.2.1 Microwave Field (H_1) at X-Band.....	158
7.2.2 Microwave Field (H_1) at S-Band.....	159
7.2.3 The Line Shape Function $g(\omega)$	163
7.2.4 Signal Enhancement and Polarisation Rate as a Function of Field Offset from Resonance.....	165
7.2.5 Dependence of the Polarisation Rate on Impurity Concentration.....	171
7.2.6 Nuclear Signal Enhancement for DNP of Central and Hyperfine lines	173
7.3 Discussion.....	175
7.4 References.....	177

7.1 Theory

An investigation into some aspects of the Nuclear Magnetic Resonance (NMR) of diamond revealed that the ^{13}C spin-lattice relaxation rate is exceedingly slow, i.e. running to tens of hours in some cases [7.1]. This fact necessitated the development of a method or methods of accelerating the polarisation of diamond. Various techniques, such as sonically induced relaxation were investigated, but the most effective methods are collectively known as Dynamic Nuclear Polarisation (DNP). The application of the DNP techniques to diamond is the subject of this chapter. The methods discussed here are referred to as the thermal mixing effect, the solid state effect and nuclear orientation via electron-spin locking or NOVEL. The former two effects require continuous microwave radiation for optimum efficiency and the latter, which is discussed in chapter 8, requires pulsed microwave radiation. All these techniques exploit the fact that in diamond, thermal equilibrium is attained much faster in the paramagnetic impurity spin system compared to the ^{13}C nuclear spin system. In terms of heat reservoirs, the paramagnetic impurity reservoir cools much faster than the ^{13}C reservoir, to the lattice temperature. In the DNP processes contact between these and other reservoirs is facilitated and provides a path for the ^{13}C reservoir to cool. This results in a much faster polarisation of nuclei than in a ^{13}C Zeeman polarisation experiment.

In this investigation a suite of seven natural type Ia and Ib diamonds was investigated to determine their response to the various DNP techniques. The dominant DNP process depends on the paramagnetic impurity type and concentration and this suite of diamonds was selected to allow a thorough investigation of each process. The diamond type and paramagnetic impurity concentration were determined by a method developed during this study, which was discussed in chapter 5. The background theory relating to the continuous wave techniques are discussed in the following sections, followed by the experimental results and a discussion of these results.

7.1.1 Background Theory of Dynamic Nuclear Polarisation

Many elaborate treatments of the theory of DNP have been published [7.2 - 7.6] and will not be duplicated here. The salient features of this theory are however given.

The Hamiltonian of a system of interacting electron and nuclear spins can be written as [7.7]:

$$H = -\omega_e S_z - \omega_n I_z + H_{ee} + H_{en} + H_{nn}. \quad 7.1$$

The first two terms in equation 7.1 represent the Zeeman interactions of the electrons and nuclei, respectively. The electronic and nuclear spins are given by:

$$S_z = \sum_{j=1}^{N_e} S_z^j \quad \text{and} \quad I_z = \sum_{i=1}^{N_n} I_z^i, \quad 7.2$$

where N_e is the number of unpaired electrons and N_n the number of nuclei.

The frequencies $\omega_e = \gamma_e H_0$ and $\omega_n = \gamma_n H_0$ are the resonant or Larmor frequencies for electrons and nuclei in a static field H_0 , respectively, and γ_e and γ_n are their gyromagnetic ratios.

The remaining three terms in equation 7.1, H_{ee} , H_{en} and H_{nn} represent the spin-spin interactions between the electrons, between electrons and nuclei and between nuclei, respectively. In a DNP experiment the interaction between electrons and nuclei is exploited, hence the term H_{en} is most important to this discussion and will be considered in more detail. In general this term is made up of an isotropic part and an anisotropic part and can be written as:

$$H_{en} = H_{en}^{iso} + H_{en}^{aniso}. \quad 7.3$$

The isotropic part is due to a finite electron spin density at the site of the nucleus and occurs when electrons are located in s -orbitals. The anisotropic part represents dipolar interactions between nuclei and electrons that are located in non-spherically symmetrical orbitals e.g. p -orbitals. H_{en}^{iso} and H_{en}^{aniso} are described by the following formulae [7.7]:

$$H_{en}^{iso} = \sum_{i,j} a_{ij} \bar{I}_i \cdot \bar{S}_j = \sum_{i,j} \frac{1}{2} a_{ij} (I_i^+ S_j^- + I_i^- S_j^+) + I_z^i S_z^j \quad 7.4$$

$$H_{en}^{aniso} = \sum_{i,j} \frac{\gamma_e \gamma_n \hbar}{r_{ij}^3} (A_{ij} + B_{ij} + C_{ij} + D_{ij} + E_{ij} + F_{ij}) \quad 7.5$$

$$A_{ij} = (1 - 3 \cos^2 \theta_{ij}) \bar{I}_z^i \bar{S}_z^j \quad 7.6a$$

$$B_{ij} = -\frac{1}{4} (1 - 3 \cos^2 \theta_{ij}) (I_i^+ S_j^- + I_i^- S_j^+) \quad 7.6b$$

$$C_{ij} = -\frac{3}{2} \sin \theta_{ij} \cos \theta_{ij} e^{-i\vartheta_{ij}} (I_z^i S_j^+ + I_z^i S_z^j) \quad 7.6c$$

$$D_{ij} = -\frac{3}{2} \sin \theta_{ij} \cos \theta_{ij} e^{-i\vartheta_{ij}} (I_z^i S_j^- + I_i^- S_z^j) \quad 7.6d$$

$$E_{ij} = -\frac{3}{4} \sin^2 \theta_{ij} e^{-i\vartheta_{ij}} I_i^+ S_j^+ \quad 7.6e$$

$$F_{ij} = -\frac{3}{4} \sin^2 \theta_{ij} e^{-i\vartheta_{ij}} I_i^- S_j^- \quad 7.6f$$

The parameters r_{ij} , θ_{ij} and ϑ_{ij} , are the polar co-ordinates of the vector connecting the position of nucleus i and the position of electron j , averaged over its orbital. Equation 7.5 is valid if H_{en}^{aniso} is cylindrically symmetrical [7.7].

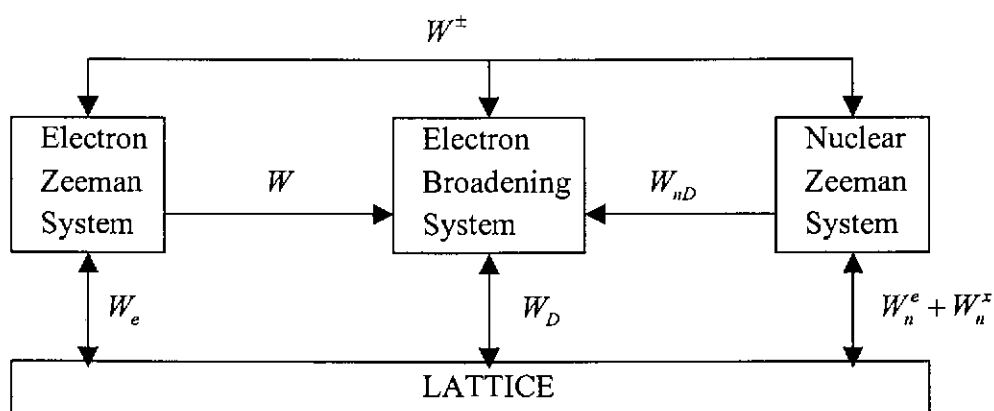
Dynamic nuclear polarisation occurs when radiation is applied at or near the electron Larmor frequency, depending on the sample. This radiation facilitates contact between the heat reservoirs mentioned above and that are shown in figure 7.1. The effectiveness of the DNP process depends on the time dependence of H_{en} as follows:

- The Overhauser effect dominates when the time dependence of H_{en} is of the order of ω_e^{-1} and the enhancement becomes maximal when $\omega = \omega_e$.
- The solid effect is dominant when the time-averaged value of H_{en}^{aniso} is non-zero. The enhancement is maximised when $\omega = \omega_e \pm \omega_n$.

- Thermal mixing occurs when the time-averaged value of H_{en}^{aniso} is non-zero and the concentration of unpaired electrons is so high that the broadening of the EPR line is homogeneous. Irradiation near ω_e enhances the polarisation corresponding to the broadening of the EPR line. Thermal mixing becomes dominant when $\omega_n \approx \omega_{\frac{1}{2}}$ and is maximised when $\omega = \omega_e \pm \omega_{\frac{1}{2}}$, where $\omega_{\frac{1}{2}}$ is the EPR line width in frequency units.

The relaxation mechanisms mentioned above are conveniently described in terms of the heat reservoirs shown in figure 7.1. In this diagram the various couplings between the respective heat reservoirs are shown. In the case of the solid effect there is direct coupling between the electron and nuclear Zeeman systems with associated transition probability W^\pm . The thermal mixing effect proceeds via the spin-spin interaction reservoir with transition probabilities of W for electrons and W_{nD} for nuclei. The transition probability W_n^x accounts for all other mechanisms that may induce transitions in the nuclear spin system.

Figure 7.1. Diagram of the heat reservoirs involved in the DNP process, the contact paths between reservoirs and the relevant transition probabilities, after Wind *et al.* [7.7].



In the following sections the solid effect and thermal mixing DNP processes are discussed in more detail. The Overhauser effect is omitted because it is not applicable to diamond.

In these discussions a number of assumption that are common to these processes are made, and are listed below:

- The magnitude of H_0 is such that the eigenstates and eigenvalues are determined by the electron and nuclear Zeeman terms.
- The temperature T is high enough for the electron polarisation to be small compared to unity.
- The time for an electron to change its spin state (electron correlation time) is much shorter than the time for a nucleus to change its spin state or for a simultaneous electron-nuclear flip.
- Only nuclei with spin $\frac{1}{2}$ are considered and γ_n is always positive.

Initially all calculations of polarisation enhancement are under the assumption that each electron only interacts with one nucleus and that all electron-nucleus interaction are identical i.e. r_{ij} , θ_{ij} and \mathcal{G}_{ij} are the same for all electron-nuclear interactions.

7.1.2 The Solid State Effect

The solid state effect occurs in solids with fixed paramagnetic impurities, where the spatial parts of H_{en}^{iso} and H_{en}^{aniso} are time independent [7.7]. The electron-nuclear states can then no longer be described by pure product functions, but are mixed with other states. Inspection of equations 7.4 to 7.6 indicates that these mixtures are due to the terms $I_i^- S_z^j$ and $I_i^+ S_z^j$. Consider an electron j in state $|-\rangle_j$, interacting with nucleus i in state $|+\rangle_i$. It follows that the term proportional to $I_i^+ S_z^j$ mixes into the state $|+\rangle_i |-\rangle_j$, a contribution $q_{ij} |+\rangle_i |+\rangle_j$ [7.7], where

$$q_{ij} = -\frac{3}{4} \frac{\gamma_e \gamma_n \hbar}{\omega_n} \frac{1}{r_{ij}^3} \sin \theta_{ij} \cos \theta_{ij} e^{-i\theta_{ij}}. \quad 7.7$$

Similar mixtures are obtained for states $|+\rangle_i |+\rangle_j$, $|-\rangle_i |+\rangle_j$ and $|-\rangle_i |-\rangle_j$, hence irradiating at a frequency $\omega = \omega_e \pm \omega_n$ leads to induced transitions with a transition probability W^\pm where a nucleus and an electron flips simultaneously, the so-called forbidden transition. W^\pm is given by [7.6]:

$$W^\pm = 4|q_{ij}|^2 \left[\frac{1}{2} \pi \gamma_e^2 H_1^2 g((\omega - \omega_e) \pm \omega_n) \right]. \quad 7.8$$

Averaging over θ gives:

$$4|q_{ij}|^2 = \frac{3}{10} \frac{\gamma_e^2 \hbar^2}{H_0^2} \frac{1}{r_{e-n}^6} \quad 7.9$$

and simplifying yields:

$$W^\pm = \frac{\Gamma^\pm}{r_{e-n}^6} = \frac{3\pi}{20} \left(\frac{H_1}{H_0} \right)^2 \frac{1}{r_{e-n}^6} \gamma_e^4 \hbar^2 g[(\omega - \omega_e) \pm \omega_n], \quad 7.10$$

where $g(\omega)$ is the EPR line shape function. This transition probability is small compared to the electron Zeeman transition probability.

Without microwave radiation, the transition probability W_n^e that describes the nuclear relaxation caused by an electron-nuclear interaction is given by [7.6]:

$$W_n^e = 4|q_{ij}|^2 \frac{\omega_n^2 T_{1e}}{1 + \omega_n^2 T_{1e}^2}. \quad 7.11$$

Averaging over θ and simplifying yield:

$$W_n^e = \frac{C}{r_{e-n}^6} = \frac{3}{10} \frac{1}{r_{e-n}^6} \frac{\gamma_e^2 \hbar^2}{T_{2e} H_0^2}. \quad 7.12$$

Inspection of equations 7.10 and 7.12 reveals that neither are dependent on the orientation of vector r_{e-n} . The solid effect is therefore independent of the spatial distribution of nuclei around an electron, or in other words, independent of the orientation of the sample.

These transition probabilities W^+ (flip-flop) and W^- (flip-flip) are most effective when $\omega = \omega_e \pm \omega_n$. If, however, the EPR line width is of the order of ω_n , flip-flop and flip-flip transitions occur simultaneously. This is then referred to as the unresolved solid state effect.

7.1.3 Thermal Mixing Effect

The thermal mixing effect can also be present in solids with fixed paramagnetic centres. This effect occurs in solids where the EPR line width becomes comparable to the nuclear Larmor frequency ω_n and coupling of the two spin systems is due to the broadening of the EPR system [7.7]. Irradiating near the electron Larmor frequency can then enhance the nuclear polarisation. To explain this effect, consider the electron spin system in isolation and assume that the broadening of the EPR line is due to electron-electron interactions only. Assume also that the electron-electron interactions are so large that the EPR line is homogeneously broadened. The local fields due to nuclei and other electrons then dictates the ordering of the electron spins and can be characterised by a spin temperature T_{SS} . Similarly, the spin temperature due to the application of the external static field H_0 is defined as T_Z . Both T_{SS} and T_Z are equal to the lattice temperature T_L at

equilibrium. Irradiation of the sample at a frequency ω can alter these temperatures. When the irradiation is applied, a photon of energy $\hbar\omega$ is made available; part of the energy, $\hbar\omega_e$ is absorbed by the electron Zeeman system and the remainder, i.e. $\hbar(\omega - \omega_e)$ is either absorbed (for $\omega_e < \omega$), or emitted (for $\omega_e > \omega$) by the broadening system or spin-spin interaction reservoir.

This is in essence similar to the solid effect where the forbidden transitions are stimulated and an energy quantum $\hbar\omega_e$ is absorbed by the electron Zeeman system. At the same time, energy quanta $\hbar\omega_n$ are either emitted or absorbed in the nuclear Zeeman system. In the case of thermal mixing, allowed transitions are stimulated and the induced polarisation is via the electron broadening system. The transition probability of such a transition is [7.7]:

$$W = \pi\gamma_e^2 H_1^2 g(\omega - \omega_e). \quad 7.13$$

Relaxation in the nuclear system is obtained as follows. When $\omega_e \approx \omega_n$ there may also be contact between the nuclear Zeeman reservoir and the electron broadening system. This transition probability is characterised by the contact time τ_{ne} , between the nuclear Zeeman and the spin-spin interaction (or electron broadening) reservoirs as given below [7.7]:

$$\frac{1}{\tau_{ne}} = 4|q_{ij}|^2 \frac{\omega_n^2 T_{2e}^{SS}}{1 + \omega_n^2 (T_{2e}^{SS})^2}. \quad 7.14$$

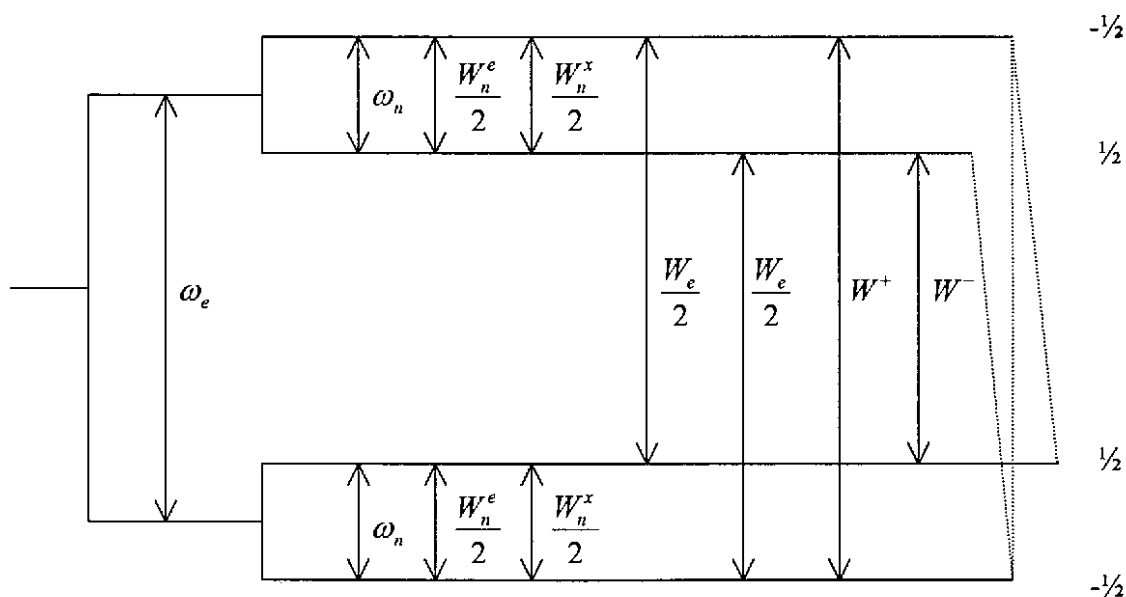
Again averaging over θ and simplifying gives a transition probability [7.7]:

$$W_{nD} = \frac{K}{r_{e-n}^6} = \frac{3}{10} \frac{1}{\omega_n^2} \gamma_n^2 \gamma_e^2 \hbar^2 \frac{1}{T_{2e}^{SS}} \frac{1}{g(0)} \int_{-\infty}^{\infty} g(\omega) g(\omega - \omega_n) d\omega, \quad 7.15$$

where T_{2e}^{SS} is the spin-spin interaction relaxation time and the integral takes into account that the electrons performing a flip-flop transition have to differ by ω_n in their Larmor frequencies in order to provide the energy quanta $\hbar\omega_n$ necessary to change the nuclear polarisation [7.7].

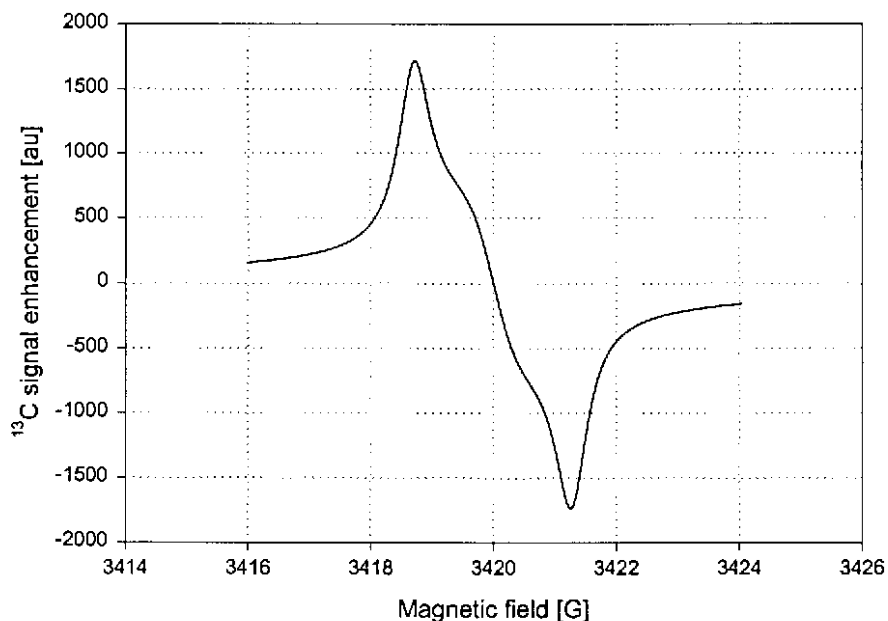
A diagram showing the energy levels and the transition probabilities, for all of the transitions discussed, is shown in figure 7.2.

Figure 7.2. Transitions and their relevant transition probabilities between energy levels in diamond.



The dependence of the signal enhancement on the field (or frequency) when the solid and thermal mixing effects are applied, is shown in figure 7.3.

Figure 7.3. Nuclear signal enhancement as a function of offset field.



7.1.4 Time Dependence of the Nuclear Polarisation

The polarisation induced in the nuclear spin system by any of the above DNP techniques is proportional to r^{-6} and are therefore only effective over relatively short ranges. The distance between a paramagnetic impurity electrons and nuclei participating in the DNP process is therefore important. This distance is obtained using a Poisson distribution and setting the probability of finding no particles between two particles i and j separated by a distance r_{i-j} equal to $\frac{1}{2}$ [7.8], i.e.:

$$\exp\left(-\left[\frac{4}{3\pi}N_j r_{i-j}^3\right]\right) = \frac{1}{2}. \quad 7.16$$

Solving this equation yields:

$$r_{i-j} = 0.55N_j^{-\frac{1}{3}}. \quad 7.17$$

Nuclei within a sphere defined by this radius will experience local fields that are dependent on their distance from a paramagnetic centre at the centre of the sphere. Nuclei can be classified into three zones depending on this distance as follows:

1. Very close to a paramagnetic centre, nuclei are strongly influenced by the electron where local fields vary too much for normal flip-flop transitions and spin diffusion to take place [7.9]. The nuclear magnetic resonance frequencies of these nuclei are shifted into the wings of the NMR line and are therefore not visible. These nuclei fall into a sphere whose radius δ , for $T_{2e} < T_{2n}$ and $\hbar\gamma_e H_0 < 2kT$, is defined as:

$$\delta = \left(\frac{\gamma_e \hbar\gamma_e H_0}{\gamma_n 2kT}\right)^{0.3} r_{e-n}. \quad 7.18$$

2. The distance from the paramagnetic centre where direct polarisation of nuclei by the electron occurs, is given by [7.7]:

$$b = 0.68\left(\frac{\Gamma}{D}\right)^{\frac{1}{4}}, \quad 7.19$$

where D is the diffusion constant that is given by:

$$D = \frac{r_{n-n}^2}{50T_{2n}}. \quad 7.20$$

Therefore, nuclei at distances $b > r > \delta$ from the paramagnetic electron, will be polarised directly.

3. The nuclei within the shell $r_{e-e} > r > b$ are polarised by spin diffusion.

These zones are shown in the figure 7.4 and we define:

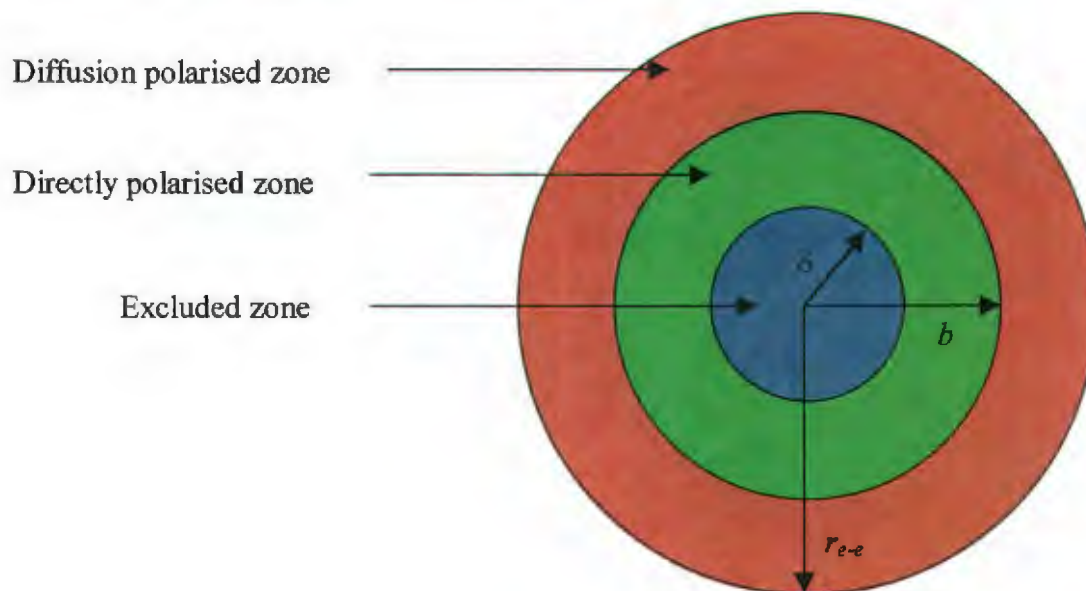
$$N_{direct} = \frac{b^3 - \delta^3}{r_{e-e}^3} N_{Total}. \quad 7.21$$

$$N_{Diff} = \frac{r_{e-e}^3 - b^3}{r_{e-e}^3} N_{Total}. \quad 7.22$$

$$N_{excl} = \frac{\delta^3}{r_{e-e}^3} N_{Total}, \quad 7.23$$

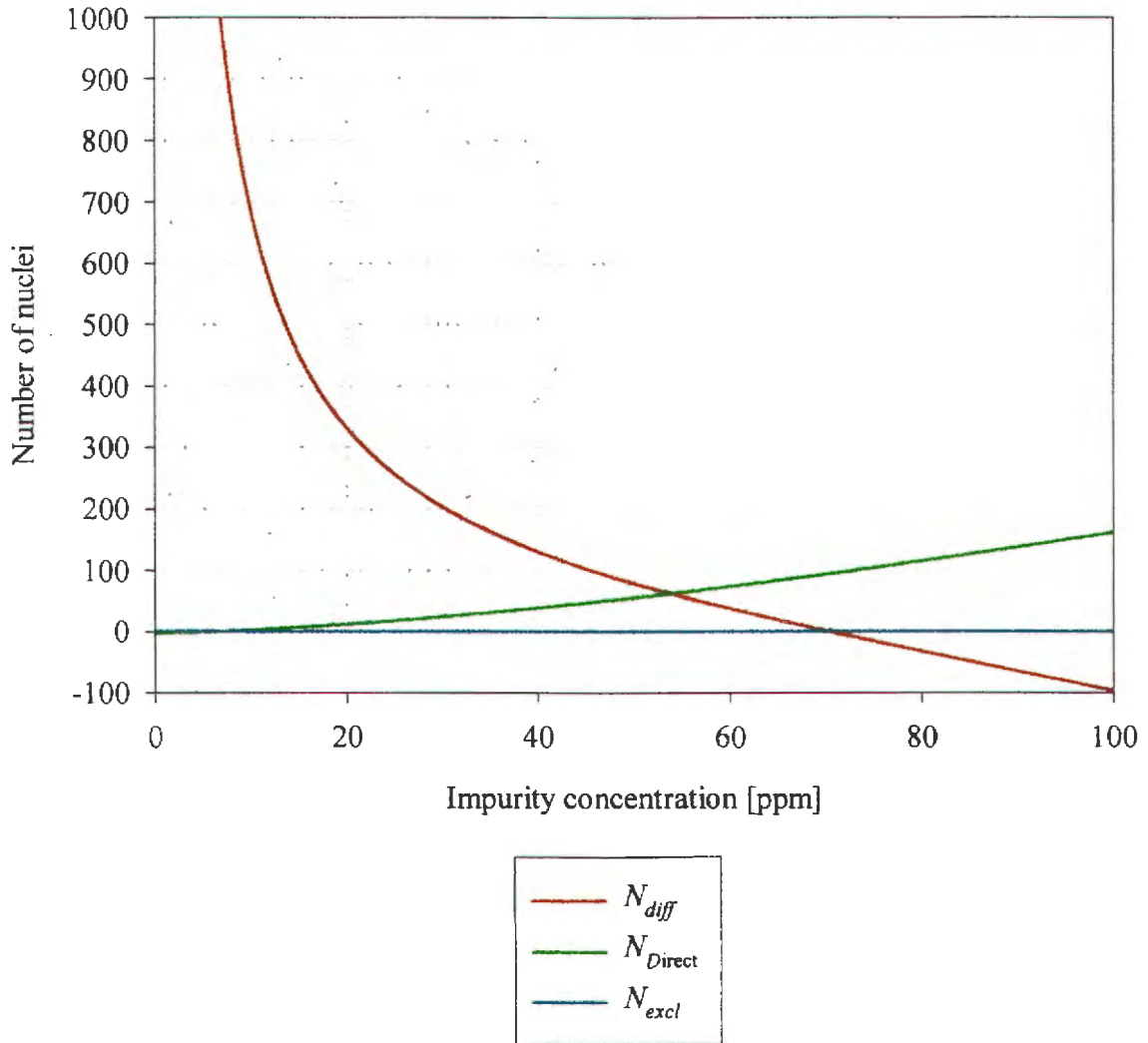
where N_{Direct} , N_{Diff} and N_{Excl} are the number of nuclei which are relaxed directly, by diffusion and those that are excluded from the relaxation process, respectively. N_{Total} is the total number of nuclei in the sphere of radius r_{e-e} .

Figure 7.4. Polarisation zones where spins are excluded, polarised directly and polarised by spin diffusion.



Substituting equation 7.17 into equations 7.21 – 7.23 and plotting the number of nuclei polarised directly, by diffusion and those excluded, as a function of the paramagnetic impurity concentrations, some interesting information is revealed and is shown in figure 7.5.

Figure 7.5. The dependence of N_{Diff} , N_{Direct} and N_{Excl} on paramagnetic impurity concentration.



In diamond, the total number of nuclei in a sphere of radius r_{e-e} is $N_{Total} = 3.7 \times 10^{21} r_{e-e}^3$ [7.10]. Using this and other relevant information for diamond, the following trends are observed:

1. N_{Direct} and N_{Diff} are dependent on the paramagnetic impurity concentration C_e .
2. For $C_e < 10$ ppm, excluding those within the sphere of radius δ , almost all the nuclei are polarised by spin diffusion.
3. For $10 < C_e < 70$ ppm the number of nuclei polarised by spin diffusion decreases rapidly and the number polarised directly increases. At about 55 ppm $N_{Diff} \approx N_{Direct}$. Increasing the static field H_0 , will move this intersection point to higher concentrations.
4. For $C_e > 70$ ppm all nuclei are relaxed directly. N_{Direct} does not however increase as sharply as N_{Diff} decreased due to the fact that the excluded zone becomes more significant at higher concentrations. This can be noted from the following equations:

$$N_{Diff} \approx N_{Total} \text{ for } C_e < 10 \text{ ppm} \quad 7.24$$

$$N_{Direct} \approx N_{Total} - N_{Excl} \text{ for } C_e > 70 \text{ ppm.} \quad 7.25$$

From the foregoing it can be concluded that the ^{13}C spin-lattice relaxation rate is a function of the impurity concentration and the spin diffusion constant.

7.1.5 Nuclear Relaxation Times and Signal Enhancement

Spin-lattice relaxation times and the possible signal enhancement depend on the distances defined above or, in other words, on the paramagnetic impurity concentration in the following way. Following the approach used in [7.11], if:

$$\delta < \left(\frac{C + K + \Gamma^+ + \Gamma^-}{D} \right)^{\frac{1}{4}} < r_{e-e}, \quad 7.26$$

the nuclei are polarised directly and the spin-lattice relaxation rate for solid and thermal mixing effects is given by [7.7]:

$$\frac{1}{T_1^*} = \frac{8\pi}{3} N_e D^{\frac{3}{2}} (C + K + \Gamma^+ + \Gamma^-)^{\frac{1}{2}}, \quad 7.27$$

where D was defined in equation 7.20. The time dependence of the ^{13}C magnetisation is given by [7.7]:

$$M = M_0 + [M_{0z} - M_0] \exp\left(-\frac{\tau}{T_1^*}\right), \quad 7.28$$

where

$$M_0 = \frac{T_1^{-1} + 4\pi D N \bar{F} (C + \Gamma^+ + \Gamma^-)^{-1} \left[T_1^{-1} + \frac{\gamma_e}{\gamma_n} (\Gamma^+ + \Gamma^-) \right]}{T_1^{-1} + 4\pi D N \bar{F}} M_{0z}, \quad 7.29$$

and \bar{F} is a constant. T_1 and M_{0z} are the Zeeman ^{13}C relaxation time and equilibrium magnetisation at the same field, in the absence of the microwave radiation. Under DNP conditions, $M_0 \gg M_{0z}$ and $T_1^* \ll 4\pi N D N \bar{F}$. If $\Delta > H_L$ then:

$$M_0 \approx \frac{C + \frac{\gamma_e}{\gamma_n} \Gamma^-}{C + \Gamma^-} M_{0z}. \quad 7.30$$

The enhancement of the nuclear signal is then given by [7.7]:

$$\eta_n = -Q \frac{[W^+ - W^-]T_1^+ - [W^+ + W^- + W_{nD}]T_1^+ WT_{1e} \left(\frac{\Delta\gamma_n H_0}{a\gamma H_L^2} \right)}{\left[1 + W^+ T_1^+ + W^- T_1^+ + W_{nD} T_1^+ \right] \left[1 + WT_{1e} \left(\frac{\Delta^2}{aH_L^2} + 1 \right) \right]}, \quad 7.31$$

with

$$Q = \frac{\gamma_e}{\gamma_n} \left(\frac{T_1^+}{T_1^+ + T_{1e}} \right), \quad 7.32$$

$$a = \frac{T_{1e}}{T_{1D}} \quad (T_{1D} \text{ is the electron dipolar relaxation time}), \quad 7.33$$

$$T_1 = \frac{8\pi}{3} N_e C^{\frac{1}{4}} D^{\frac{3}{4}}. \quad 7.34$$

Calculated nuclear signal enhancements as a function of H_1 at two impurity concentrations, 20 ppm and 0.1 ppm, are shown in figures 7.6a and 7.6b.

Figure 7.6a. Calculated dependence of the ^{13}C signal enhancement on H_1 for $C_e = 20$ ppm.

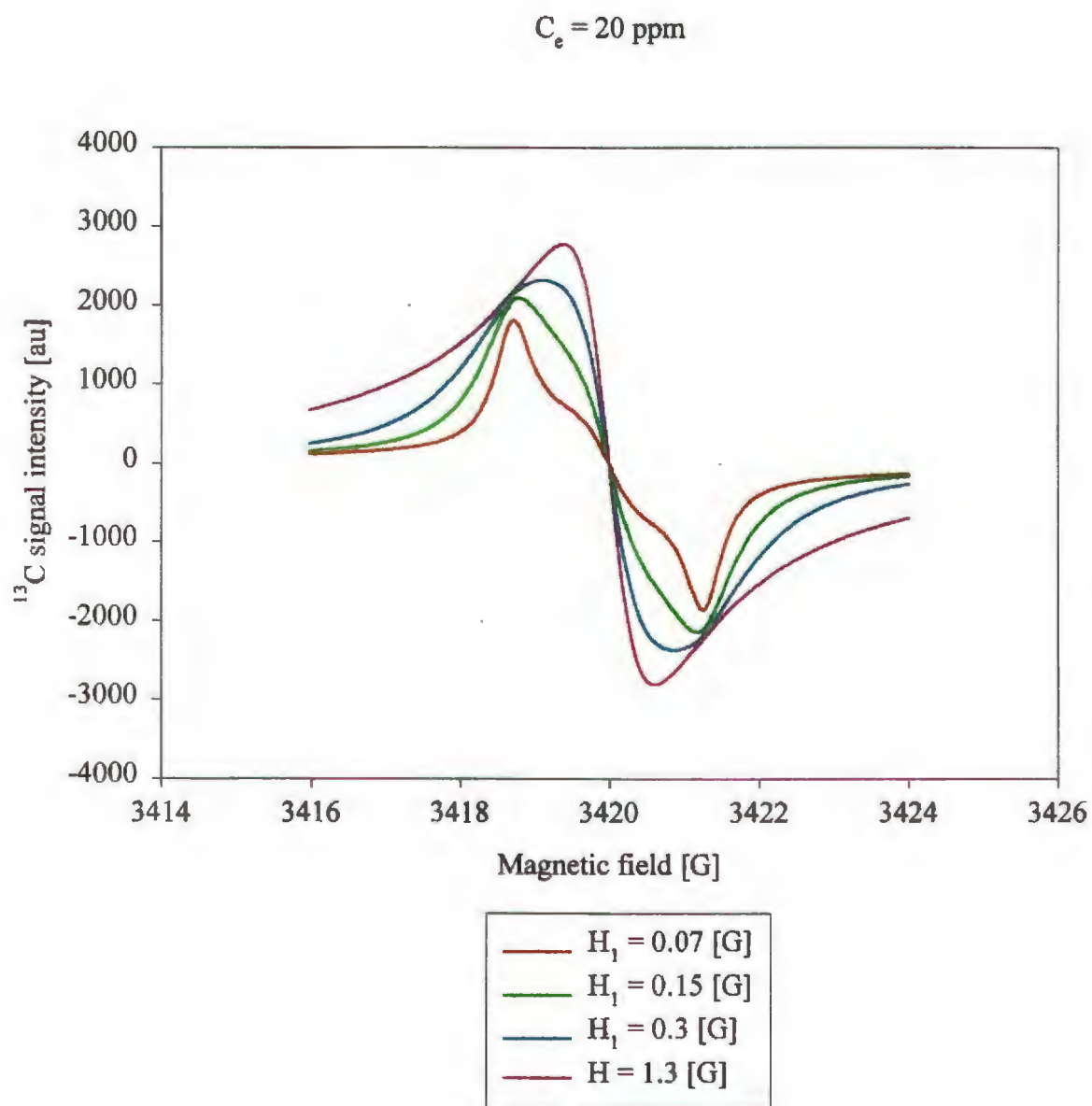
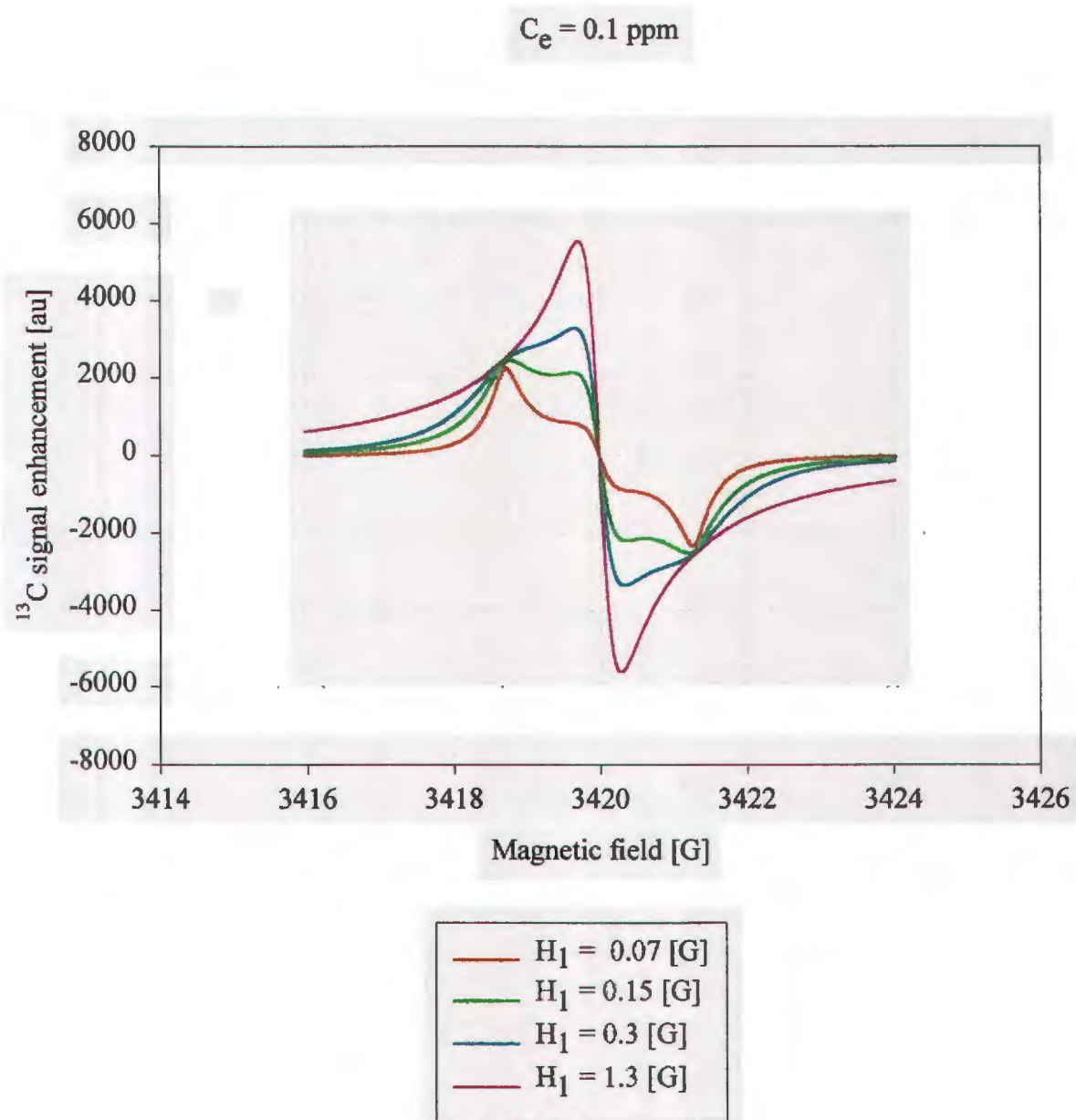


Figure 7.6b. Calculated dependence of the ^{13}C signal enhancement on H_1 for $C_e = 0.1$ ppm.



The thermal mixing process dominates if $H_1 > 0.1\text{G}$ at both s-band and x-band. At s-band, however, H_L/H_F (where H_F is the field offset from resonance) is larger than at x-band and thermal mixing is more prevalent. It is interesting to note that at high H_1 values and low impurity concentrations the nuclear signal enhancement exceeds the theoretical maximum of γ_e/γ_n . This can be seen from equation 7.31, where the thermal mixing signal enhancement is given by:

$$\eta_{TM} = Q \frac{\left[\langle W^+ \rangle + \langle W^- \rangle + \langle W_{nD} \rangle \right] T_1^+ W T_{1e} \left(\frac{\Delta \gamma_n H_0}{a \gamma_e H_L^2} \right)}{\left[1 + \langle W^+ \rangle T_1^+ + \langle W^- \rangle T_1^+ + \langle W_{nD} \rangle T_1^+ \right] \left[1 + W T_{1e} \left(\frac{\Delta^2}{a H_L^2} + 1 \right) \right]} \quad 7.35$$

For $\Delta^2 = a H_L^2$ and $W \gg T_{1e}$ (i.e. for high power or large H_1) and since $T_1^+ \ll T_1$, it follows that:

$$\eta_{TM} \approx \frac{1}{2} \frac{H_0}{\sqrt{a} H_L}. \quad 7.36$$

Substituting typical values (i.e. $H_0 = 3400\text{G}$, $C_e < 10\text{ppm}$ or $H_L \leq 0.25\text{G}$ and $a \approx 3$) into equation 7.36, yields:

$$\eta_{TM} \approx 4000, \quad 7.37$$

which exceeds the theoretical maximum of $\gamma_e/\gamma_n \approx 2600$.

7.2 Results

7.2.1 Microwave Field (H_1) at X-Band

The magnitude of the magnetic field component of the microwave irradiation applied in a DNP experiment is calculated as follows [7.12]:

$$H_1 = 2\mu_0 \frac{\beta a_c}{\pi} A, \quad 7.38$$

where

$$\beta = \left[\left(\frac{2\pi}{\lambda_0} \right)^2 - \left(\frac{\pi}{a_c} \right)^2 \right]^{\frac{1}{2}}, \quad 7.39$$

is the propagation constant and

$$A = \left[\frac{4\pi^2 P}{\omega_e \mu_0 a_c^3 b_c \beta} \right]^{\frac{1}{2}}. \quad 7.40$$

Here a_c , b_c and P are the dimensions on the x-band waveguide and the input power to the matched cavity, respectively.

Substituting the values, $\omega_e/2\pi = 9.6 \times 10^9$ Hz, $a_c = 2.286 \times 10^{-2}$ m, $b_c = 1.016 \times 10^{-2}$ m and $P = 220$ mW into these equations, yields a $H_1 = 0.147$ G.

7.2.2 Microwave Field (H_1) at S-Band

The nature of the s-band hardware dictated that the continuous wave DNP experiments be carried out as a long series of pulses with an interval between these pulses. The length of the pulse is τ_1 and the length of the interval is τ_2 . The time-averaged value of the solid state effect transition probability Γ^\pm , is given by [7. 9]:

$$\Gamma_{eff}^\pm = \Gamma^\pm \alpha, \quad 7.41$$

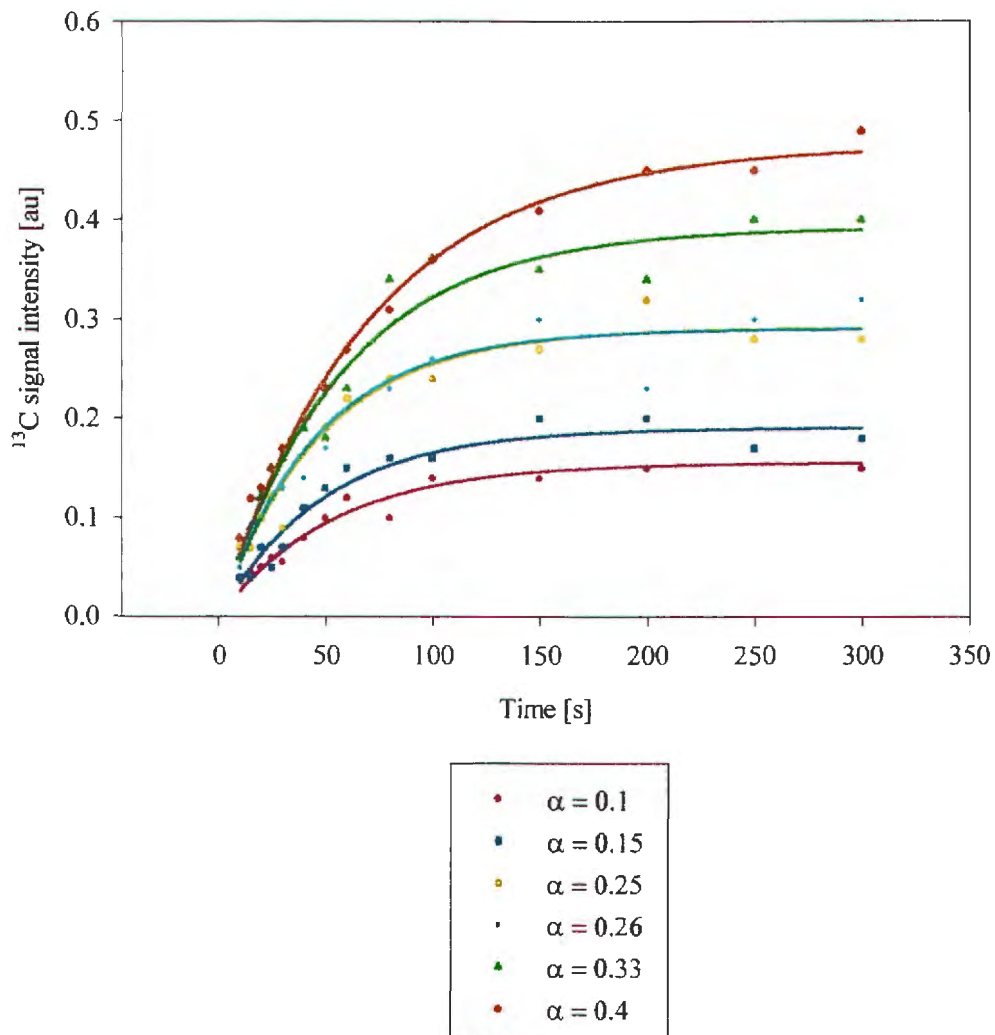
where

$$\alpha = \frac{\tau_1}{\tau_1 + \tau_2}.$$

7.42

The time dependence of the ^{13}C magnetisation for various values of α and the same microwave power is shown in figure 7.7.

Figure 7.7. Time dependence of the ^{13}C magnetisation for a few values of α for sample B2. Solid lines represent fits of equation 7.43 to the data.



The values of the saturation magnetisation M_0 and the DNP relaxation time T_1^+ are obtained from fitting the equation:

$$M = M_0 \left[1 - \exp\left(-\frac{\tau}{T_1^+}\right) \right], \quad 7.43$$

to the measured data. These values are plotted in figures 7.8 and 7.9 as a function of α . The solid line in figure 7.8 represents a fit of equation 7.30 to the data. Using the fitting parameters and equation 7.10 and 7.12, it follows that $H_1 = 0.13$ G.

The relaxation rate under these conditions is obtained by substituting equation 7.41 into equation 7.27 to yield:

$$\frac{1}{T_1^+} = \frac{3\pi}{8} N_e D^{\frac{3}{2}} (C + \alpha \Gamma_{SS}^-)^{\frac{1}{2}}. \quad 7.44$$

The transition probabilities that are not applicable to this situation have been omitted from equation 7.44. A fit of this equation to the measured data, represented by the solid line in figure 7.9, yielded $N_e = 1.3 \times 10^{18} \text{ cm}^{-3}$ or $C_e = 13$ ppm.

Figure 7.8. ^{13}C equilibrium magnetisation as a function of α . The solid line is a fit of equation 7.30 to the data with $H_I = 0.13\text{ G}$.

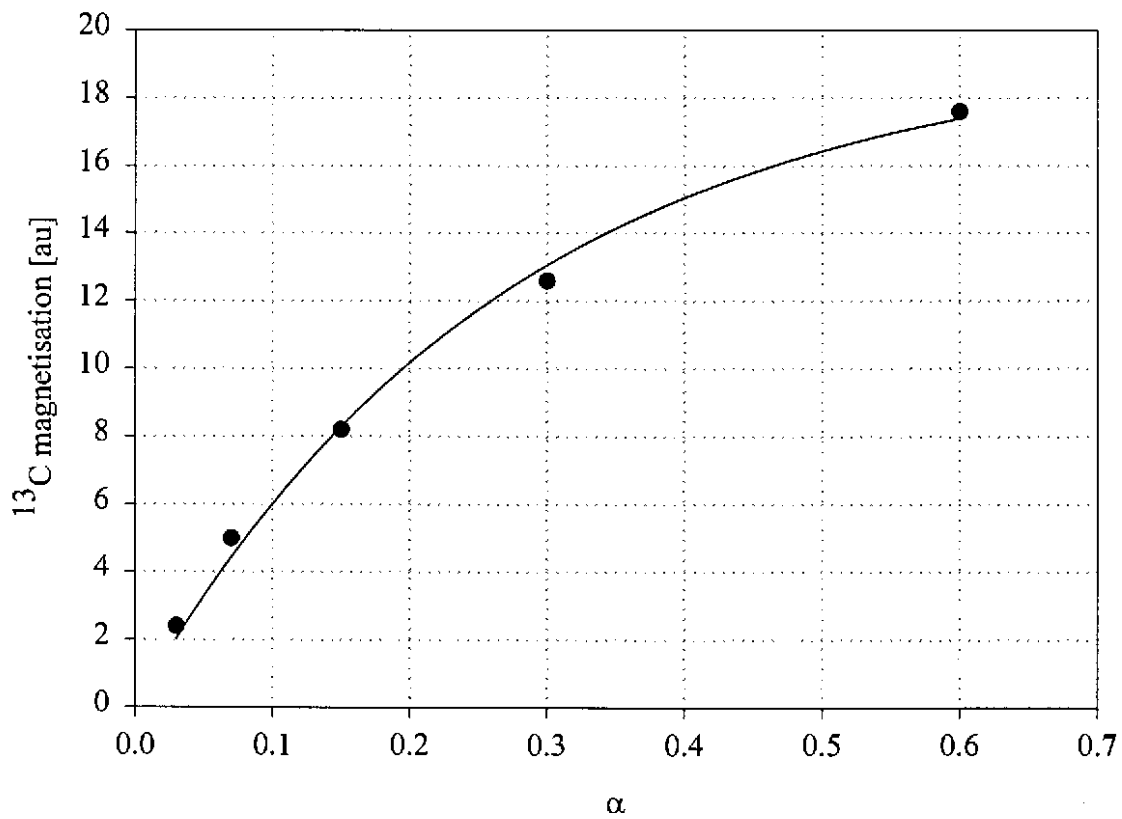
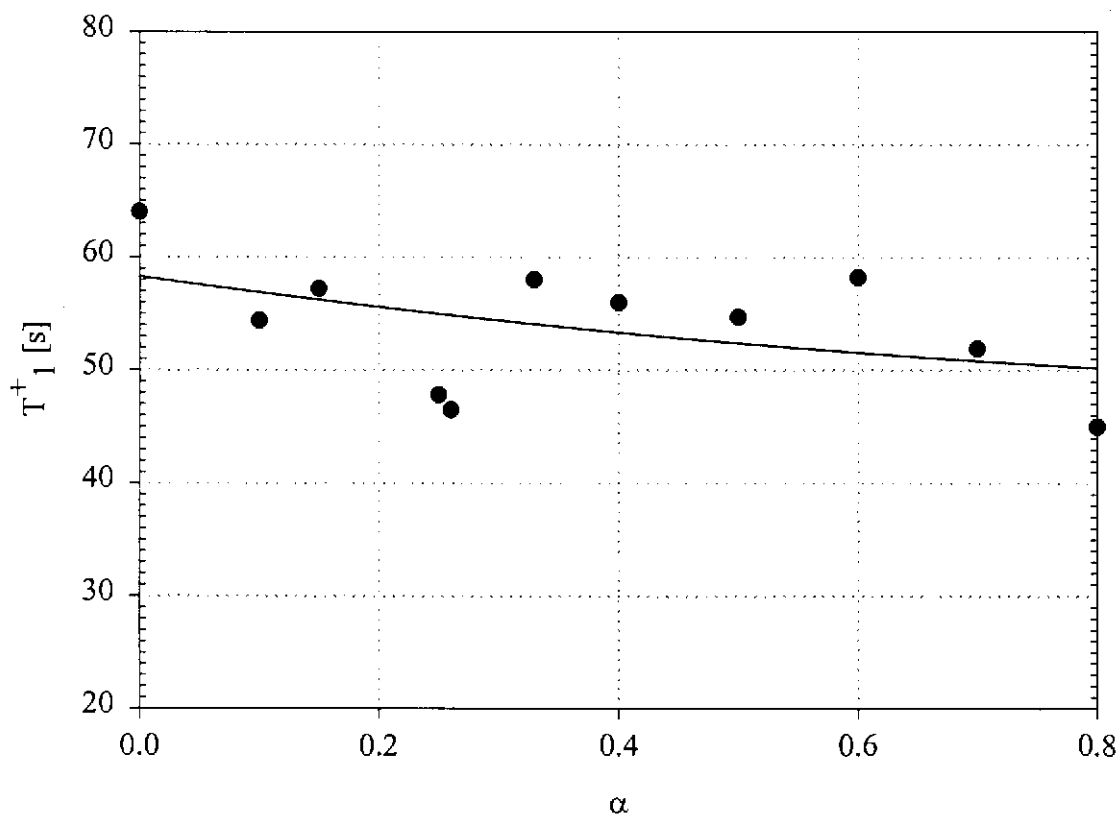


Figure 7.9. DNP ^{13}C polarisation time T_1^+ as a function of α . The solid line is a fit of equation 7.27 to the data with $C_e = 13$ ppm.



7.2.3 The Line Shape Function $g(\omega)$

The line shape function plays an important role in transition probabilities associated with relaxation processes in diamond and is required for the calculation of the theoretical signal enhancements and the relaxation rates. Details of the nature of the line shape functions encountered in magnetic resonance studies are therefore discussed here. The width and shape of resonance lines are due to processes that vary the relative energies of spin levels [7.13]. Such processes are characterised, mainly, by the spin-spin relaxation

time T_2 . The form of the line is described, in angular frequency units, by a line shape function, $g(\omega)$, that shows how the energy absorption varies near resonance. The line shape function is normalised to unit area so that [7.13]:

$$\int_0^{\infty} g(\omega) d\omega = 1. \quad 7.45$$

Magnetic resonance lines most commonly show the Lorentz line shape, which is given by [7.14]:

$$g(\omega) = \frac{\delta_l}{\pi} \frac{1}{\delta_l^2 + (\omega - \omega_0)^2}, \quad 7.46$$

where δ_l is the half width at half height and ω_0 the resonance frequency.

The next most common line shape encountered is the gaussian line shape, which is given by [7.14]:

$$g(\omega) = \frac{1}{\Delta\sqrt{2\pi}} \exp\left(-\frac{(\omega - \omega_0)^2}{2\Delta^2}\right), \quad 7.47$$

where Δ is the gaussian width that is calculated from:

$$\Delta = \frac{1}{T_2}, \quad 7.48$$

or can be obtained from the second moment of the line as follows:

$$M_2 = \Delta^2, \quad 7.49$$

or more generally:

$$M_{2n} = (2n-1)\Delta^{2n}, \quad n = 1, 2, 3, \dots \quad 7.50$$

The value used for $g(\omega)$ is obtained by assuming that the average local field at an impurity site is given by:

$$H_L \approx \sqrt{M_{2e}}, \quad 7.51$$

where M_{2e} is the second moment of the EPR line that is given in gauss² by [7.15]:

$$M_2 = (4.55 \times 10^{-5} C_e^2 + 0.0055). \quad 7.52$$

It was found that the Lorentz line shape obtained by substituting the EPR line width [7.8]:

$$\delta_l = \sqrt{1.2 \times 10^4 C_e^2 + 0.014}, \quad 7.53$$

into equation 7.47, fits the experimental EPR line shape at 9.6 GHz quite well.

7.2.4 Signal Enhancement and Polarisation Rate as a Function of Field Offset from Resonance.

The ¹³C signal enhancements for x-band and s-band were investigated and the results for sample B2 are shown in figures 7.10 and 7.11. The solid lines represent the fits of equation 7.31 to the data. The dominant DNP effects for sample B2, at each of these frequencies, are determined from an examination of the peak-to-peak line width of about 0.2 G as shown in figure 7.12. At s-band (834 G), $H_F \approx 0.32$ G and the thermal mixing effect is expected to dominate. When fitting equation 7.31, C_e and a are varied and the experimentally determined values of T_{1e} , T_{2e} and T_{2n} , given in table 7.1 are used. As can be seen in figures 7.10 and 7.11 the experimental and theoretical results agree quite well.

Figure 7.10. Signal enhancement for sample B2 as a function of DNP field at 9.6 GHz.

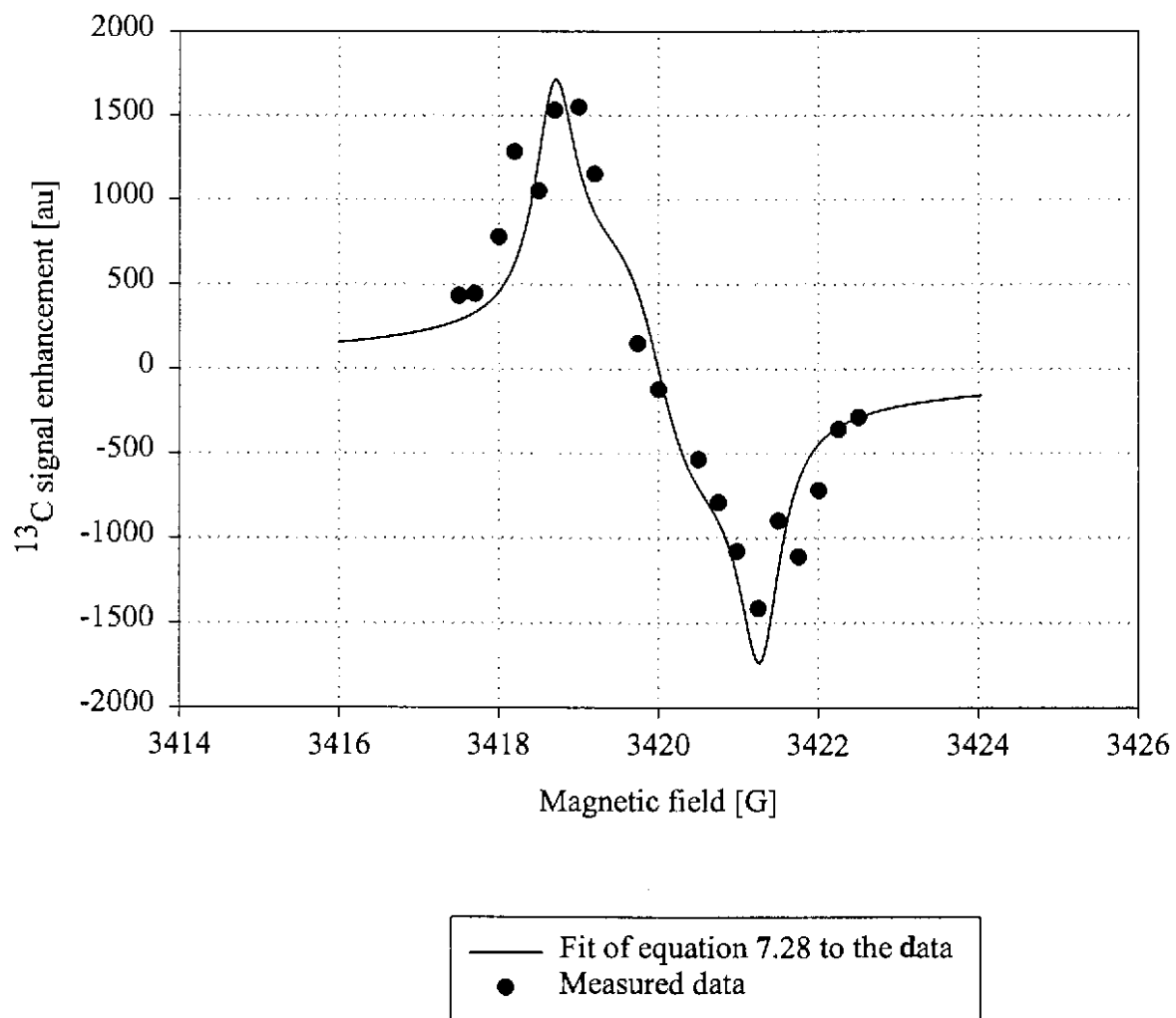
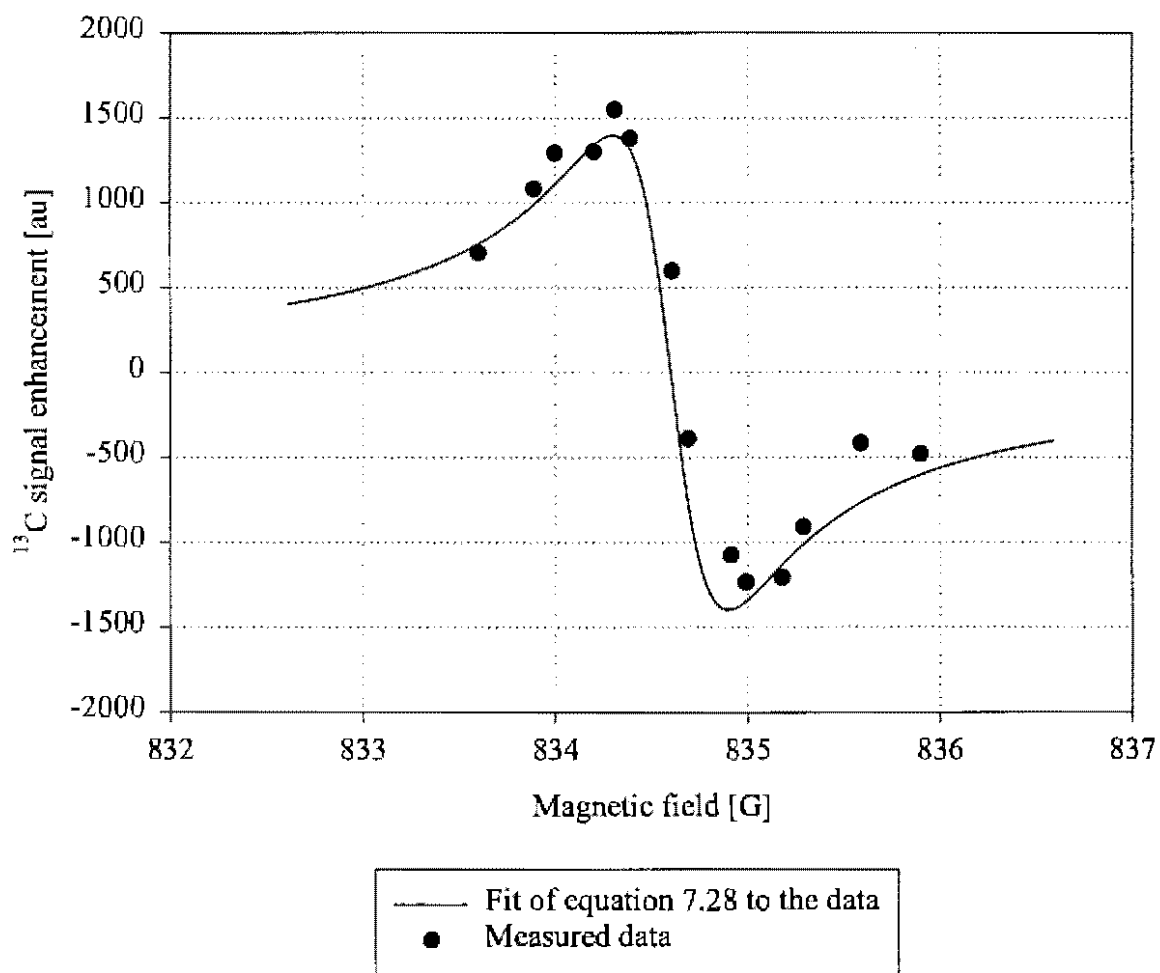


Figure 7.11. Signal enhancement for sample B2 as a function of DNP field at 2.4 GHz.



The data displayed in figures 7.10 and 7.11 were derived from the ¹³C saturation magnetisation for various H_0 values, as illustrated in figure 7.13.

Figure 7.12. Continuous wave EPR spectrum of sample B2 at 9.6 GHz. The $m_l = 0$ and $m_l = \pm 1$ transitions are indicated.

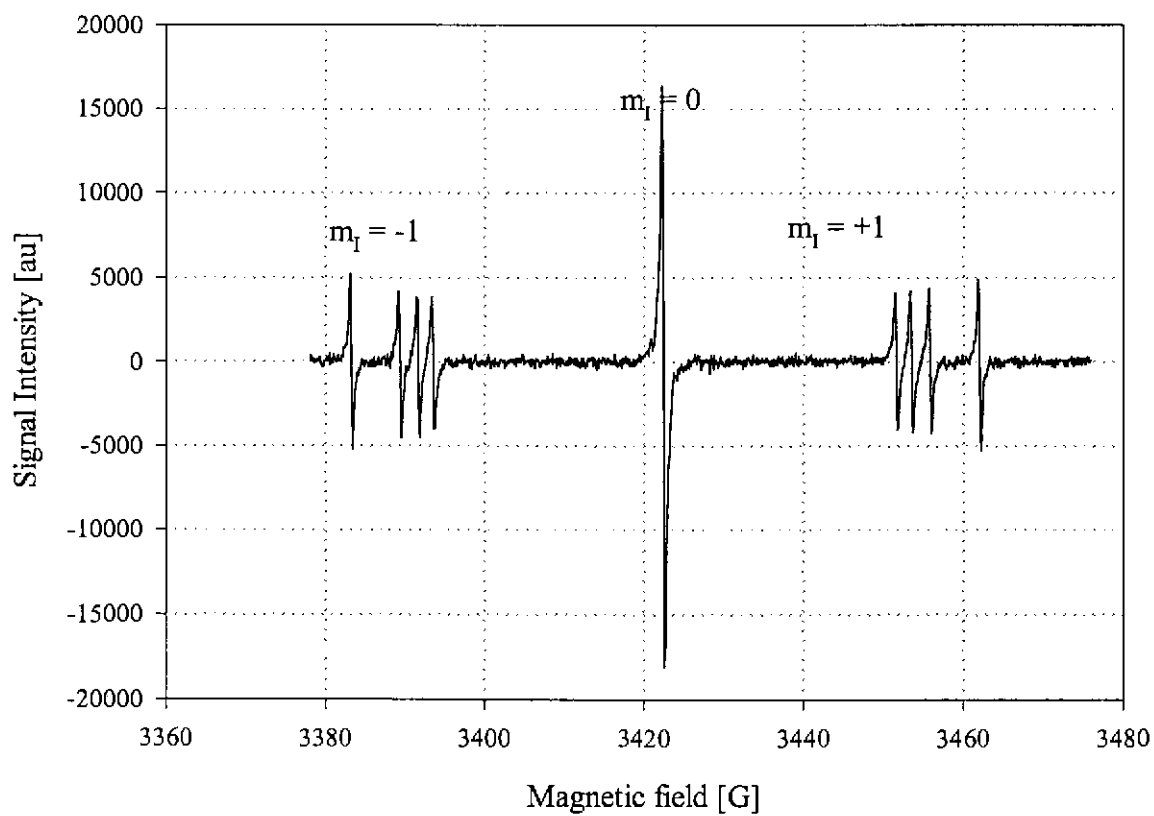
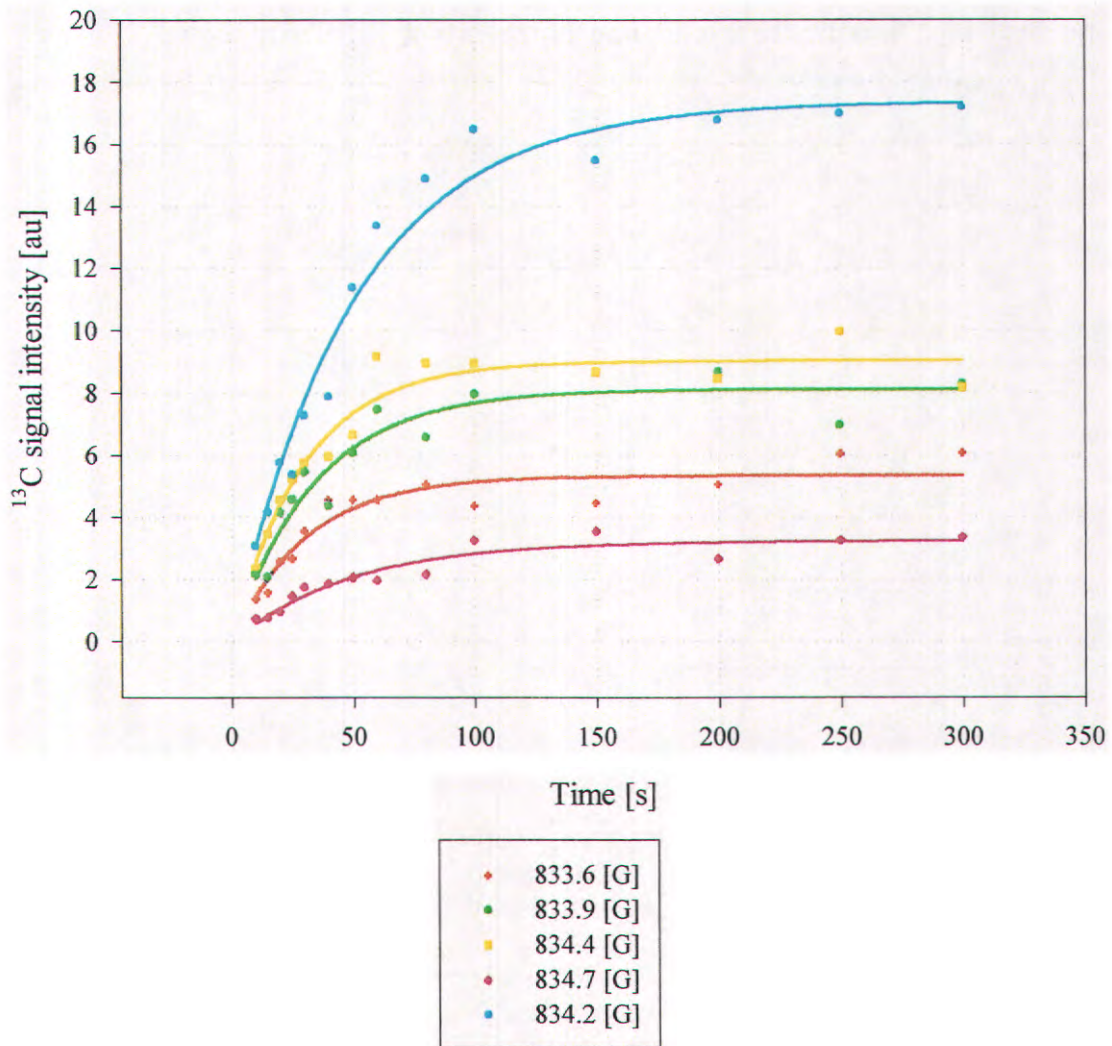


Figure 7.13. Saturation ^{13}C magnetisation for a few H_0 values.



The polarisation time, T_1^+ , is plotted in figure 7.14. The solid state, thermal mixing, Zeeman and total polarisation rates are shown in this figure. A reasonable agreement between theory and experiment with $C_e = 13$ ppm and $H_1 = 0.15$ G is obtained, if the difficulty of making these measurements is taken into account.

Figure 7.14. ^{13}C spin-lattice relaxation time, T_1^+ , of sample B2 as a function of DNP magnetic field at 2.4 GHz. The solid line represents a fit of equation 7.27 with $C_e = 13$ ppm and $H_1 = 0.15$ G.

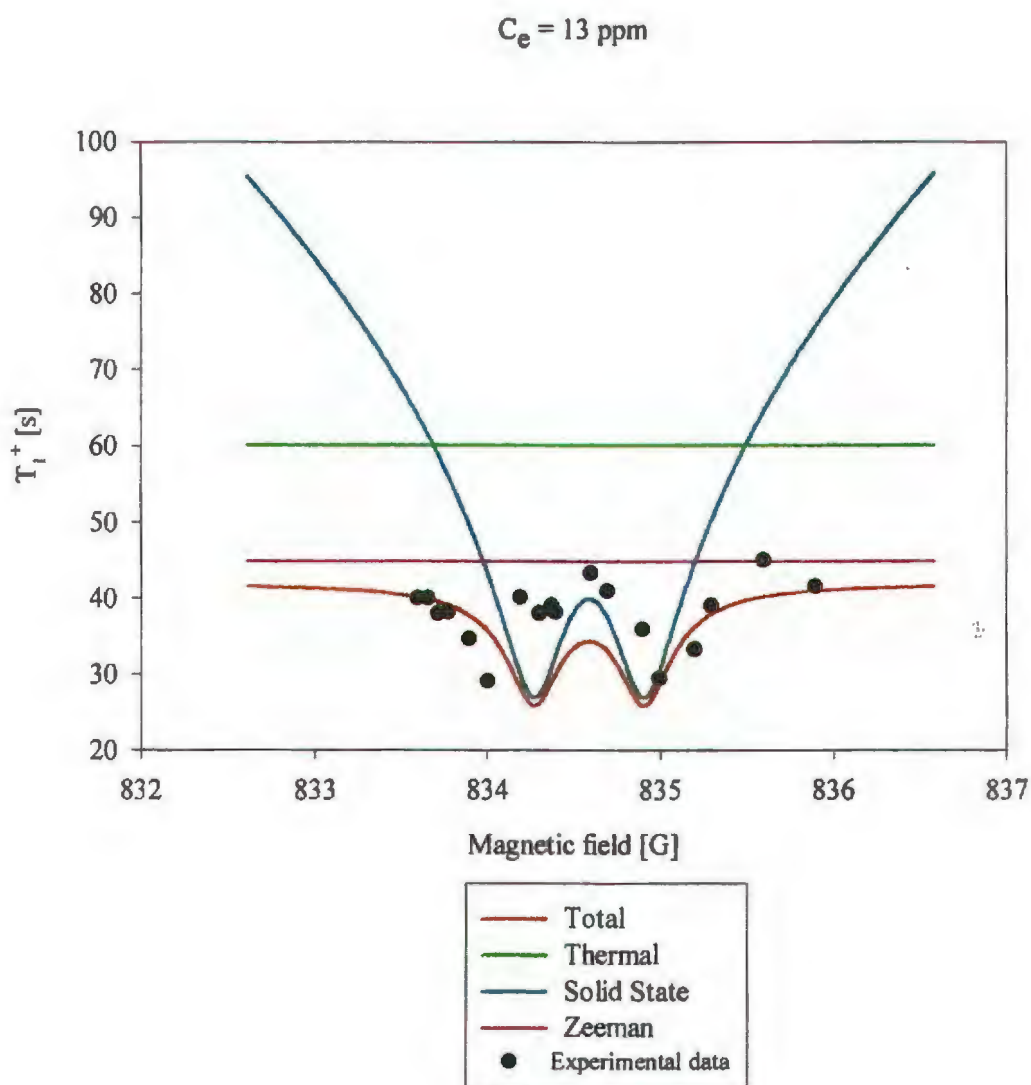


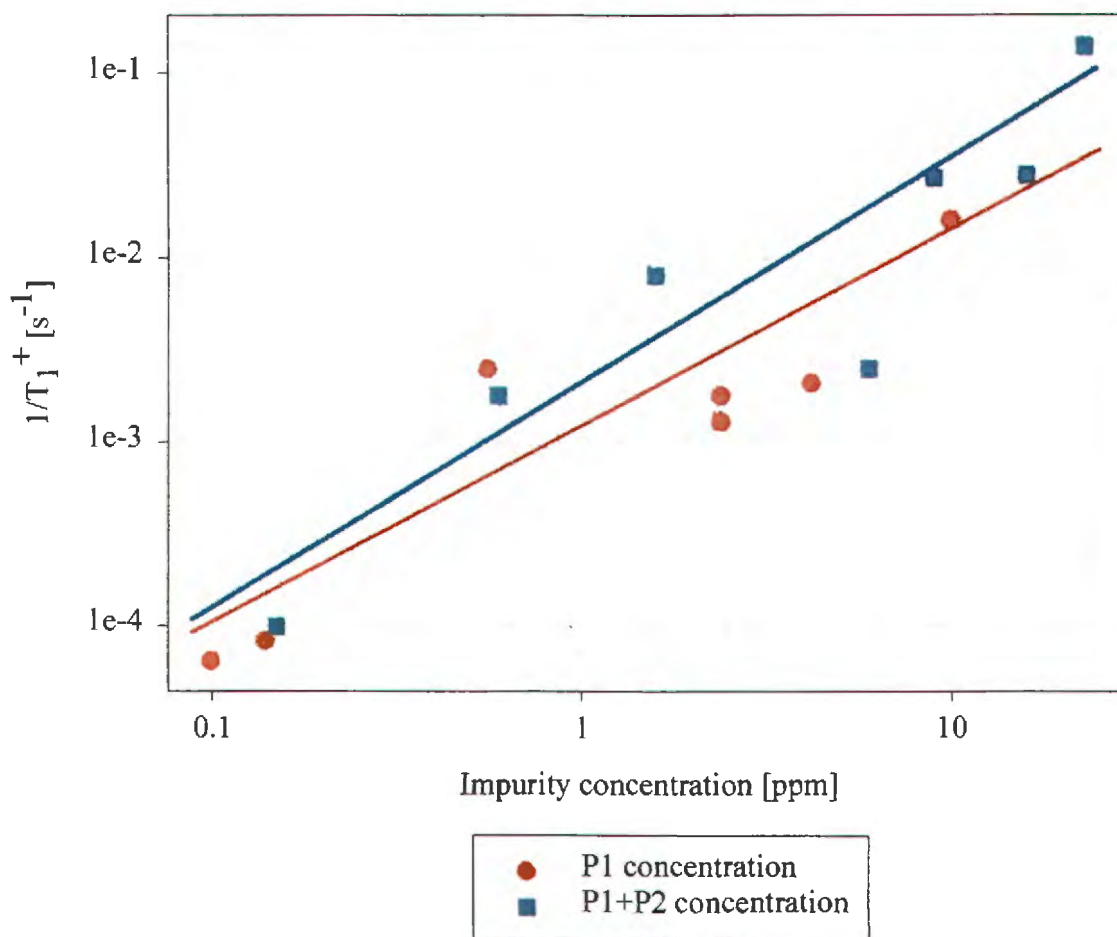
Table 7.1. Diamond Data sample B2

Parameter	Value	Remark	
C_e (P1)(ppm)	9.3	From T_{2e}	
C_e (Total)(ppm)	23	From T_{2e}	
T_{2n} (s)	0.012	Measured	
T_{2e} (s)	1.4×10^{-6}	Measured	
T_{1e} (s)	7.5×10^{-4}	Measured	
C (cm^6/s)	2.1×10^{-41}	From Eq. 7.12	
b (cm)	5.7×10^{-7}	From Eq. 7.17	
r_{e-n} (cm)	5.8×10^{-8}	From Eq. 7.23	
δ (cm)	9.6 GHz	7.0×10^{-8}	From Eq. 7.16
	2.4GHz	4.6×10^{-8}	From Eq. 7.16
D (cm^2/s)	5.4×10^{-15}	From Eq. 7.18	
$(\tau_{Ce})^{-1}$ (s^{-1})	0.18	From Eq. 7.14	

7.2.5 Dependence of the Polarisation Rate on Impurity Concentration.

Since diamonds have a wide range of impurity concentrations, the polarisation rate could be measured as a function of the impurity concentration for the P1 concentration and the P1 + P2 concentration (as well as other impurities). This was accomplished by performing the polarisation experiments at the fields corresponding to the centre line (P1 + P2) and the hyperfine lines (P1). The isolation of these contributions to the polarisation is explained in the following section. These experiments were carried out at x-band with a field offset of 1.3 G. These results are shown in figure 7.15.

Figure 7.15. ^{13}C DNP relaxation rate as a function of impurity concentration. The solid lines are linear regressions of the measured data.



The calculated rates (blue and red lines) are linear regressions of the measured data of the form:

$$\frac{1}{T_1^+} = kC_e. \quad 7.54$$

Correlation coefficients, R^2 values, for these regressions are 0.84 and 0.85 respectively. If the long relaxation times, experimental difficulties and possible sources of error are taken into account, it can be deduced that the polarisation rate is linearly dependent on the impurity concentration.

7.2.6 Nuclear Signal Enhancement for DNP of Central and Hyperfine lines

The diamond signal enhancement was measured for the central and hyperfine lines as mentioned in section 7.2.5. Some of the results of these experiments are shown in figure 7.16 and 7.17.

Figure 7.16. The growth in ^{13}C magnetisation in a Ib diamond, sample B3 as a function of polarisation time for the central and hyperfine lines.

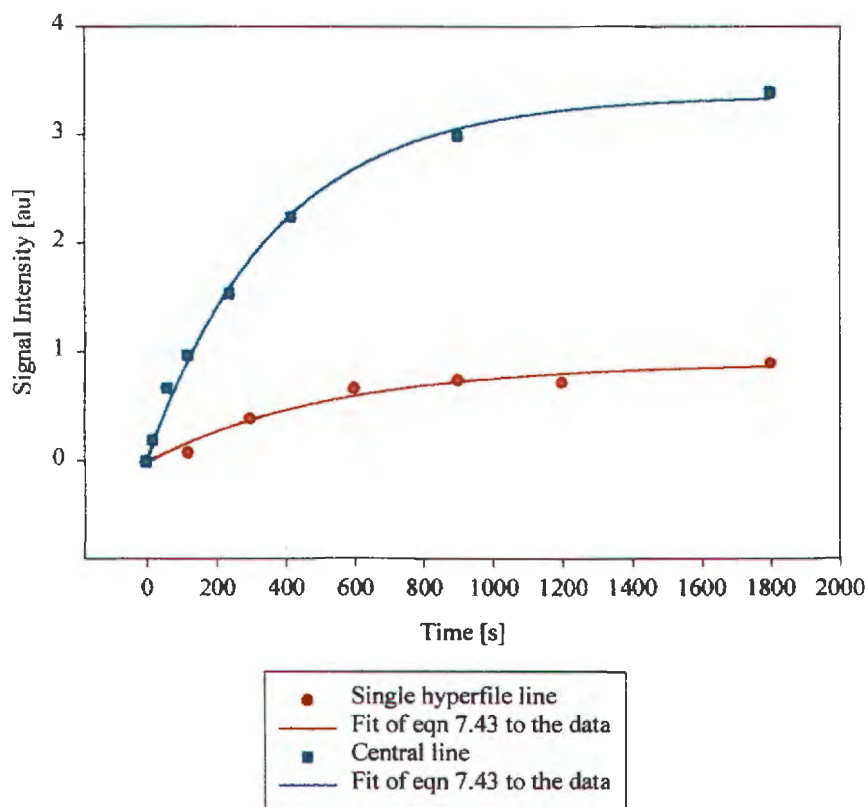
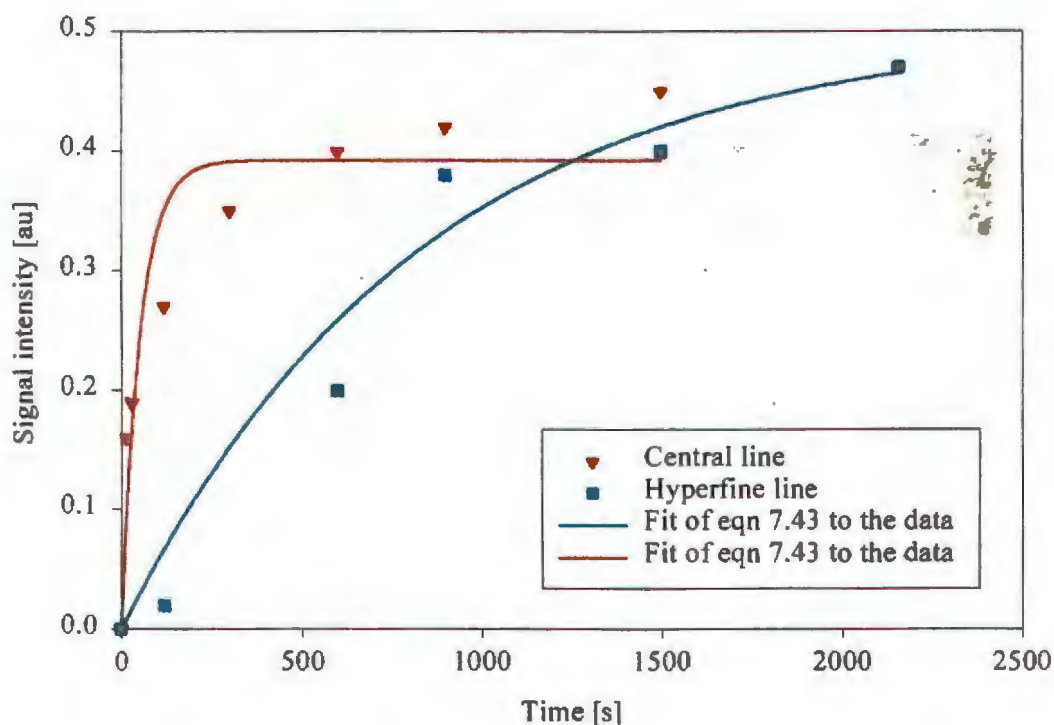


Figure 7.17. The growth in ^{13}C magnetisation in a Ia diamond, sample A13, as a function of polarisation time for the central and hyperfine lines.



According to these results, diamonds can be divided into two groups. For the first group, samples B3 and B6, the signal enhancement for the central transition is four times higher than that for the hyperfine transitions. For a single well-resolved hyperfine line in a type Ib diamond of relatively low impurity concentration, only the ^{13}C nuclei associated with the hyperfine line will be polarised, i.e. one in four nuclei. It then follows that only 25% of the ^{13}C will be polarised by spin diffusion within a reasonable time. For the central line however, all the P1 centres will be involved in the DNP process and will hence result in a signal that is 4 times stronger.

The second group consists of samples A10, A13, B2, B9 and B20. In this case the signal is approximately the same for the central and hyperfine transitions. All these samples are type Ia diamonds, which contain both P1 and P2 centres. The EPR spectra of these samples were shown in figure 3.13 and a broad central line due to overlapping of P1 and P2 lines is clearly visible. Thermal contact is therefore established between the nuclear spin reservoirs (P1 and P2) and the spin-spin interaction reservoir. Since the DNP process establishes contact between the electron Zeeman reservoir and the spin-spin interaction reservoir, the nuclear spin reservoir is brought into contact with the electron Zeeman reservoir via the spin-spin interaction reservoir. Polarising the sample on the central line will therefore activate both P1 and P2 centres. Polarising on the hyperfine line will also polarise both the P1 and P2 centres as they are in thermal contact via the spin-spin interaction reservoir. The result is that the signal enhancement for the hyperfine lines is the same as for the central line. Although sample B2 is a type Ib diamond it does not conform to the behaviour of other Ib diamonds because the P1 concentration in this diamond is sufficiently high for the thermal mixing effect to be active. Therefore, in this case all ^{13}C nuclei are polarised irrespective of the EPR line that is irradiated.

7.3 Discussion

The transition probabilities of all the polarisation techniques discussed are proportional to $1/r_{e-n}^6$ and these techniques are therefore active over relatively short distances. Consequently, the nuclei outside the sphere of radius b , which was defined in section 7.1.4, are polarised by spin diffusion at a rate determined by the diffusion constant [7.11]:

$$\frac{\partial M}{\partial t} \approx D \frac{\partial^2 M}{\partial x^2}. \quad 7.55$$

The spin diffusion constant for diamond was determined by Hoch and Reynhardt [7.8] to be $D \approx 7 \times 10^{-14} \text{ cm}^2 \text{ s}^{-1}$. This equation implies that the polarisation rate can be influenced

by the rate of change of the polarisation gradient between nuclei in the directly polarised zone and those in the spin diffusion polarised zone. The zones referred to were defined in equations 7.21 – 7.23 and were shown in figure 7.4. This is accomplished by increasing the microwave power in the continuous wave DNP processes.

The DNP process that is dominant in a particular diamond is dependent on its paramagnetic impurity concentration as follows:

1. At low concentrations the solid effect dominates the ^{13}C signal enhancement, but at concentrations of more than a few ppm thermal mixing is important. This is due to the effects of the electron broadening system discussed in section 7.1.3.
2. The polarisation rate is determined by the solid effect.
3. The polarisation rate is linearly dependent on the impurity concentration.

Performing a DNP experiment on a single hyperfine line of a Ib diamond of relatively low impurity concentration, gives 25% of the maximum signal enhancement as only 25% of the ^{13}C nuclei participate in the process. This is not the case in Ia diamonds due to the thermal contact of both P1 and P2 centres via the spin-spin interaction reservoir. It is also not the case for Ib diamonds with high P1 concentrations because the thermal mixing effect is activated, which also provides thermal contact via the spin-spin interaction reservoir.

7.4 References

- [7.1] E. C. Reynhardt and C. J. Terblanche, *Chem. Phys. Lett.*, **296**, 464, (1997).
- [7.2] A. Abragam, A. Landesman and J. M. Winter, *C. R. Acad. Sci.*, **247**, 1852, (1958).
- [7.3] E. Erb, J. L. Motchane and J. Ueberfeld, *C. R. Acad. Sci.*, **246**, 2121, (1958).
- [7.4] A. Abragam and W. G. Proctor, *C. R. Acad. Sci.*, **246**, 2253, (1958).
- [7.5] A. Abragam and M. Goldman, *Nuclear magnetism: Order and Disorder*, (Clarendon Press, Oxford, 1982).
- [7.6] M. J. Duivestjin, R. A. Wind and J. Smidt, *Physica* **138B**, 147, (1986).
- [7.7] R. A. Wind, M. J. Duijvestjin, C. van der Lugt, A. Manenschijn and J. Vriend, *Prog. In NMR Spec.*, **17**, 55, (1985).
- [7.8] M. J. R. Hoch and E. C. Reynhardt, *Phys. Rev.*, **B37**, 9222, (1988).
- [7.9] E. C. Reynhardt and G. L. High, accepted for publication in *J. Chem. Phys.* (1998).
- [7.10] J A van Wyk, E C Reynhardt, G L High and I Kiflawi, *J. Phys. D: Appl. Phys.*, **30**, 1790, (1997).
- [7.11] G. R. Khutsishvili, *Sov. Phys. Uspekhi*, **8**, (1966).
- [7.12] D. M. Pozar, in *Microwave Engineering*, (Addison-Wesley, Reading Mass., 1990). P143.
- [7.13] J. H. N. Loubser and J. A. van Wyk, *Rep. Prog. Phys.* **41**, 201, (1978).
- [7.14] A. Carrington and A. D. McLachlan, *Introduction to Magnetic Resonance with Applications to Chemistry and Chemical Physics*, (Harper and Row, New York & London and John Weatherhill, Inc., Tokyo, 1967), p9.
- [7.15] A. Abragam. *The Principles of Nuclear Magnetism*, (Oxford at the Clarendon Press, 1961), p106.

Chapter 8

Dynamic Nuclear Polarisation of Diamond: Nuclear Orientation via Electron Spin-Locking



8.1 Theory of Nuclear Orientation Via Electron–Spin Locking.....	181
8.2 Results	184
8.2.1 Field Offset from Resonance	184
8.2.2 Spin-Locking Pulse Amplitude and Phase.....	185
8.2.3 The Effect of Impurity Concentration on the NOVEL Polarisation Rate	188

8.2.4 NOVEL at Different Frequencies.....	189
8.2.5 Signal Intensity and Polarisation Rates for Pulsed and Continuous Wave DNP Techniques.....	191
8.3 Discussion.....	194
8.4 References.....	195

8.1 Theory of Nuclear Orientation Via Electron–Spin Locking

The nuclear orientation via electron spin-locking (NOVEL) technique of polarisation is in essence the same as the method of Hartmann and Hahn [8.1] for inducing cross-polarisation between nuclear species. This method was first applied for cross-polarisation between nuclei and electrons by Henstra and Wenckebach [8.2] in Si:B systems and then in DCBP systems by Brunner *et al.* [8.3]. To date no thorough treatment of the theory of this technique, which includes spin diffusion and nuclear relaxation effects, has been published. In this thesis, the solid effect theory of Khutsishvili [8.4] is applied to NOVEL.

The NOVEL transition probability is estimated, using the approach of Hartmann and Hahn [8.1], as follows:

$$W_{NOVEL} = \frac{\Gamma_{novel}}{r_{e-n}^6} = \sqrt{\frac{\pi}{8}} \left(\frac{T_{e-e}}{T_{e-n}^2} \right), \quad 8.1$$

where T_{e-e} is the spin-spin relaxation time due to electrons and T_{e-n} is the contribution of electrons to the spin-spin relaxation time due to nuclei, which is given by [8.1]:

$$\frac{1}{T_{e-n}^2} = \frac{9}{4} \frac{(\sin \theta \cos \theta)^2 \gamma_e^2 \gamma_n^2 \hbar^2}{r_{e-n}^6}. \quad 8.2$$

The parameters r and θ are the polar co-ordinates of the vector between the electron and the external field.

Averaging over θ gives:

$$\frac{1}{T_{e-n}^2} = \frac{9}{30} \frac{\gamma_e^2 \gamma_n^2 \hbar^2}{r_{e-n}^6} \quad 8.3$$

and the NOVEL transition probability becomes:

$$W_{NOVEL} = \frac{\Gamma_{NOVEL}}{r_{e-n}^6} = \frac{3}{10} \sqrt{\frac{\pi}{8}} \frac{1}{r_{e-n}^6} \gamma_e^2 \gamma_n^2 \hbar^2 T_{2e}, \quad 8.4$$

where $\frac{1}{T_{2e}} \approx \sqrt{M_2}$ has been used as an estimate for the electron second moment.

It must also be noted that the polarisation transfer is only active during the locking pulse and a recovery time of approximately $5T_1$ is required before the NOVEL sequence can be applied again. The fraction of the total time, α , that ^{13}C polarisation takes place is therefore given by:

$$\alpha = \frac{\tau_{sl}}{\tau_{\pi/2} + \tau_{\text{recovery}} + \tau_{sl}}. \quad 8.5$$

where $\tau_{\pi/2}$ is the length of the initial $\pi/2$ pulse, τ_{sl} is the length of the spin-locking pulse and τ_{recovery} is the recovery time.

The NOVEL polarisation rate is then given by:

$$T_1^+ = \frac{8\pi}{3} N_e D^{\frac{3}{4}} (\alpha \Gamma_{NOVEL})^{\frac{1}{4}}. \quad 8.6$$

During the application of the NOVEL pulse sequence the relevant continuous wave processes and Zeeman polarisation are also activated and contribute to the nuclear signal enhancement. The overall polarisation rate is therefore given by [8.5]:

$$T_1^+ = \frac{8\pi}{3} N_e D^{\frac{3}{4}} [\alpha(\Gamma_{NOVEL} + \Gamma^+ + \Gamma^- + K) + C]^{\frac{1}{4}}. \quad 8.7$$

At this point it is interesting to make a comparison between the ^{13}C polarisation rates of NOVEL and the solid effect. Using equation 7.10 with $\pi g(\omega - \omega_e \pm \omega_n) \approx T_{2e} \gamma_e$, the solid state effect's transition probability becomes:

$$W^\pm = \frac{3\pi}{20} \left(\frac{H_1}{H_0} \right)^2 \frac{1}{r_{e-n}^6} \gamma_e^4 \hbar^2 g(\omega - \omega_e \pm \omega_n) = \frac{3\pi}{20} \left(\frac{H_1}{H_0} \right)^2 \frac{1}{r_{e-n}^6} \gamma_e^4 \hbar^2 T_{2e}. \quad 8.8$$

The ratio of transition probabilities is given by:

$$\frac{W_{NOVEL}}{W^\pm} = \frac{\frac{3}{10} \sqrt{\frac{\pi}{8}} \frac{1}{r_{e-n}^6} \gamma_e^2 \gamma_n^2 \hbar^2 T_{2e}}{\frac{3\pi}{20} \frac{1}{r_{e-n}^6} \gamma_e^4 \hbar^2 T_{2e} \left(\frac{H_1^2}{H_0^2} \right)}, \quad 8.9$$

which simplifies to:

$$\frac{W_{NOVEL}}{W^\pm} = \frac{1}{\sqrt{2\pi}} \frac{\gamma_n^2}{\gamma_e^2} \frac{H_0^2}{H_1^2}. \quad 8.10$$

In a typical x-band experiment, $H_0 = 3500 \text{ G}$ and $H_1 = 0.1 \text{ G}$ for the solid state effect and $H_1 = 1.3 \text{ G}$ for NOVEL. Substituting these values into equation 8.10 yields:

$$\frac{W_{NOVEL}}{W^\pm} = \frac{1}{\sqrt{2\pi}} \frac{(6.2 \times 10^3)^2 (3500)^2}{(1.6 \times 10^7)^2 (0.1)^2} \approx 10^2.$$

NOVEL is therefore more effective under these conditions, but as the microwave power is increased, the solid state effect will become the more effective mechanism. The NOVEL and solid effects will be approximately equally effective when $W_{NOVEL}/W^{\pm} = 1$ or when the condition, $H_1 = 1.8$ G at x-band, is satisfied.

When comparing the solid effect and NOVEL the factor α should be included. The NOVEL transition probability becomes:

$$W_{NOVEL}^{eff} = \alpha W_{NOVEL}. \quad 8.11$$

Inserting typical values into equation 8.5 gives $\alpha \approx 10^{-3}$, which in turn gives:

$$\frac{W_{NOVEL}^{eff}}{W^{\pm}} = 0.1,$$

i.e. at x-band, under the conditions described above, the transition probability for NOVEL is slightly lower than for the solid state effect.

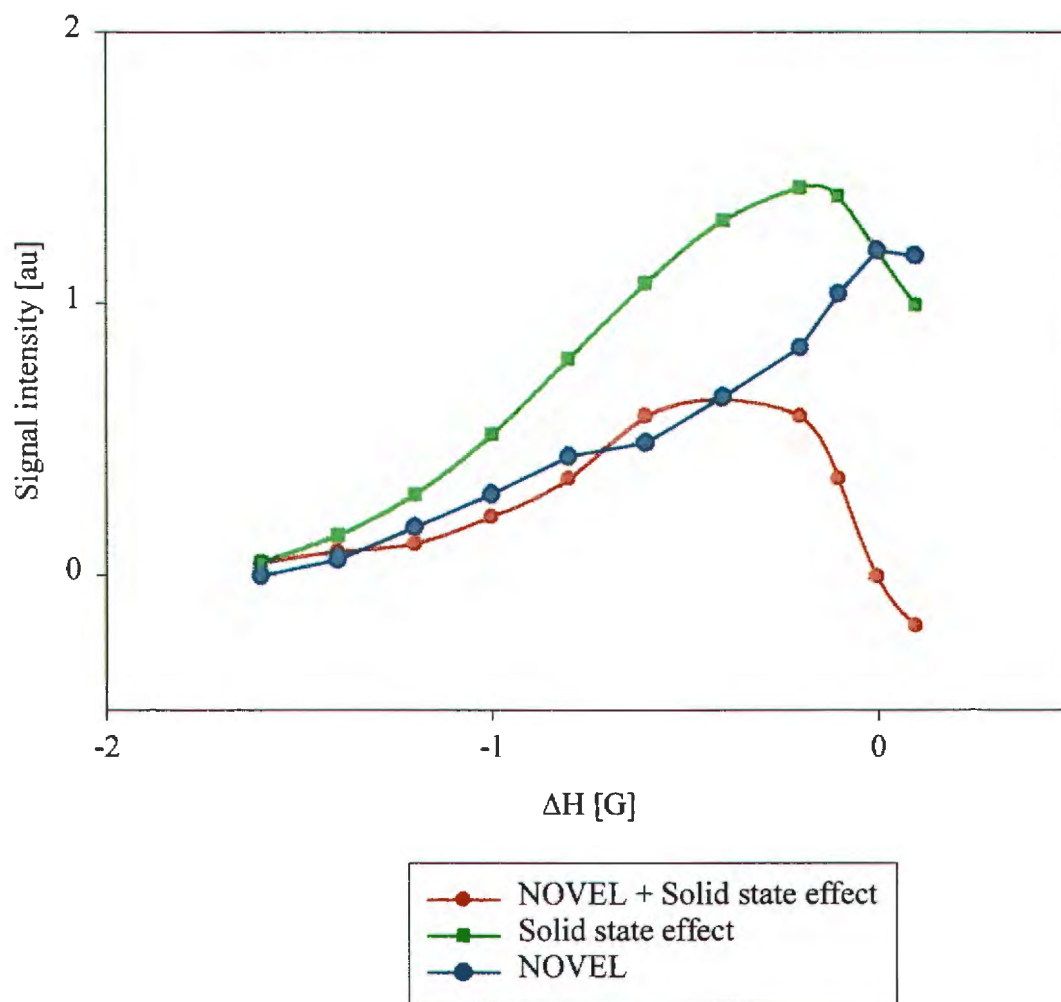
8.2 Results

8.2.1 Field Offset from Resonance

The sensitivity of the NOVEL technique to the field at which the NOVEL pulse sequence is applied, was investigated in these experiments by shifting the static field from the exact resonance field, H_0 , in steps of 0.2 G. The results show that the maximum NOVEL effect is obtained at the EPR resonance, $\Delta = 0$, as predicted by the theory. As the field is shifted from exact resonance, the continuous wave DNP processes start contributing to the polarisation. To determine the NOVEL contribution independently, the solid effect was measured by removing the first $\pi/2$ pulse from the NOVEL sequence. These signal intensities were then subtracted from the corresponding data for the sequence with the

$\pi/2$ pulse included. The resulting data points represent the NOVEL contribution. The results are shown in figure 8.1.

Figure 8.1. Experimentally obtained dependence of the NOVEL process on the offset from exact resonance.

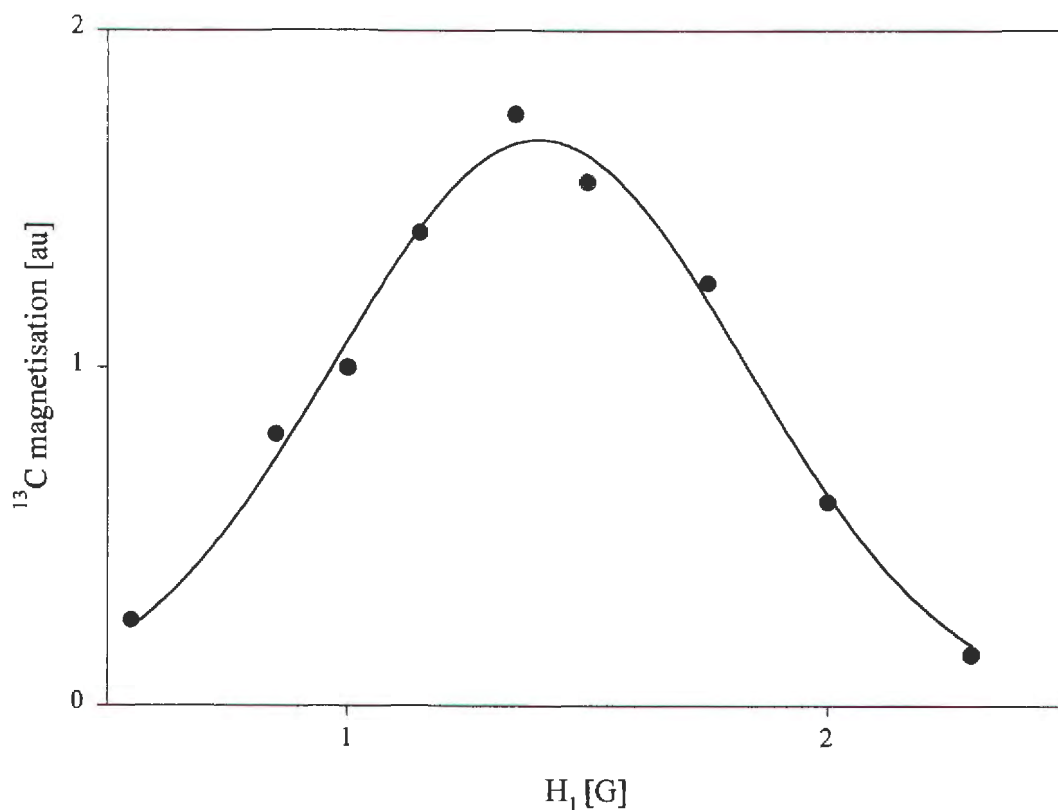


8.2.2 Spin-Locking Pulse Amplitude and Phase

The static field was set to the exact resonance for the central EPR resonance line and the microwave power varied to determine the sensitivity of NOVEL to satisfying the

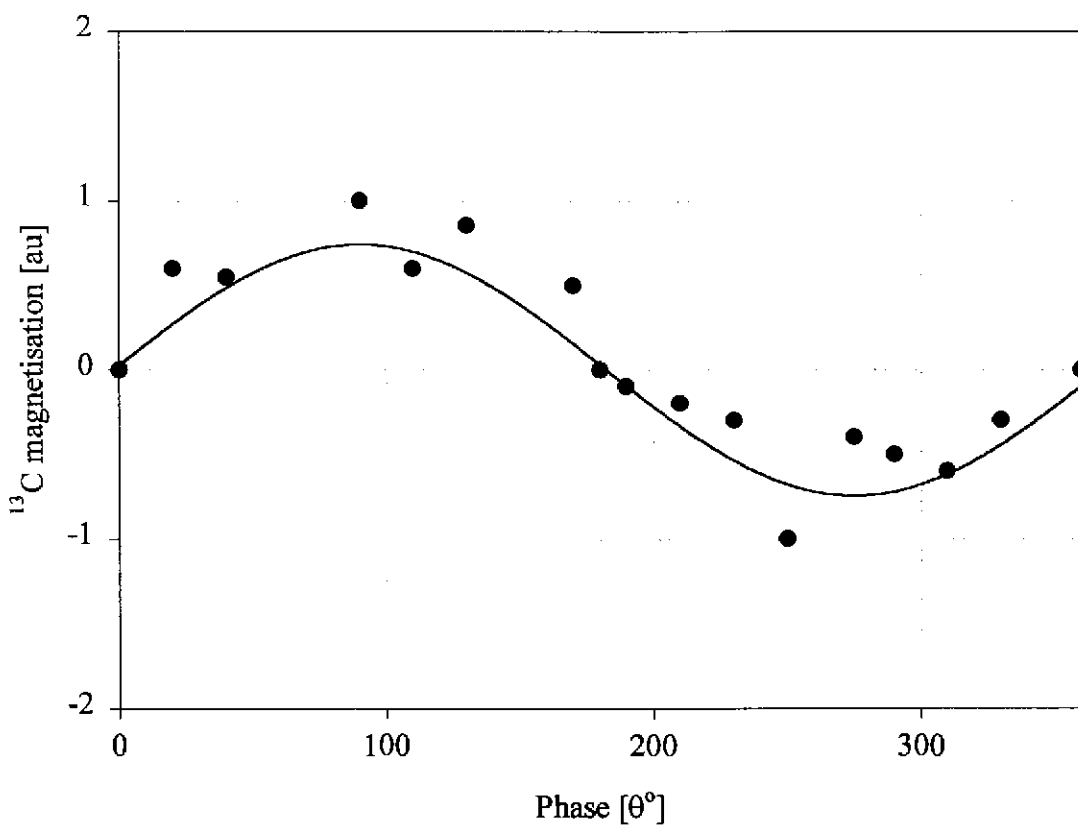
Hartman-Hahn condition. Figure 8.2 indicates that the technique is effective over a relatively large range about the theoretical maximum at resonance. This range is approximately 0.5 G and is most probably determined by the width of the EPR line and the sample size. If H_1 is not uniform over the volume of the sample, the Hartman-Hahn condition is not satisfied for all impurities in the sample at a particular external field. As the H_1 field is varied, some impurities are included in the NOVEL process while others are excluded.

Figure 8.2. Experimentally obtained dependence of the ^{13}C magnetisation on the NOVEL spin-locking pulse amplitude.



The second experiment involved varying the phase of the spin-locking pulse with respect to the initial $\pi/2_x$ pulse from 0° to 360° . The results, shown in figure 8.3, indicate that the effect is optimal at 90° and 270° as predicted by the theory.

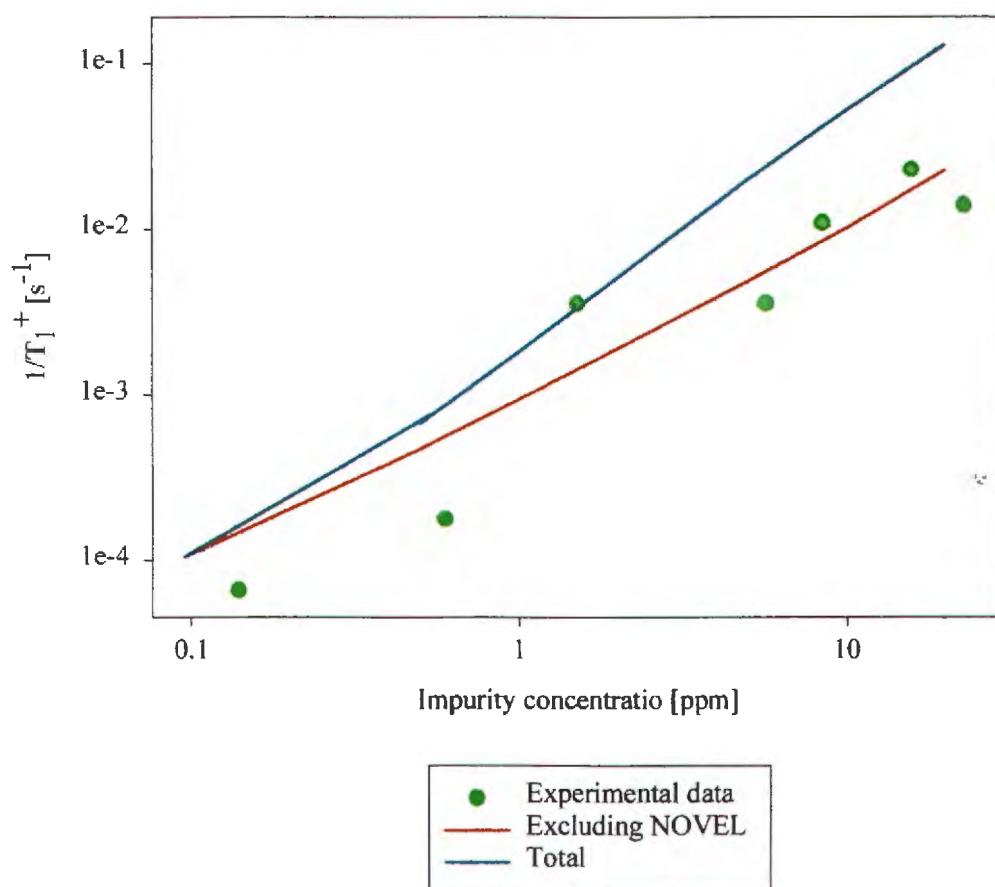
Figure 8.3. Experimentally obtained dependence of the NOVEL process on spin-locking pulse phase θ .



8.2.3 The Effect of Impurity Concentration on the NOVEL Polarisation Rate

The effect of impurity concentration on the NOVEL polarisation rate is shown in figure 8.4. It must be born in mind that when applying the NOVEL pulse sequence, the relevant continuous wave DNP processes are also active. Cognisance of this fact must be taken when comparing the experimental and theoretical values. The theoretical curves in figure 8.4 were generated using equations 8.6 and 8.7. It can be seen that there is quite good agreement between theory and experiment. Discrepancies are probably due to the line width and size effect, discussed earlier, which would lower the polarisation rates.

Figure 8.4. ^{13}C NOVEL relaxation rate $1/T_1^+$ as a function of impurity concentration.



8.2.4 NOVEL at Different Frequencies

The ^{13}C signal strength for diamond B2 as a function of the NOVEL polarisation time at 9.6 GHz and 2.4 GHz are shown in figures 8.5 and 8.6, respectively. The solid lines were obtained by fitting the following equation to the data:

$$M = M_0 \left[1 - \exp\left(-\frac{\tau}{T_{1\text{NOVEL}}^+}\right) \right]. \quad 8.12$$

In equation 8.12 the variable τ is the duration of the application of the NOVEL sequence. From these fits, the values of M_0 , the equilibrium magnetisation and T_1^+ are obtained. The respective T_1^+ values are:

$$(T_1^+)_x = 17 \text{ s},$$

and

$$(T_1^+)_s = 66 \text{ s},$$

Values for α were calculated using equation 8.5 with $\tau_{\pi/2} \approx 0$, $\tau_{sl} = 400 \mu\text{s}$ and $\tau_{\text{recovery}} = 1.5 \text{ ms}$ at x-band and with $\tau_{\pi/2} \approx 0$, $\tau_{sl} = 1.4 \mu\text{s}$ and $\tau_{\text{recovery}} = 1.5 \text{ ms}$ at s-band.

The resulting values are:

$$\alpha_x = 9.5 \times 10^{-4},$$

and

$$\alpha_s = 0.2.$$

According to equation 8.6:

$$\frac{(T_1^+)_x}{(T_1^+)_s} = \left(\frac{\alpha_s}{\alpha_x} \right)^{\frac{1}{4}}. \quad 8.13$$

The experimentally obtained ratio determined from the relaxation times is 0.257 and the theoretical ratio obtained from the α values is 0.262. The polarisation rates are therefore approximately the same at the two frequencies for the same value of α in accordance with the theory.

Figure 8.5. NOVEL polarisation build up rate at s-band for sample B2.

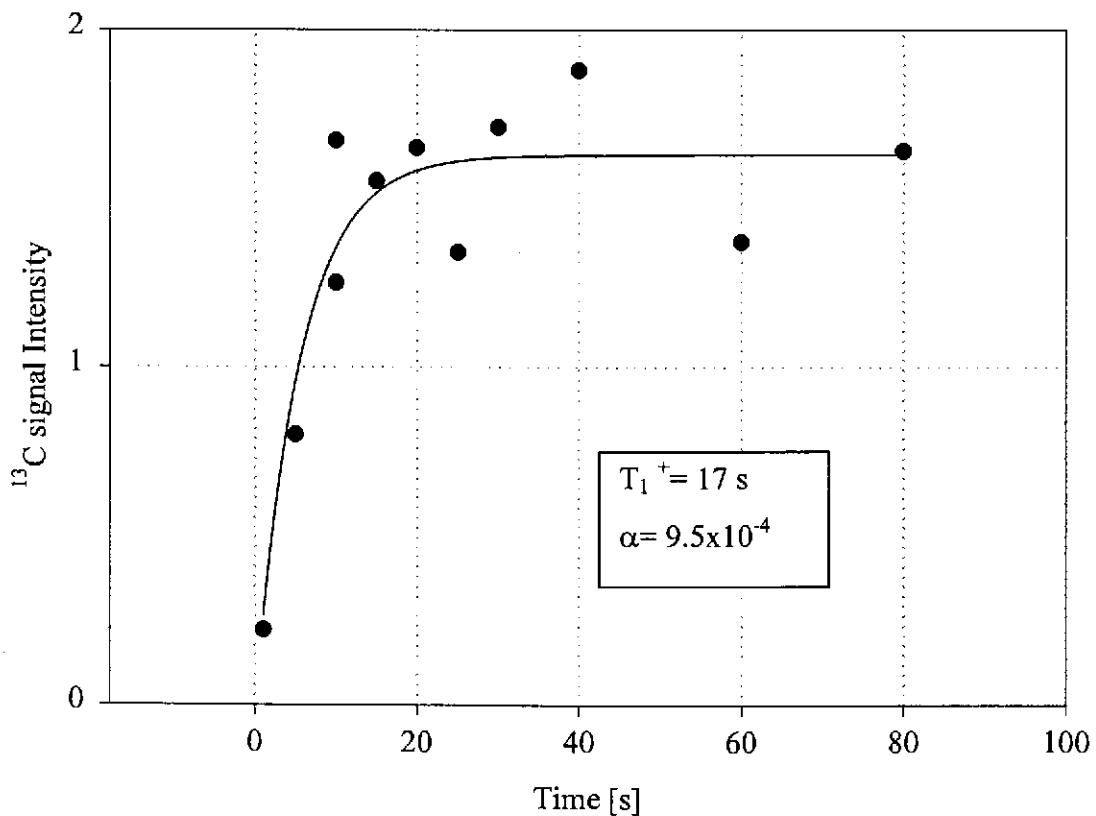
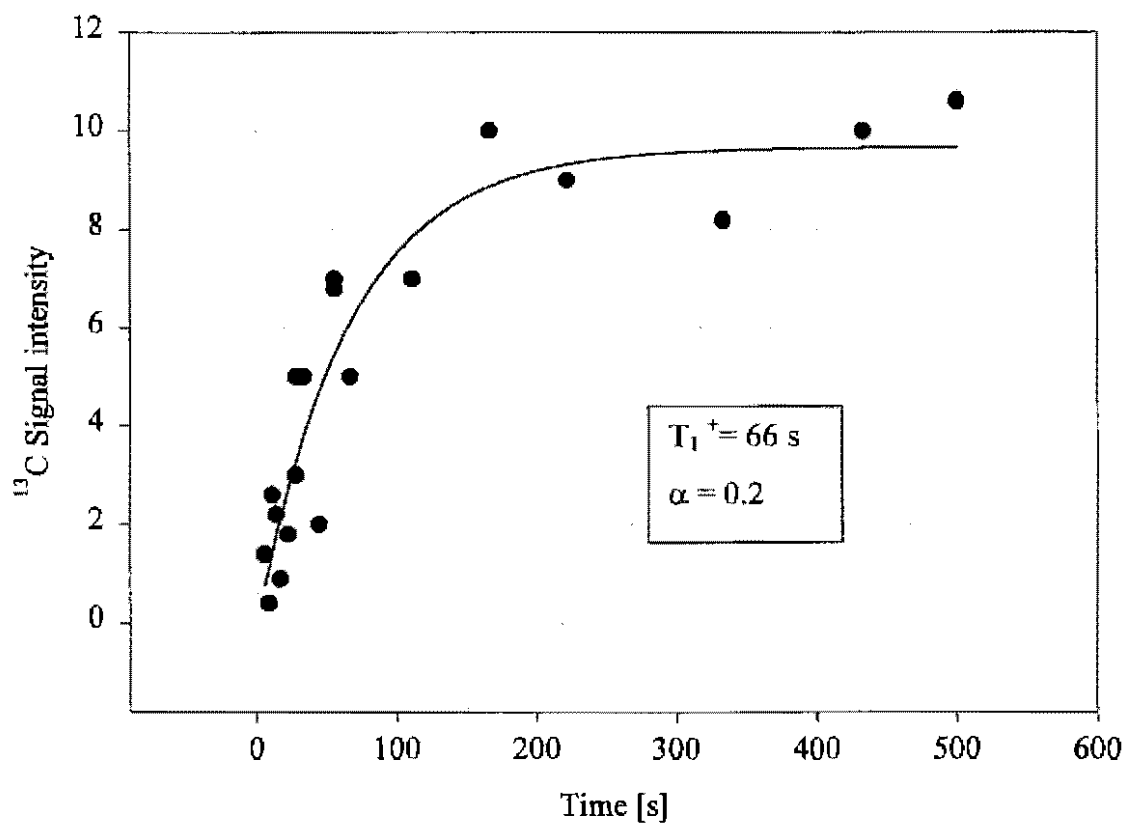


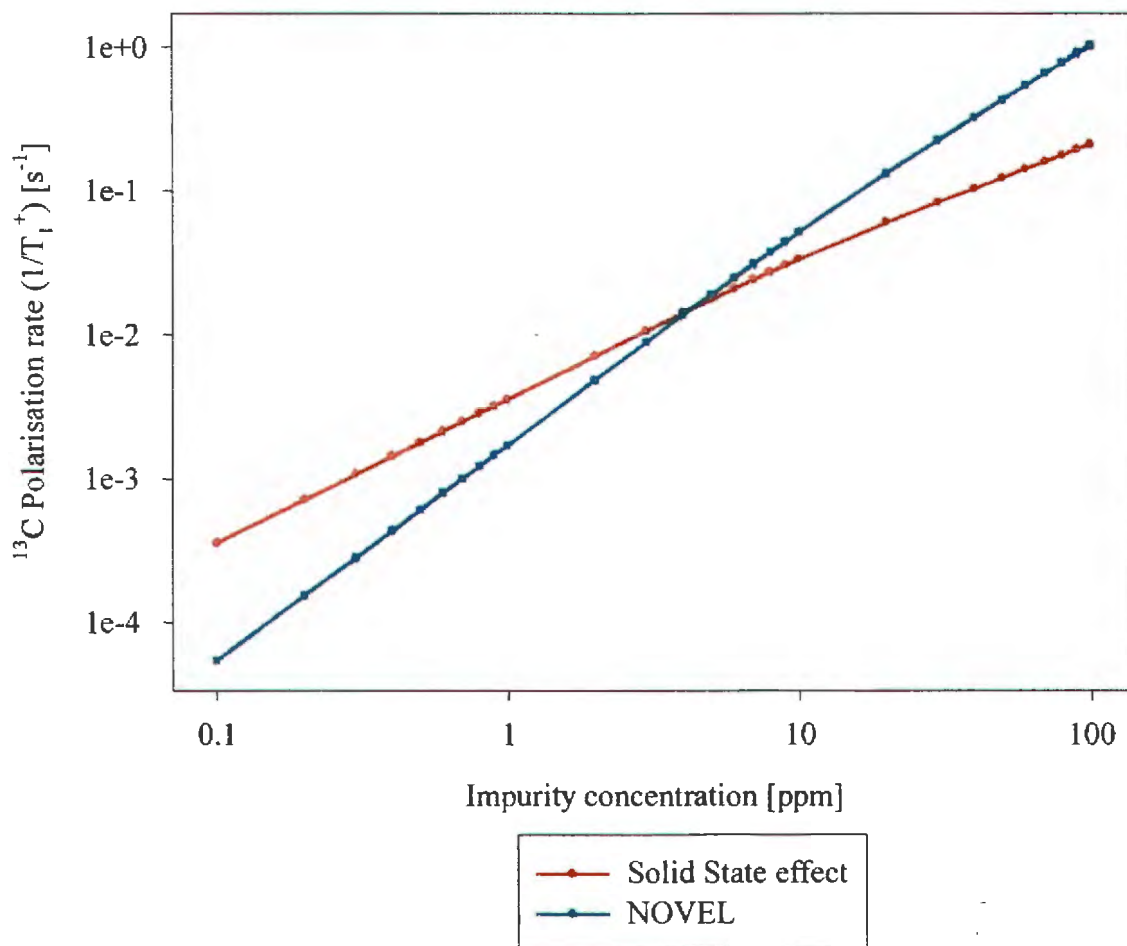
Figure 8.6 NOVEL polarisation build up rate at x-band for sample B2.



8.2.5 Signal Intensity and Polarisation Rates for Pulsed and Continuous Wave DNP Techniques

In this discussion, the signal intensity was calculated for the solid effect and the NOVEL effect for the same H_1 of about 0.1 G. This result is given in figure 8.10 and shows very little difference between the polarisation rates for the two techniques. This was predicted in the theory when the parameter α was included.

Figure 8.7. A comparison of the NOVEL and solid effects ^{13}C signal intensity for $H_1 = 1 \text{ G}$ in both cases.



The theoretical prediction for all of the polarisation rates at two C_e values, (23 ppm and 0.1 ppm) is shown in figures 8.8 and 8.9. It is interesting to note that at high impurity concentrations the polarisation rates are limited or determined by the solid or NOVEL effects. At lower concentrations the solid effect determines the rate of polarisation.

Figure 8.8. Theoretical relaxation rates as a function of field for $C_e = 23$ ppm.

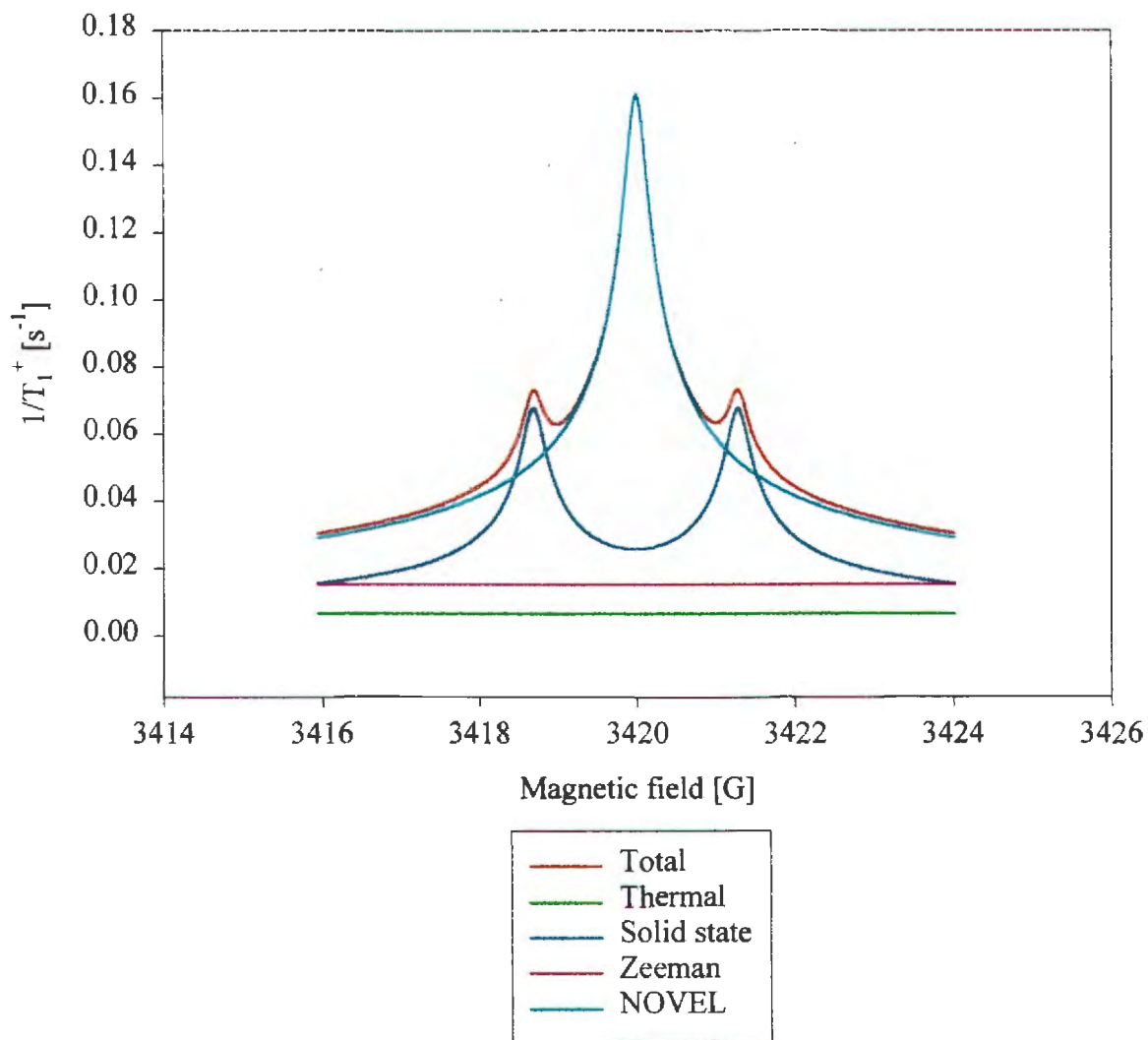
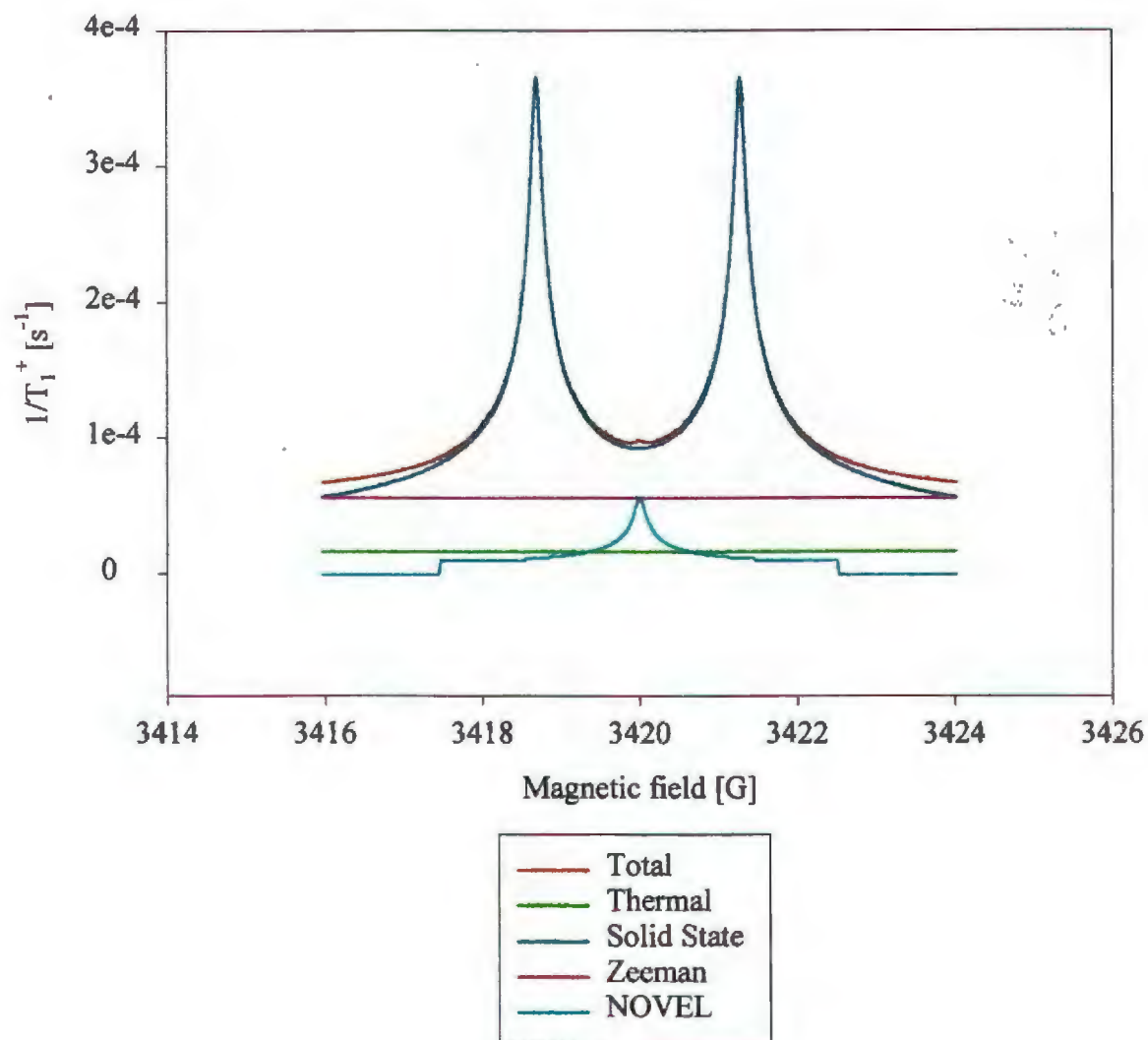


Figure 8.9. Theoretical relaxation rates as a function of field for $C_e = 0.1$



8.3 Discussion

The transition probability for the NOVEL effect is much higher than that for the solid effect for relatively low H_1 fields. The NOVEL polarisation rate is however limited by

α , i.e. the $T_{1\rho}$ and T_{1e} values. The net effect is that in practice, the solid and NOVEL polarisation rates are similar. Also in the case of the NOVEL effect, the microwave power is dictated by the Hartman-Hahn condition and therefore little can be done to increase the polarisation rate.

8.4 References

- [8.1] S. R. Hartmann and E. L. Hahn, *Phys. Rev.*, **128**, (1962).
- [8.2] A. Henstra and W. Th. Wenckebach, in *Pulsed Magnetic Resonance: NMR, EPR and Optics, A recognition of E L Hahn*, (Clarendon Press, Oxford, 1992).
- [8.3] H. Brunner, R. H. Fritsch and K. H. Hausser, *Z. Naturforsch.*, **42a**, 1456, (1987).
- [8.4] G. R. Khutsishvili, *Sov. Phys. Uspekhi*, **8**, (1966).
- [8.5] E. C. Reynhardt and G. L. High, Accepted for publication, *J. Chem. Phys.*, (1998).

Chapter 9

Concluding remarks



9.1 Achievements..... 198

9.2 Recommendations 199

9.1 Achievements

One of the main motivations for this study was to obtain an understanding of the fundamental physics of dynamic polarisation of diamond. The solid state, thermal mixing and NOVEL effects were investigated and a good grasp of the fundamental physics underlying these processes was achieved.

Although some work had been done in the field of continuous wave dynamic nuclear polarisation of diamond, no results have been reported for similar studies employing pulsed techniques. An aspect of the continuous wave processes that required additional attention was the effect of impurity types and concentration on these processes. The methods described in chapter 5 to determine the concentration of P1 and P2 centres were used extensively in the investigation of the DNP techniques. In addition, they are a useful tool for further investigations of diamond. The fact that the DNP processes were applied at the same field as the NMR measurements in previous investigations placed severe limitations on the scope of experiments that could be carried out. In the present study, all DNP and NMR experiments were carried out in independent systems. This allowed the DNP processes to be investigated at two frequencies i.e. 2.4 GHz and 9.6 GHz. The retention of the induced polarisation in the dipolar reservoir was exploited during transfer from the DNP system to the NMR system.

Henstra and Wenckebach, [9.1] reported that transfer of magnetisation from the electron spin system to the nuclear spin system was completed within a few milliseconds in Si:B systems, when the NOVEL effect was exploited. This result can be misleading as it refers to the electron relaxation time in the rotating frame, $T_{1\rho}$, that determines the optimum length of the spin-locking pulse. The NOVEL pulse sequence must be applied repeatedly for a much longer time for complete transfer of polarisation between the two spins systems. This system is very similar to diamond containing paramagnetic impurities and it was expected that diamond would behave in a similar manner. As reported in chapter 8, relaxation times of seconds or minutes were achieved for diamond employing the solid state, thermal mixing and NOVEL effects.

From our investigation it was established that the only parameters that affect the relaxation rates for the DNP processes are:

1. The microwave power for the continuous wave processes.
2. The paramagnetic impurity concentration in the diamond.
3. The field, H_0 , at which the experiment is performed.
4. The optimum NOVEL pulse sequence (i.e. the α value).

It was also established or confirmed that all the DNP processes are limited by spin diffusion, which in turn is dependent on the paramagnetic impurity concentration.

The results of this study are in the process of being published in four articles and three patents, which were listed in the introductory pages of this thesis.

9.2 Recommendations

As a result of the information obtained with regard to the impurity types and their concentrations, a deeper understanding of DNP processes in diamond could be obtained. This investigation has been limited to studying the most common defects, i.e. P1 and P2 centres, but it is believed that other more exotic defects, containing oxygen, iron and cobalt, may lead to some interesting effects and should be the subject of further investigation.

It was mentioned above that DNP processes are limited by the paramagnetic impurity concentration. A possible avenue for further research in this field is the investigation of the possibility of creating temporary paramagnetic defect centres using ionising radiation. The lifetime of these centres should be such that they can participate in the DNP processes.